UNIVERSITÀ DI PISA
Dottorato in Ingegneria

NUCLEAR ENGINEERING AND INDUSTRIAL SAFETY

Development and characterization of an innovative ASIC pixel detector for imaging based on chromatic photon counting technology

Supervisors
Prof. Ing. Francesco D'Errico
Dott. Ing Riccardo Ciolini
Dott. Ronaldo Bellazzini

Student
Pasquale Luca de Ruvo

Academical Year 2015

Cycle XXVIII

Abstract

The purpose of this work is to characterize Pixirad (INFN spin-off) detector system, an innovative X-ray imaging sensor with intrinsic digital characteristics, based on *Chromatic Photon Counting* technology. The system counts individually the incident X-ray photons and selects them according to their energy to produce two color images per exposure. The energy selection occurs in real time and at radiographic imaging speed (GHz global counting rate). Photon counting, color mode and a very fine spatial resolution allow to obtain a high ratio between image quality and absorbed dose. The individual building block of the imaging system is a two-side buttable semiconductor radiation detector made of a thin pixellated CdTe crystal coupled to a Very Large Scale Integration (VLSI) CMOS pixel ASIC (Application Specific Integrated Circuits).

The first chapter is devoted to introduce the basic processes of interaction of photons with matter. In the second chapter the most common radiographic metrics are described with an introduction to the imager systems. The third chapter focuses on the pixel detectors, describing the physical mechanism of charge collection involved in the CdTe sensor and explaining the principal components of the front-end electronic chain.

In the fourth chapter the general features of Pixirad detector system are described. The chapter five is focused on the characterization of the Pixirad-1 detector system from the spectroscopic point of view: an energy calibration and resolution has been carried out using different X-ray sources and the charge sharing fraction has been evaluated by exploiting the monochromatic Elettra synchrotron beam. The aim of chapter six is the characterization of the imaging performance of the detector with monochromatic synchrotron radiation at different energies, investigating the linearity of the system, the ratio between detector counts and number of impinging photons, as a function of energy and discriminator thresholds, the pixel noise and the spatial resolution. In the chapter seven are showed some last measurements with *PIXIE III*: the third and last generation of Pixirad ASIC. In particular the full recovering of the charge sharing effect is demonstrated at 62 micron pixel pitch allowing the sharp spectral separation between the color images.

Contents

List of Figures

List of Tables

Chapter 1

Interaction of X-rays with Matter

There are four major interaction processes when a photon interacts with matter. Each one of these is determined by a cross-section which depends on the photon energy and on the density and atomic number of the medium [1].

- *Rayleigh (coherent) scatter*: the photon interacts with the total electron cloud of an atom.
- *Compton (incoherent) scatter*: the photon interacts with an individual electron whose binding energy is low compared to that of the incident photon.
- *Photoelectric absorption*: the photon interacts with an inner atomic electron.
- *Pair production*: the photon converts into an electron-positron pair when it enters the strong Coulomb field surrounding an atomic nucleus.

The attenuation of a beam of photons includes scatter as well as absorption processes. Thus

$$Attenuation = Scatter + Absorption. \tag{1.1}$$

All the interaction processes (apart from coherent scatter) result in the production of electrons as consequence of ionization, so the major fraction of the photon energy is imparted to the medium. In this sense photons are known as *indirectly ionizing radiation*. Secondary photons that are generated from the primary processes - from Rayleigh or Compton scattering of the primary beam or as a characteristic X-ray of fluorescence event - can interact again according to one of the previous four processes if they are energetically possible.

1.1 Photon beam attenuation

It is possible to express the attenuation of a photon beam which has an initial intensity I_0 across a medium of thickness x with the following equation:

$$I = I_0 e^{-\mu x} \tag{1.2}$$

where μ is known as *attenuation coefficient* $[cm^{-1}]$. In a beam with a good (or narrow) geometry the detection of scattered photons is minimized (position A), while in a bad (or wide) geometry the effects of scatter are prominent, as in position B (fig. 1.1). These two distinctions depend of:

- the distance from the detector to the material,
- the size of the detector compared with the width of the beam,
- the photons energy,
- the density and mean atomic number of the material.

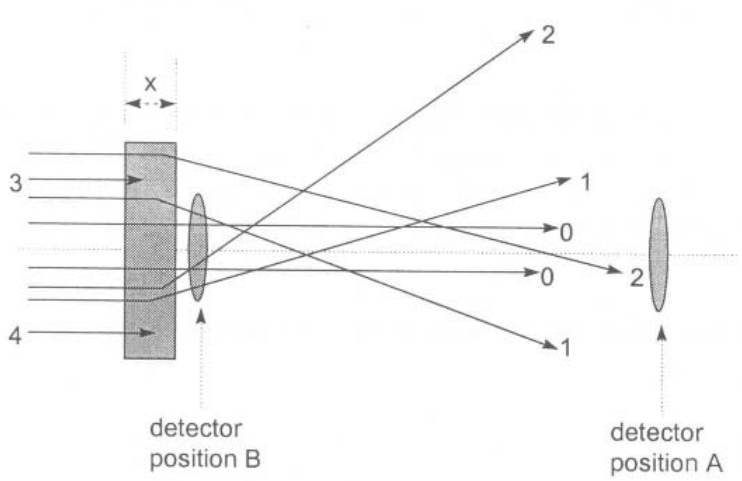

Figure 1.1: Interaction processes of photon beam in a material: only photons with tag "0" reach the detector in position A (and one with tag "2" - Compton), while the detector in position B records all the photons [1].

Usually the dependence on density is conveniently removed to have an expression for the mass attenuation coefficients of the individual processes:

$$\frac{\mu}{\rho} = \frac{\sigma_{coh}}{\rho} + \frac{\sigma_{incoh}}{\rho} + \frac{\tau}{\rho} + \frac{\kappa}{\rho} \tag{1.3}$$

in this way the *mass attenuation coefficient* μ/ρ has the unit of cm^2g^{-1}. This gives the total attenuation in terms of the individual cross-sections specified per gram of material.

Using the *Avogadro constant* N_A and the *atomic mass* A it is possible to determine the number of electron and atom per gram:

$$\frac{N_A}{A} = \left[\frac{atom}{gram}\right] \tag{1.4}$$

$$\frac{ZN_A}{A} = \left[\frac{electron}{gram}\right] \tag{1.5}$$

So it is possible to lead

$$\frac{\tau}{\rho}\left(\frac{cm^2}{g}\right) = \frac{\tau}{\rho}\frac{A}{N_A}\left(\frac{cm^2}{atom}\right) \tag{1.6}$$

$$\frac{\sigma_{incoh}}{\rho}\left(\frac{cm^2}{g}\right) = \frac{\sigma_{incoh}}{\rho}\frac{A}{ZN_A}\left(\frac{cm^2}{e^-}\right) \tag{1.7}$$

The number of electrons per gram is constant to within ~ 10 for all materials (apart from hydrogen which has no neutron in its nucleus). So the probability of a Compton event depends largely on the density of the material and weakly on its atomic number [1].

1.2 Thomson scatter from a single electron

The *differential scatter cross-section* is defined as the probability that the energy contained within the incident electromagnetic wave is scattered into a solid angle $d\Omega$ at an angle of Ω with respect to the incident direction [1] and in a classical approximation it is equal to:

$$\frac{d\sigma_0}{d\Omega} = \frac{r_0^2}{2}\left(1+\cos^2\theta\right) \tag{1.8}$$

where $r_0 = 2.8179 \cdot 10^{-15}m$ is the classical electron radius. Integrating over all the angles it gives the total Thomson cross section σ_0. Considering the fig. 1.2:

$$\frac{d\sigma_0}{d\theta} = \frac{d\sigma_0}{d\Omega}\frac{d\Omega}{d\theta} = \frac{r_0^2}{2}\left(1+\cos^2\theta\right)2\pi\sin\theta \tag{1.9}$$

1.3 Coherent scatter

The coherent or Rayleigh scatter is the interaction between a photon with an atomic electrons whose binding energy is considerably greater than the incoming photon energy [1]. There in no transfer of energy to the medium (scattered wavelength = incident

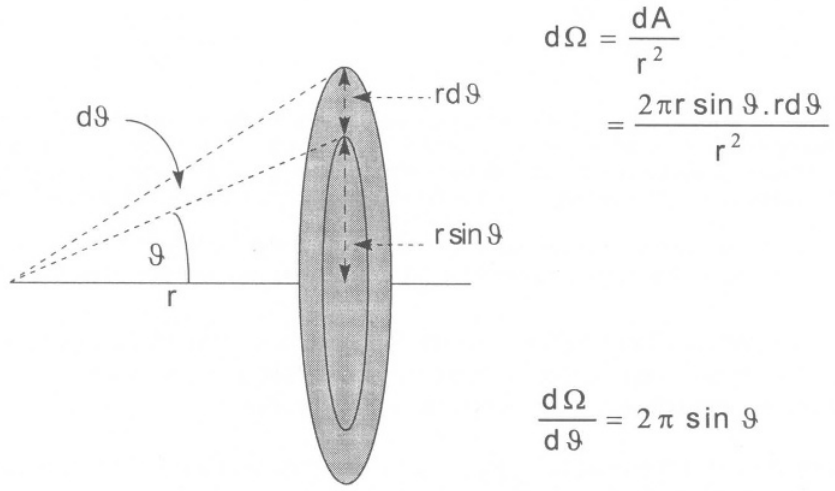

Figure 1.2: Geometric relations in the scattering process of a photon by an electron [1].

wavelength) so the Z electrons in the atom hold the recoil momentum without absorbing any energy. Rayleigh scatter becomes more important as the photon energy decreases and the atomic number of the medium increases. The Thomson cross-section is multiplied by a form factor, $F(x,Z)$, where Z is the atomic number of the atom, $x = \sin(\vartheta/2)/\lambda$, and λ is the wavelength of the photon. $F(x,Z)$ represents the spatial electron distribution in the atom from which the photon can be scattered without any momentum transfer. The mathematical expression of the differential cross section is

$$\frac{d\sigma_0}{d\theta} = \frac{r_0^2}{2}\left(1+\cos^2\theta\right)2\pi\sin\theta\,[F(x,Z)]^2 \tag{1.10}$$

$F(x,Z)$ tends to zero at large angles, while it tends to Z with small angles.

1.4 Incoherent scatter

The classical theory approach to describe the incoherent scatter is not sufficient, but it has to be replaced by relativistic considerations because the order of magnitude of photon energy range approaches the rest mass of an electron

$$m_0c^2 = 511keV \tag{1.11}$$

The main characteristics of this process known also as *Compton scatter* are:

- the momentum conservation between the outgoing photon and the struck electron;

- incoherent scattering takes place with higher probability from individual free electrons (unbound). At lower photon energy the photoelectric absorption takes place. Corrections exist for Compton scatter from bound electrons using the incoherent scatter function $S(x,Z)$;
- it is important to distinguish between the probability of an interaction taking place (*Klein-Nishina formula*) and the amount of energy transferred in that process (momentum conservation equations).

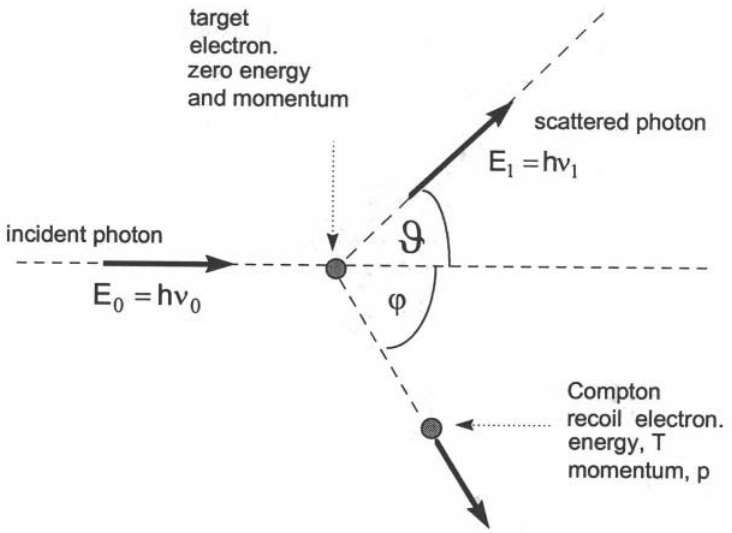

Figure 1.3: Geometric relations in the Compton scatter process [1].

It is well known that the energy of photon is equal to

$$E_0 = h\nu_0 \tag{1.12}$$

in case of bounded electron, its energy is $<< h\nu_0$. In fig. 1.3 it is shown that energy and momentum are conserved between the electron and photon. Considering the following energy and momentum balance equation

$$h\nu_0 = h\nu_1 + T \tag{1.13}$$

$$\frac{h\nu_0}{c} = \frac{h\nu_1}{c}\cos\theta + p\cos\varphi \tag{1.14}$$

$$0 = \frac{h\nu_1}{c}\sin\theta - p\sin\varphi \tag{1.15}$$

$$pc = \sqrt{T\,(T + 2m_0c^2)}. \tag{1.16}$$

Writing that $\alpha = h\nu_0 / m_0c^2$, with some manipulation it is possible obtain the following equations:

1. *Compton wavelength shift*

$$\Delta\lambda = \lambda_1 - \lambda_0 = \frac{c}{\nu_1} - \frac{c}{\nu_0} = \frac{h}{m_0 c}(1 + \cos\vartheta) \tag{1.17}$$

   the wavelength shift depends only on scattering angle and not on the incident photon energy.

2. *Energy of scattered photon*

$$h\nu_1 = \frac{m_0c^2}{1 - \cos\vartheta + \left(\frac{1}{\alpha}\right)} = \frac{h\nu_0}{1 + \alpha(1 - \cos\vartheta)} \tag{1.18}$$

3. *Energy of the recoil electron*

$$T = h\nu_0 \frac{\alpha(1 - \cos\vartheta)}{1 + \alpha(1 - \cos\vartheta)} \tag{1.19}$$

4. the minimum scattered photon energy and the maximum electron recoil energy is reached with $\vartheta = \pi$

5. when $\vartheta \to 0$, $T \to 0$ and the photon retains its original energy $h\nu_0$.

1.5 Photoelectric Absorption

In photoelectric absorption process all the energy of photon is given to a bound electron, the energy in excess is imparted to the electron as kinetic energy as shown in the following equations:

$$E_K = h\nu_0 - BE_K \tag{1.20}$$

$$E_L = h\nu_0 - BE_L \tag{1.21}$$

where K and L are the atomic shell of the electron. An absorption edge occurs whenever the photon energy reaches an electron binding energy, the discontinuities being greatest for the most tightly bound (K-shell) electrons. To calculate theoretically photoelectric cross-section is used the *Born approximation* in which the calculations are performed with a plane wave for the electron wave function, without considering the attraction of nuclear charge on the electron as it leaves the atom. This approximation loses validity when energy photon are comparable to the ionization potential of

the atom. So it is possible to determine the analytical expression of the atomic cross-section for K-shell electrons in an atom of atomic number Z as:

$$a^{\tau}\kappa = \frac{8}{3}\pi r_0^2 Z^5 \alpha^4 2^{\frac{5}{2}} \left(\frac{m_0 c^2}{h\nu_0}\right)^{\frac{7}{2}} \tag{1.22}$$

where $r_0 = e^2/m_0c^2$, $\alpha = 2\pi e^2/hc = 1/137$ is the fine structure constant.

The vacancy in a K- (or L-, M-..) shell following photoelectric absorption results in a de-excitation of the atomic system, either by *characteristic X-ray* or *Auger-electron emission* (fig. 1.4). The relative probability of these de-excitation processes is given by the fluorescence yield. Characteristic X-ray emission (known as *fluorescence*) yield

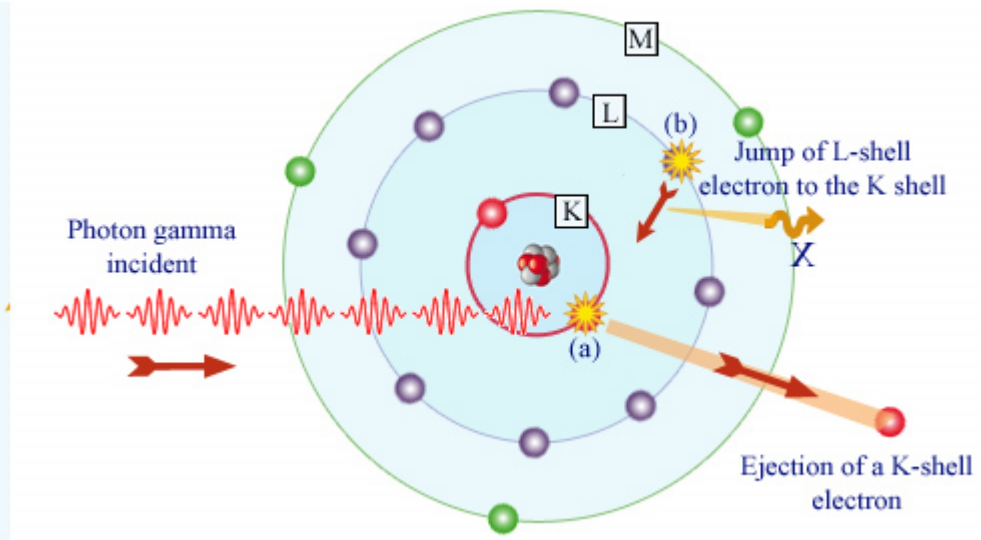

Figure 1.4: Processes involved the photoelectric effect.

is strongly dependent on Z, being small for light atoms and large for heavy atoms. Auger emission is classified by the atomic energy levels involved, so a vacancy initially created in the K-shell can be filled by an electron from one of the outer shells L (say L_1). The energy released in this de-excitation process is transferred to another electron in a shell having a smaller binding energy (say L_3) [1].

1.6 Pair production

This process happens in the field of a charged particle (mostly in the strong Coulomb field of the nucleus), although it can also take place at high energies in the field of an

electron. Pair production has a threshold photon energy equal to the combined rest mass of two electrons as showed in the following balance of energy:

$$h\nu = \left(T^{+} + m_0c^2\right) + \left(T^{-} + m_0c^2\right) \tag{1.23}$$

This means that the pair production is possible only if the photon energy exceeds twice the electron rest-mass energy:

$$h\nu > 0.501MeV \cdot 2 = 1.02MeV \tag{1.24}$$

The energy in excess goes in kinetic energy shared by the positron and the electron. The positron annihilates after the slowing-down in the medium so two photons are produced [2]. In fig. 1.5 it is plotted the relative importance of the three interaction processes described in this chapter.

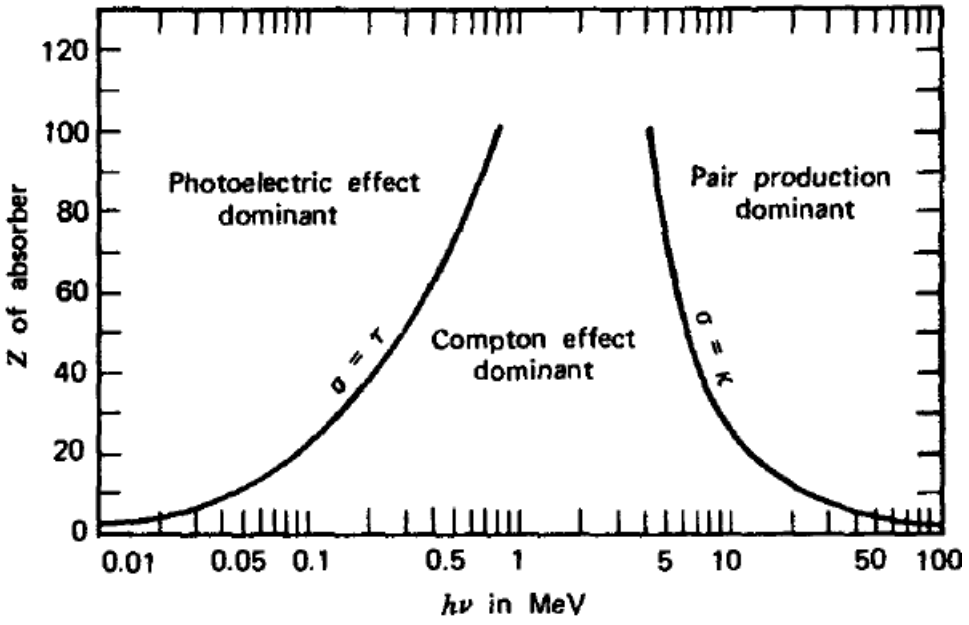

Figure 1.5: The relative importance of the three interaction processes [2].

Chapter 2

Introduction to digital imaging

The principle features that characterize an imager are:

- its contrast resolution,
- its spatial resolution,
- its sensitivity,
- the radiation dose or other potentially harmful consequences to the object,
- the nature of the interactions which underlie the imaging process.

Conventional X-ray imaging are widely diffused in medical and industrial application from the beginning to the middle of the 20th century. For example the development of computerized tomography with X-rays in the 1960's evolved during the last decades in the sophisticated technology of the present-day. New imaging technique has been developed to help radiologist in the diagnosis:

- X-ray computerized tomography (CT),
- positron emission tomography (PET),
- magnetic resonance imaging (MRI),
- single photon emission computerized tomography (SPECT).

Each of these modalities is based on different physical interactions between the radiation and the tissue being imaged. The information contained within each type of image is therefore unique to that method [1].

The first part of this chapter is devoted to the definition of the main radiographic metrics, while in the second part it is treated the description of the principal imager devices.

2.1 Contrast

Contrast is the difference in the image gray scale between closely adjacent regions on the image. The contrast present in a medical image is the result of a number of different steps that occur during image acquisition, processing, and display. Different definitions of contrast occur for each step in the imaging process.

Subject contrast [3] is the difference in some aspect of the signal, prior to its being recorded. Subject contrast is a result of fundamental mechanisms, usually an interaction between the type of energy (*carrier wave*) used in the modality and the topology of the subject. An example gives the possibility to define mathematically the subject contrast. A homogeneous beam of (N_0) X-ray photons is incident upon a slab of tissue with linear attenuation coefficient μ and thickness x (region A), and toward the right there is a small bump of tissue of additional thickness z (region B). Although the increased bump of tissue is shown on top of the tissue slab here. The X-ray fluence (photons$/cm^2$) exiting the slab of tissue (to simplify the discussion no scatter processes are considered) is given by A and B regions respectively. The subject contrast C_s can be defined here as:

$$C_s = \frac{A-B}{A} \tag{2.1}$$

and because $A > B$, C, will be a number between 0.0 and 1.0. The simple equations that define X-ray attenuation are

$$A = N_0 e^{-\mu x} \tag{2.2}$$

$$A = N_0 e^{-\mu(x+z)} \tag{2.3}$$

The equation of contrast becames

$$C_s = 1 - e^{-\mu z} \tag{2.4}$$

Only the difference of two thickness remains in the expression of contrast being caused by difference in the object size z. The expression for subject contrast contains linear attenuation coefficient of the tissue slab, μ. Just like if we increase z, subject contrast will increase. Figure 2.1 shows the linear attenuation coefficient for tissue, plotted as a function of x-ray energy. At lower energies, μ increases substantially. This also illustrates that changing imaging modality parameters (kV of X-ray tube) can often be used to increase subject contrast. In other words this means that the contrast information is carried mainly by low energy photons.

Detector contrast, C_d, is determined principally by how the detector converted energy into the output signal. Different detectors can convert input energy to output signal with different efficiency, and in the process amplify contrast. *Characteristic curve* is an important parameter of a imaging detector that shows the relation between the input energy and the output signal in a detector. The detector contrast is defined from a

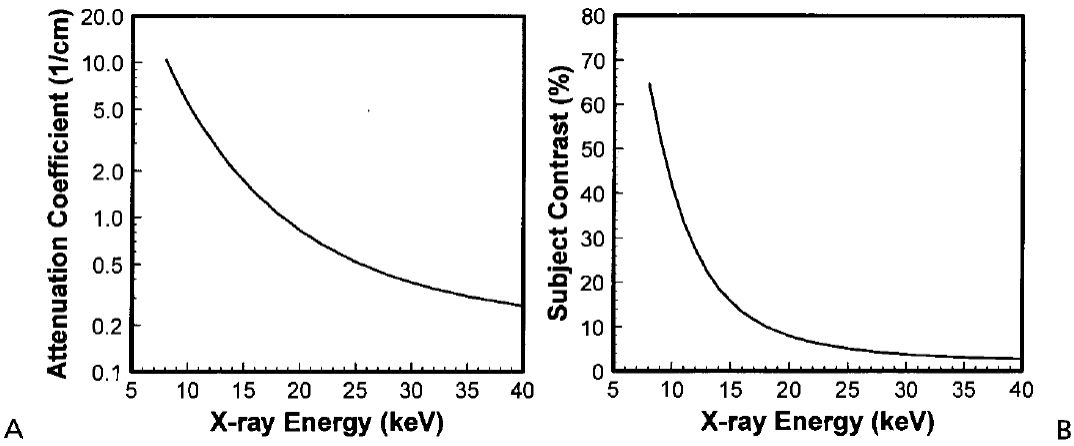

Figure 2.1: The linear attenuation coefficient and subject contrast as function of the photon energy [3].

mathematical point of view as the slope of characteristic curve. This curve is typically non-linear in a screen film, while is quasi-linear (or properly) in a digital imager. Another very important advantage of a *digital imaging system* is that the unit that conveys the light and dark properties for each pixel is called a gray scale value, or sometimes a digital number. This means that it is possible to apply numerical conditioning of the image improving the radiographic performance.

A more meaningful and frequently used measure in assessing digital images, related to contrast, is the *contrast-to-noise ratio* (CNR):

$$CNR = \frac{|A-B|}{\sigma} \tag{2.5}$$

where A and B are the counts in two different region of the detector and σ is the noise. It is a measure of the detectors ability to distinguish between objects in an image and the image noise. In case of applicability of Poisson model (photon counting type detectors)

$$\sigma = \sqrt{\frac{A+B}{2}}. \tag{2.6}$$

2.2 Spatial resolution

A two-dimensional image really has three dimensions: height, width, and gray scale. *Spatial resolution* is a property that describes the ability of an imaging system to accurately depict objects in the two spatial dimensions of the image. The classic notion of spatial resolution is the ability of an image system to distinctly depict two

objects as they become smaller and closer together. When two objects become so close that they appear as one the spatial resolution is lost [3].

2.2.1 The point spread function

The simpler way to measuring the spatial resolution of a detector system in the spatial domain is to stimulate the detector system with a single point input, and then observe how it responds. The image produced from a single point input to a detector is called a a *point spread function* (PSF) (fig. 2.2). If the PSF is measured at many different locations and it is invariant from position, the imaging system is said to be *stationary*, conversely the detector system is considered *nonstationary*. Practically a point stimulus could be reached using a very narrow (pencil) beam of photons with a small hole (10 μm diameter) aligned (in two dimension) with a focal spot of 1 mm, this is considered a very difficult measurement. Synchrotron sources have a low beam divergence and usually are used for this scope.

An image is just a large collection of individual points, and exposing the imaging system to an image, the PSF acts to blur each and everyone of the millions of point inputs that comprise the image. The process of breaking up an input image into its constituent point stimuli, individually blurring each point using the PSF of the imaging system, and then adding up the net result is a mathematical operation called convolution [3] (not met in this thesis).

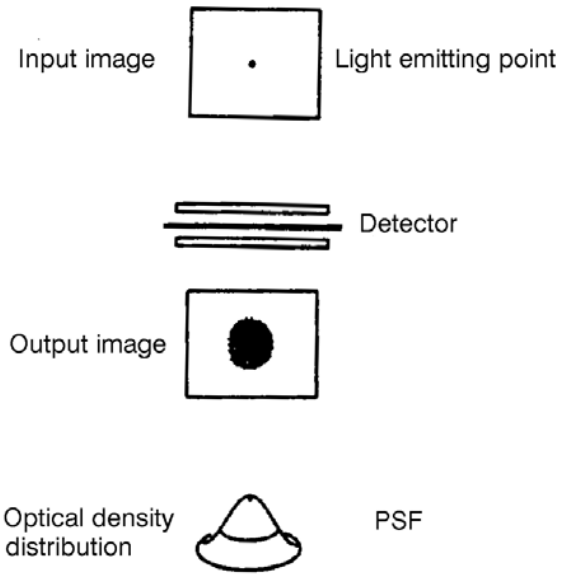

Figure 2.2: Point Spread Function.

2.2.2 Other spread functions

Because the PSF implies many experimental difficult, other spread functions become useful. The *line spread function* (LSF) describes the response of an imaging system to a linear stimulus (fig. 2.3). A slit image is acquired and a 90-degree profile across the slit is measured to determine the LSF. The LSF can be thought of as a linear collection of a large number of PSFs. The LSF is slightly easier to measure experimentally, because the linear slit that is used need only be aligned with the focal spot in one dimension. A single LSF describe the imaging system's behavior for a imaging system with an isotropic PSF (PSF with regular radial blurring). If the PSF is nonisotropic, the LSF needs to be measured with the line stimulus positioned at different angles with respect to the imaging system. The LSF is often determined in both the horizontal and vertical axes of the imaging system.

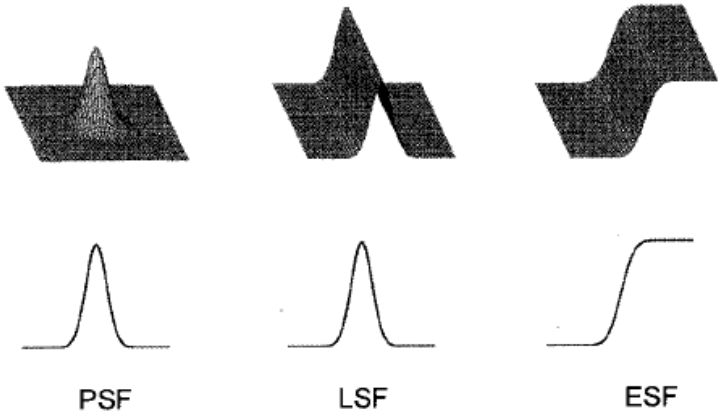

Figure 2.3: Three different spread functions : PSF, LSF, ESF [3].

The *edge spread function* (ESF) is sometimes measured instead of the LSF (fig. 2.3). Rather than a hole (for the PSF) or a line (for the LSF), only a sharp edge is needed to measure the ESF. The ESF is measured in situations where various influences to the imaging system are dependent on the area exposed. Where the spatial properties of scattered x-ray radiation are often measured using this technique. Very little scatter is produced with a small linear stimulus (the LSF), but with the ESF measurement half the field is exposed, which is sufficient to produce a measurable quantity of scattered radiation [3].

2.3 The frequency domain

Another useful way to explore the resolution of an imaging system is to make use of the spatial *frequency domain*. Similarly to the phenomena in which waves are involved

like sound, for objects on an image that are separated by shorter distances (measured in millimeters), these objects correspond to high spatial frequencies ($cycles/mm$). In

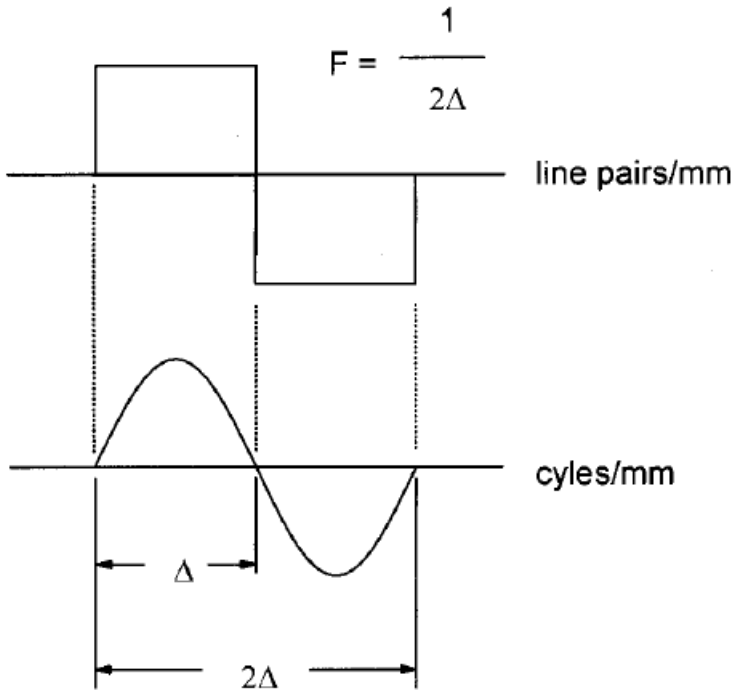

Figure 2.4: Spatial frequency [3].

fig. 2.4 it is illustrates a (spatial domain) sine wave spanning a total distance of 2Δ, where Δ is measured in millimeters. If $\Delta = 0.5mm$, then the single cycle of the sine wave would be 1.0 mm across, and this would correspond to 1 $cycles/mm$. The relationship between the distance spanned by one-half cycle of a sine wave, Δ, and the spatial frequency F, is given by:

$$F = \frac{1}{2\Delta} \tag{2.7}$$

The square wave (fig. 2.4) is a simplification of the sine wave, and the square wave shown corresponds to a single line pair. The units of spatial frequency are sometimes expressed as $line-pairs/mm$ (lp/mm), instead of $cycles/mm$. For example, objects that are 50 lp/mm across (0.050 mm) correspond to 10 $line-pairs/mm$, and objects that are 0.250 mm correspond to 2 $line-pairs/mm$.

Low spatial frequencies correspond to larger objects in the image, and higher spatial frequencies correspond to smaller objects. Knowing the size of an object (Δ), it is possible to convert it to spatial frequency (the equation above), and knowing the spatial frequency F, it is possible to convert object size [3].

2.3.1 The Modulation Transfer Function

The modulation transfer function is a mathematical description of the capability of a system to produce in the image the whole range of spatial frequencies in the object. It is defined as the *ratio between the amplitude frequency spectrum which produces the given image over the amplitude frequency spectrum to produce an image identical to the input* (fig. 2.5). The MTF of a real imaging system is the Fourier transform of the imager output when the input is an infinitely sharp point, edge or line. The MTF can

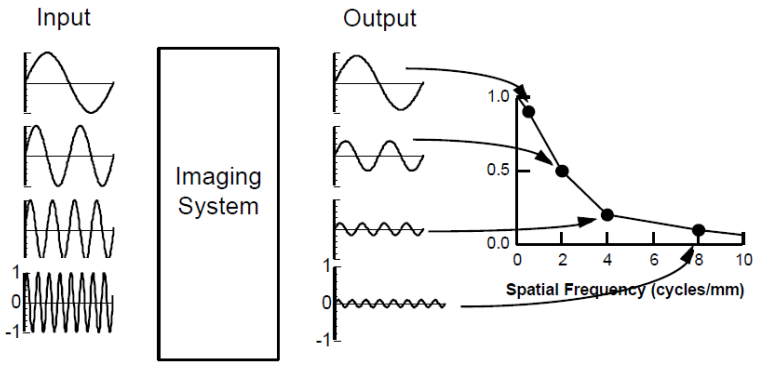

Figure 2.5: Input and output signal of imaging system.

be computed directly from it using the Fourier transform (FT):

$$MTF(f) = | FT[LSF(x)] | \tag{2.8}$$

The Fujita method

From experimental point of view there are many technique to calculate the MTF of a imager device. One of the simpler is the Edge (or Fujita) Method [4]. The first step is to position a slit tilled of a small angle (usually < 2 deg) respect of the perpendicular direction of scanning in deriving the LSF like in fig. 2.6a. Considering the fig. 2.6a, the slit passes across 1 pixel in the horizontal direction sampling four different pixels in vertical direction. Each LSF consists of five discrete data with the same sampling distance Δx for each row of pixel (fig. 2.6b) and it is possible to compone $4 \cdot 5 = 20$ data to generate a *finely sampled LSF* (fig. 2.6c). Calculating the Fourier tranform of LSF, the result is the MTF.

2.4 X-ray imaging technology

For almost a century, X-ray radiographies were made with photographic films, based on gel with AgBr or AgI grains. During the past two decades, digital radiog-

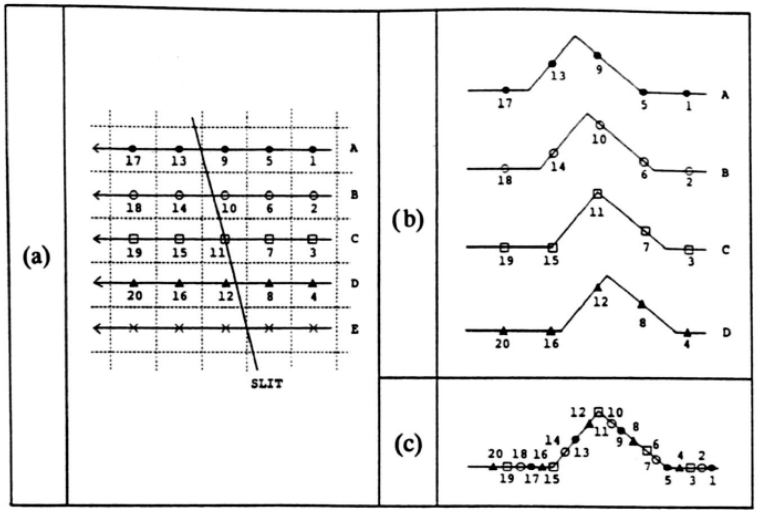

Figure 2.6: The Fujita Method to calculate the MTF [4].

raphy has supplanted screen-film radiography in many radiology departments. In 1980 X-ray images were first recorded digitally with cassette-based storage-phosphor image plates. Ten years after the first direct radiography system appeared, it was charge-coupled device (CCD) slot-scan system. The main advantage of digital detectors is the to archive and store the data in a very simple way. Thus, distribution of images in hospitals can be achieved electronically by means of web-based technology without a low risk to lose images. Another very important advantage regards the medical impact, infact increasing the dose efficiency, and with the greater dynamic range of digital detectors it is possible to reduce the X-ray exposure (dose) to the patient [5]. In fig. 2.7 is reported the main phases of a digital radiography system usually implemented at the hospitals.

2.4.1 Digital imager

Digital radiography can be divided into *computer radiography* (CR) and *direct radiography* (DR). CR systems make use of image plates with a detective layer of crystals that contain different halogenides such as bromide, chlorine, or iodine. The sensing device are usually cast into plates of resin material, and it replaces the conventional films in the cassette.

DR are very interesting device and are the object of this section. DR is able to convert x-rays into electrical charges using a direct readout process. DR systems can be subdivided into direct and indirect conversion groups depending on the type of x-ray conversion used (fig. 2.8).

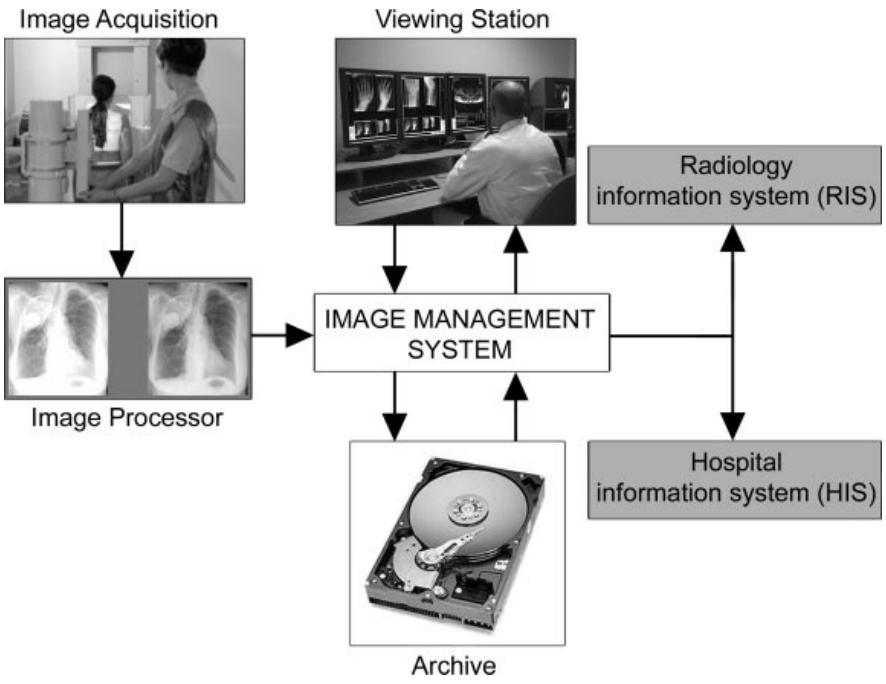

Figure 2.7: Digital radiography system [5].

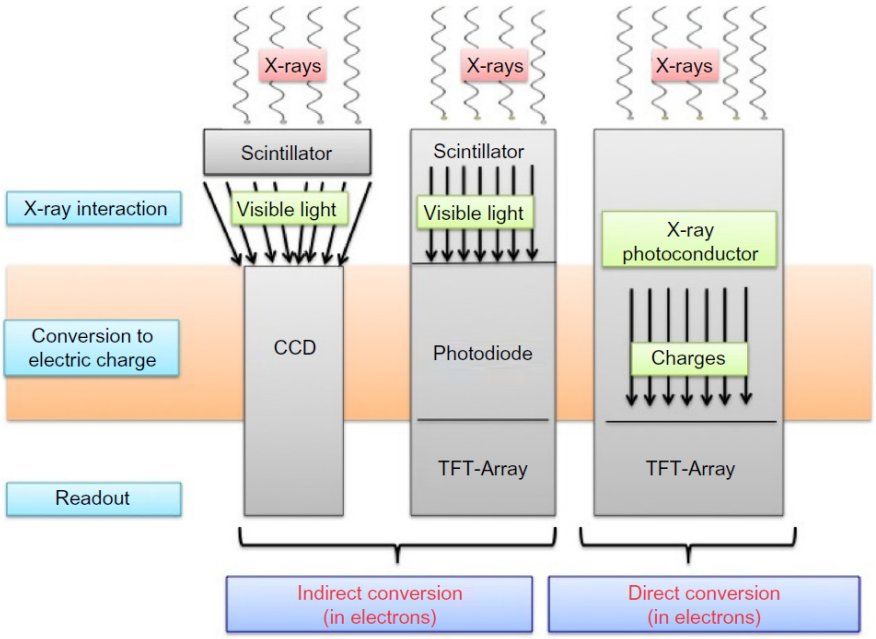

Figure 2.8: Direct and indirect conversion in charge-integration mode. [6].

CCDs

Scintillators convert X-rays to visible light, that is collected by bundles of optical fibers, coupled at the end to a visible CCD camera for radiography scan. The main characteristics of CCDs respect of films are:

- small active area (a few cm^2);
- very high spatial resolution;
- good dynamic range;
- linearity with exposure;

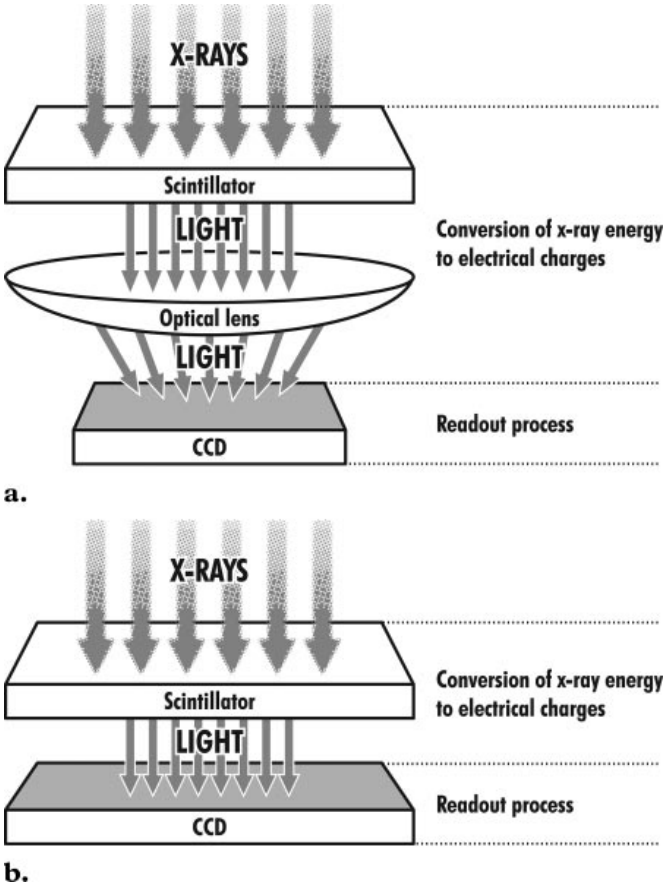

Figure 2.9: CCD device coupling with a lens (a) and in a slot scan configuration (b). [5].

In fig. 2.9a the system CCD + scintillator is coupled to a lens to bundle the emitted light for fitting of CCD chip, while the fig. 2.9b draws the slot scan configuration to move the detector of the same size of scintillator with the X-ray beam.

Flat panel detectors

The flat panel detectors (FPD) sum the advantages of having an electronic conversion of the radiation (CCD), to a large active area. Indirect FPD are made by a slab of scintillator coupled to a two-dimensional squared matrix of photodiode array in amorphous silicon (a-Si). It requires low voltage for biasing and can be machined with large areas (up to about $40\,x\,40|:cm^2$). Electric charges produced by a photodiode array are collected and processed by *thin-film transistors* (TFT), individually per each pixel. Despite the indirect approach is well known from many years, indirect conversion suffers from degradation of the spatial resolution and the noise level of a-Si is pretty high [6].

Photon counting

Ad already told, the detectors described in the previous sections are defined *digital* in the sense that they are able to convert the spatial information in a matrix of pixels with a digital scale (bits). But they are *analog* in the meaning of the charge generated by photon is integrated in the signal output (fig. 2.10b). New generations of X-ray detectors, based on solid-state C-MOS imagers or GEM (gas electron multipliers) gas detectors, opened the way for photon-counting imaging. Photons are counted one by one and its energy is estimated (fig. 2.10a). It offers unprecedented advantages [6]:

1. a general improvement of the physical parameters, on which imaging quality is based;

2. a energy discrimination in bands of the X-ray photons (*color X-ray radiography*).

The last development of the microelectronics allowed the realization of application-specific integrated circuit (ASIC) with millions of electronic components per mm^2. This highly integrated electronics, coupled to very small pixel size ($50\,\mu m$), reduces the electronic noise to the level about 50 e^- root mean square (rms), the effect is the detection of a single photon, even without cooling of the electronics. These detectors are called *noise-free* because the only uncertainty is due to the intrinsic statistical Poissonian fluctuation. Moreover the linearity response of electronic amplifier in a wide range of the input charge signal permits a full correspondence with the incoming photon energy [6].

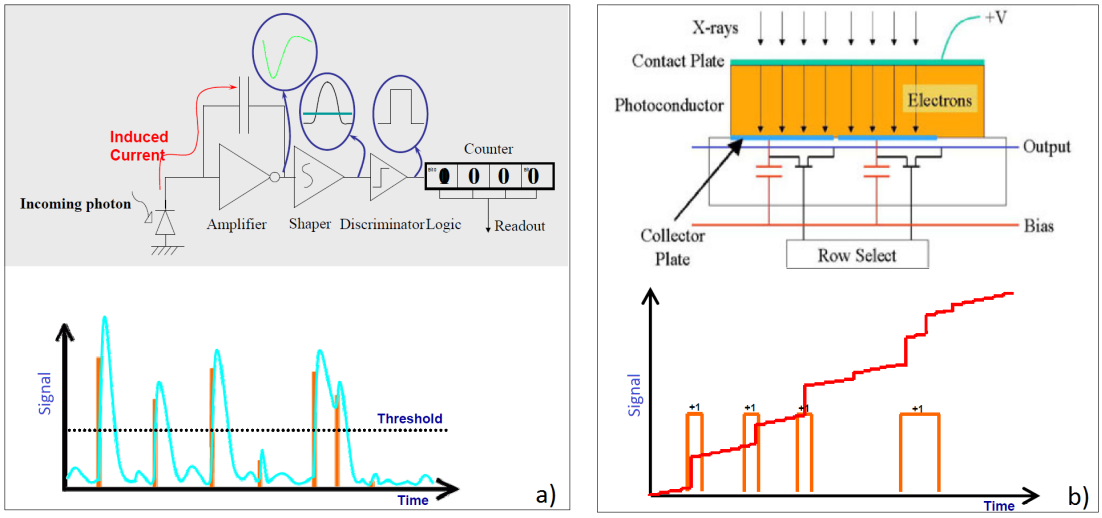

Figure 2.10: Photon (a) versus integrating counter (b).

Chapter 3

The pixel detectors

The word *pixel* (picture element) was introduced in imaging technology to indicate the smallest discernable element in a given device and the size of a pixel corresponds to the granularity of the image [7]. They come from R&D in particles physics. All the photons that interact with the pixel detector generate the image that it is composed by the integration of signal in each pixel of the imaging device. The object of this work is the characterization of a particular type of imaging device known as *hybrid* pixel detector: this definition originates from the fact that the sensor and the electronics are fabricated separately and than they are mated together. In this device (fig. 3.1) the ionizing radiation interacts with the sensor by photoelectric effect charge (photoelectrons), than the electric field moves the charge generating the electric signal. The electronic board amplifies, selects and stores the signal. The bias voltage that generate the electric field is function of the thickness and the material of the sensor. The main characteristics of the hybrid pixel detectors are:

- high speed;
- good time resolution and selectivity;
- stability;
- sensitivity.

Another very important peculiarity of this detector type, which is of fundamental importance in medical imaging application, is the capability to detect many events with a quasi-uniform spatial distribution on the sensing surface, so that the read-out electronics has not to select the position like in particle physics applications, but it can accumulate all the signal for a proper time to obtain a high quality image.

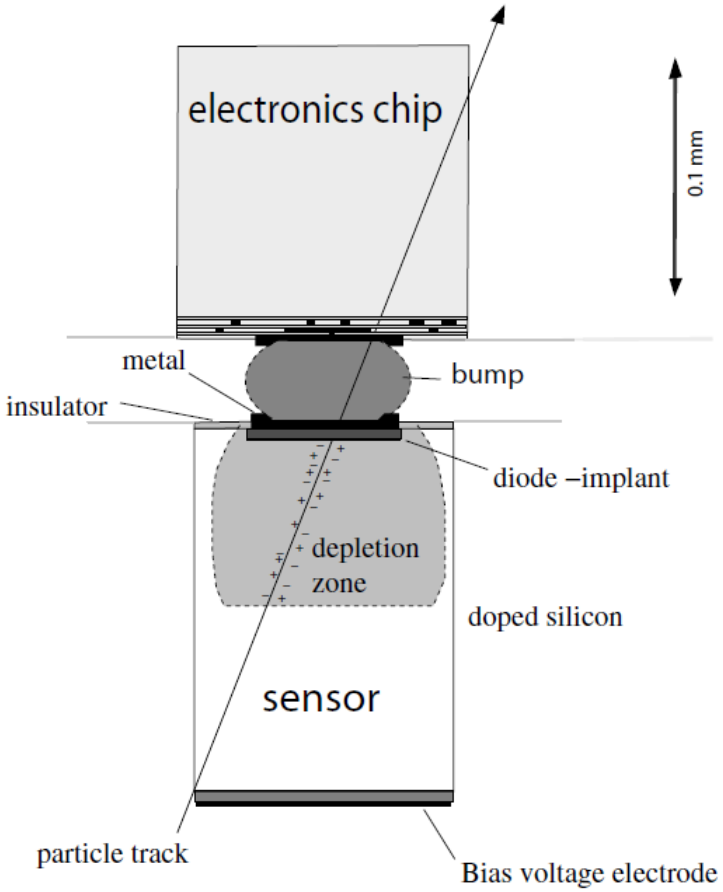

Figure 3.1: Sketch of an *hybrid* pixel detector [7]

3.1 An overview

The pixel detector could be considered an evolution of the micro-strip detector with an higher segmentation implant, in the sense that it is a 2-D expansion of the micro-strip detector. Each pixel is designed to have a properly electrical insulation from the neighboring sensing elements. The order of magnitude of the elemental pixel is below 1 mm^2 and their number is $10^4 - 10^5$. For this reason the connectivity of this high density pixel sensor with the electronic chip must be vertical and there must be a high precision and close (10-20 μm) contact between each pixel and his front-end electronics. Because the chip is very closed to the sensor, the designer must avoid:

1. the destructive sparks generated by the high voltage bias, confining the high voltage region inside an area defined by a guard ring;

2. high frequency pulse on electronics that induce a spurious signal using a low

swing logic signals and minimizing the capacitance between the sensor and the digital buses.

The very small dimension of a single pixel exhibits a low capacitance (0.2-0.4 pF) coming from the inter-pixel coupling rather than the backside plane: this avoids the phenomenon of the *cross-talk* between the neighbor pixels. The low capacitance is a very interesting advantage of this device because it can operate with a very low random noise of electronic origin [7]. So if the detector threshold is fixed to $10\sigma_{noise}$ practically no noise fluctuation exceeds the threshold. The small dimension of the pixel means also low leakage current, which allows the operation of the device also after a considerable irradiation.

3.2 The sensor

Since the '60 the semiconductor materials were used to assembly the sensor for spectroscopic measurements in nuclear physics. As the gas ionization chambers, also the semiconductor sensors convert the radiation in electric charge (signal). The process of charge production in semiconductor materials is more efficient than in the gas because the energy for producing a electron-hole pair (E_i) is lower of some factor (about 20 eV in a gas, 3.6 eV in silicon, 4.4 eV in cadmium telluride).

During the '70 the silicon became the principal semiconductor used in particle physics, but in the last years also other materials like CdTe, GaAs, SiC have been demonstrated a good quantum efficiency for the X-ray imaging application because they contain elements with a higher atomic number (fig. 3.2).

3.2.1 The sensor physics

The e-h (electron-hole) pairs are formed in the sensitive volume of the pixel detector and the average signal charge is [8]

$$Q_s = \frac{E}{E_i} e \tag{3.1}$$

where E is the absorbed energy, E_i the energy required to form a charge pair, and e the electronic charge. The ionization energy E_i is proportional to the bandgap, so higher bandgap materials yield less signal charge. For X-rays absorbed (E < 100 keV) the photoelectric charge generation is the prevalent interaction mechanism, the deposited energy is fixed, but the sensor must be sufficiently thick to provide good efficiency. The charge deposition is localized, with a charge cloud whose extent is determined by the range of the generated photo-electron. The charge pairs are created along the track with a range of order μm. The signal is formed when the generated charge carriers

Material	E_g (eV)	E_i (eV)	ε	μ_e	μ_h	$(\mu\tau)_e$	$(\mu\tau)_h$	ρ	$\langle Z \rangle$
Si	1.12	3.6	11.7	1350	450	> 1	> 1	2.33	14
Ge	0.67	2.96	16	3900	1900	> 1	> 1	5.33	32
GaAs	1.43	4.2	12.8	8000	400	$8 \cdot 10^{-5}$	$4 \cdot 10^{-6}$	5.32	31.5
Diamond	5.5	13	5.7	1800	1200			3.52	6
4H-SiC	3.26	8	9.7	1000	115	$4 \cdot 10^{-4}$	$8 \cdot 10^{-5}$	3.21	10
GaN	3.39	$8 - 10$		1000	30			6.15	19
InP	1.35	4.2	12.4	4600	150	$5 \cdot 10^{-6}$	$< 10^{-5}$	4.78	32
CdTe	1.44	4.43	10.9	1100	100	$3 \cdot 10^{-3}$	$2 \cdot 10^{-4}$	5.85	50
$Cd_{0.9}Zn_{0.1}Te$	1.572	4.64	10	1000	120	$4 \cdot 10^{-3}$	$1.2 \cdot 10^{-4}$	5.78	49.1
HgI_2	2.15	4.2	8.8	100	4	$3 \cdot 10^{-4}$	$4 \cdot 10^{-5}$	6.4	62
TlBr	2.68	6.5	30	30	4	$5 \cdot 10^{-4}$	$2 \cdot 10^{-6}$	7.56	58
a-Si	1.9	6	12	$1 - 4$	0.05	$2 \cdot 10^{-7}$	$3 \cdot 10^{-8}$	2.3	14

Figure 3.2: Physical parameter of principal semiconductor used for sensors

move, and than changes the induced charge on the sensor electrodes. When all charges have reached the respective electrodes (fig. 3.3), the variation in the induced charge, i.e. the integrated signal current, is equal to Q_s. A voltage is applied between the

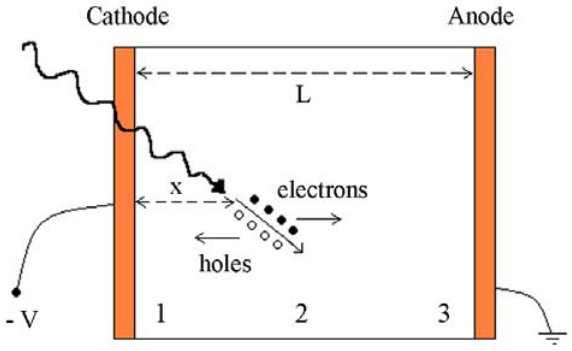

Figure 3.3: Mechanism of ionization and diffusion of charge in a semiconductor

electrodes to collect the charge carriers. As the carriers move through the medium they scatter and after a short transient the velocity depends on the magnitude of the local electric field. The carrier velocity is

$$\vec{v}(x) = \mu \vec{E}(x) \tag{3.2}$$

where μ is the mobility.

If the conductivity of a material is low, a high electric field can be reach with a small current: this signal are typically of the order of μA. The resistivity depends exponentially on the bandgap, so increasing the bandgap reduces the signal charge. The silicon resistivity is of order 10^4 Ωcm, which is too low; in a 300 μm thick sensor 30 V would lead to a high current flow of 100 mA and a high power dissipation of 3 W. The conductivity of semiconductors can be doped by introducing impurities into the lattice:

- if the dopant is of atomic number $Z+1$ (*n-type*), the external shell electron can be thermally excited into the conduction band, and it is available as mobile charge carriers;
- if the atomic number of the dopant is $Z-1$ (*p-type*), a little energy is needed to *borrow* an electron from a nearby atom and it acts like a positive mobile charge (hole).

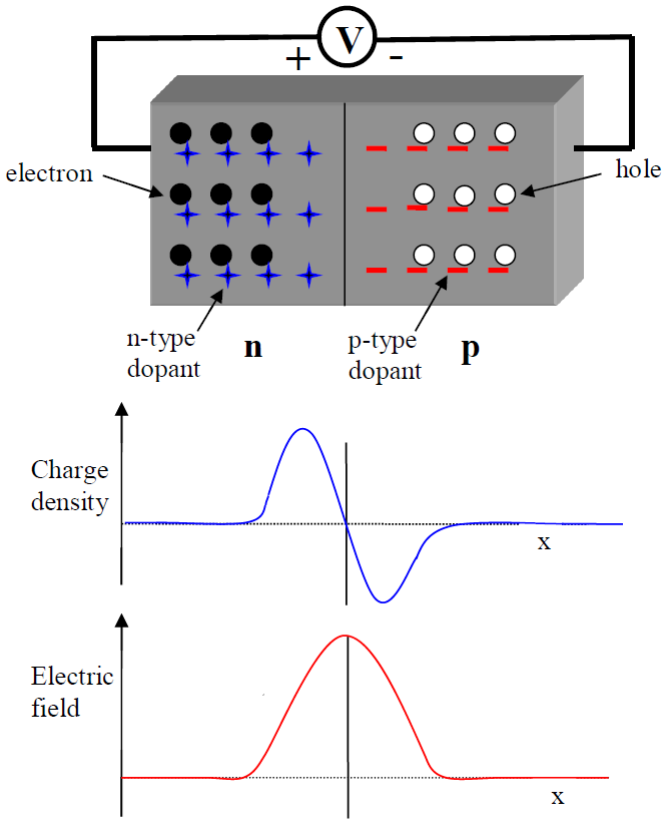

Figure 3.4: Reverse bias depletion applied to pn-junction (top). Charge density and electric field inside the diode.

Starting from a doped material it is possible to form a diode (*pn-junction*). Applying a positive polarity voltage on the n-side and negative on the p-side (*reverse bias*), the electrons on the n-side and the holes on the p-side are drawn away from the junction (fig. 3.4). The region around to the pn-junction is depleted of mobile charge and forms an insulator, over which the applied voltage builds up the desired electric field [8]. Thermal diffusion forms a depletion region also without applying an external voltage, so every pn-junction has an intrinsic *built-in* potential V_{bi}. The depletion width is generated by a V_b

$$w_d = \sqrt{\frac{2\varepsilon(V_b + V_{bi})}{Ne}} \tag{3.3}$$

where N is the dopant concentration in the bulk and ε the dielectric constant. When the depletion width is less then the crystal thickness, the diode is *partially depleted*, while if the w_d extends to the back contact the diode is *fully depleted*. The depleted volume is free of mobile charge and thus forms a capacitor

$$C = \varepsilon \frac{A}{w_d} = A\sqrt{\frac{\varepsilon Ne}{2(V_b + V_{bi})}} \tag{3.4}$$

Pixel capacitance

An important parameter of a pixel sensor is its capacitance because it determines the noise and the cross-talk between the neighbor pixels. The total capacitance C_t is defined as [7]:

$$C_t = C_{back} + C_{int} + C_{readout} + C_{bump} \tag{3.5}$$

where C_{back} is the capacitance to the backside, C_{int} is the sum of inter-pixel capacitance, $C_{readout}$ is the capacitance to the ground plane of the readout chip and C_{bump} the small contribution of the bumps.

The capacitance to the *backside* can be estimated with the formula (3.4) of parallel plate capacitor.

The *inter-pixel* capacitance represents the main contribution to the total capacitance. This component is proportional to the number of the neighbor pixels and so to the perimeter of the pixel, but also the gap size between the pixel implants give a contribution. Only a finite element simulation of the real topology of the pixels gives a good extimation of the inter-pixel capacitance. Also the experimental measurement of this quantity requires attention because of the small area to contact with special probe. A very interesting method is to bump bond a special router chip to the sensor instead of the readout electronics [7], giving a less sensitive response to systematic effect.

The charge deposited by the radiation on a pixel can induce via capacitive coupling a signal on its neighbors, this phenomenon is known as *cross-talk*.

3.2.2 Energy resolution

The process of charge formation in semiconductor sensors is stochastic and in this sense it is limited by fluctuations. Sensors convert absorbed energy into signal quanta. The deposited energy divided by the ionization energy yields the average number of signal quanta

$$N = \frac{E}{E_i} \tag{3.6}$$

This number fluctuates statistically, so the relative resolution is

$$\frac{\Delta E}{E} = \frac{\Delta N}{N} = \frac{\sqrt{FN}}{N} = \sqrt{\frac{FE_i}{E}} \tag{3.7}$$

The resolution improves with the square root of energy. F is the *Fano factor*, which takes in counts the multiple excitation mechanisms that reduce the overall statistical fluctuation. In a semiconductor absorbed energy forms electron–hole pairs, but also excites lattice vibrations, known as *phonons*, whose excitation energy is much smaller (the order of magnitude is some meV of energy). Thus, many more excitations are involved in the process of charge forming and this reduces the statistical fluctuations of the charge signal. In the energy deposition, excitations produce N_x phonons and N_{ion} ionization interactions form N_Q charge pairs. The energy deposited by the incident radiation is equal [8]

$$E_0 = E_{ion}N_{ion} + E_xN_x \tag{3.8}$$

where E_{ion} and E_x are the energies required for a single ionization or excitation, respectively. In a semiconductor E_{ion} is the bandgap and E_x is the average phonon energy. Considering that the excitation is a stochastic process following the Poissonian statistics, the variance in the number of excitation is $\sigma_x = \sqrt{N_x}$ and the variance in the number of ionizations is $\sigma_{ion} = \sqrt{N_{ion}}$. For a single event, the energy E_0 deposited in the detector is fixed. If the energy required for excitation E_x is much smaller than required for ionization E_{ion}, sufficient degrees of freedom will exist for some combination of ionization and excitation processes to dissipate precisely the deposited energy. Hence, for a fixed energy deposited in the sample a fluctuation in excitation must be balanced by an equivalent fluctuation in ionization:

$$0 = E_{ion}\Delta N_{ion} + E_x\Delta N_x \tag{3.9}$$

For many events the variances in the energy allocated to ionization and excitation must be equal $E_{ion}\sigma_{ion} = E_x\sigma_x$,

$$\sigma_{ion} = \frac{E_x}{E_{ion}}\sqrt{N_x}. \tag{3.10}$$

Extracting N_x from eq.3.8 and inserting in eq.3.10

$$\sigma_{ion} = \frac{E_x}{E_{ion}}\sqrt{\frac{E_0}{E_x} - \frac{E_{ion}}{E_x}N_{ion}}. \tag{3.11}$$

The total number of charge generated in the sensor is

$$N_{ion} = N_Q = \frac{E_0}{E_i} \tag{3.12}$$

and the variance of ionization processes can be written as

$$\sigma_{ion} = \sqrt{\frac{E_0}{E_i}} \sqrt{\frac{E_x}{E_{ion}} \left(\frac{E_i}{E_{ion}} - 1 \right)} = \sqrt{N_Q F}. \tag{3.13}$$

The second factor on the right-hand side is the *Fano factor* F. This is a very important formula for calculating the intrinsic resolution of semiconductor detectors

$$\Delta E_{FWHM} = 2.35 \cdot E_i \sqrt{N_Q F} = 2.35 \cdot E_i \sqrt{\frac{E_0}{E_i} F} = 2.35 \cdot \sqrt{E_0 E_i F}. \tag{3.14}$$

Usually the energy resolution response is measured in terms of *Full Width at Half Maximum* ($FWHM = 2.35 \cdot \sigma$) and indicates the width of the distribution (of Gaussian shape) at a level that is just half the maximum ordinate of the peak [2]. Detectors with good efficiency at X-ray energies typically have sufficiently small capacitance to mantain electronic noise < 100 eV FWHM, so the variance of the detector signal is a significant contribution. At energies > 100 keV the elevate pixel size tends to increase the electronic noise to dominant levels.

3.3 CdTe sensor

Since the 1960s the Cadmium telluride crystal has been studied as an X-ray and gamma ray detector material. CdTe has a cubic zincblende crystal structure with atomic numbers of 48 (Cd) and 52 (Te), and a large band gap of 1.44 eV, that means the sensor can operate at room temperature. A typical characteristic of this material is the disparity between electrons and holes mobility properties (fig. 3.2). The presence of defects and impurities in the crystals acts as trapping centres and causes a low values of the charge carrier mobility-lifetime products. Structural defects, impurities and complexes of the two (cadmium vacancies and donor impurities like Cl, In) are the typical defects in CdTe [9]. Gold and platinum (high work function) are used to generate the *ohmic* contacts while the *Schottky* detector has usually an indium–titanium multilayer contact (fig. 3.5 and 3.6).

The phenomenon of *polarization* is a critical issue for CdTe detectors because it determines it time instability under bias. This depends on the ionization of deep acceptor levels present in these crystals. The origin of the deep level can be attributed to the presence of a Cd vacancy in the crystals. A deep acceptor level can cross the Fermi level when the bands are bent due to the formation of a pn-junction. This causes

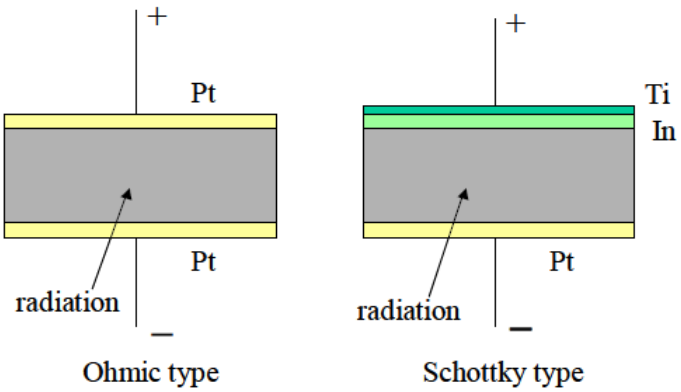

Figure 3.5: Ohmic and Schottky type of CdTe sensor [10].

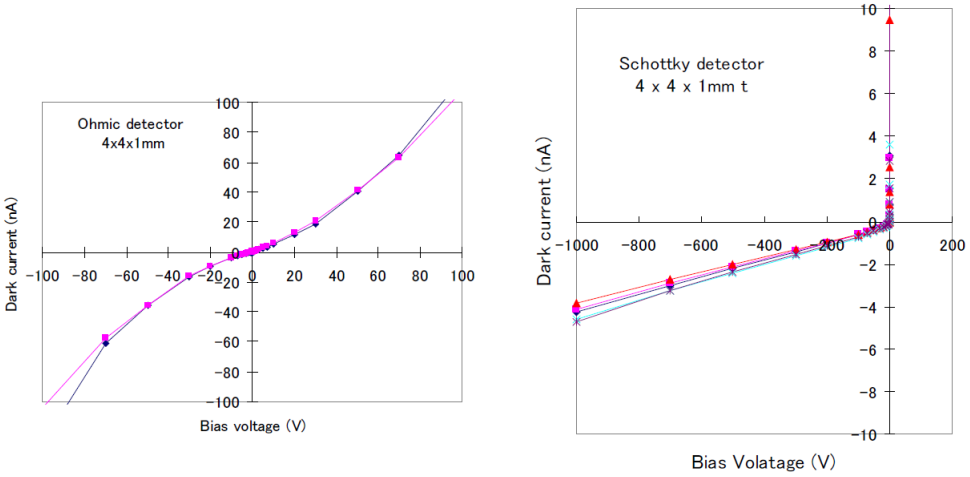

Figure 3.6: Typical current vs voltage curves of ohmic (left) and Schottky (right) detector [10].

the ionization of the deep acceptor levels, and the re-distribution of the initially uniform electric field, increasing at the positively biased electrode and decreasing at the opposite side. Hence a gradual reduction of the effective depletion layer width with time results [11]. Polarization leads to a time-dependent decrease in counting rate and charge collection efficiency. It is possible to minimize the polarization effects by using high bias voltages and low temperature operation. CdTe detectors with blocking contacts and cooled with compact Peltier cells shows better performance and time stability [9].

3.3.1 Fabrication

There are different techniques to grow an high purity CdTe crystals, such as zone melting, Bridgman method, epitaxial and travelling heater method (THM). The most used is the THM and doped with Cl to compensate background impurities and defects. The resulting substrate is a high resistivity p- type materials.

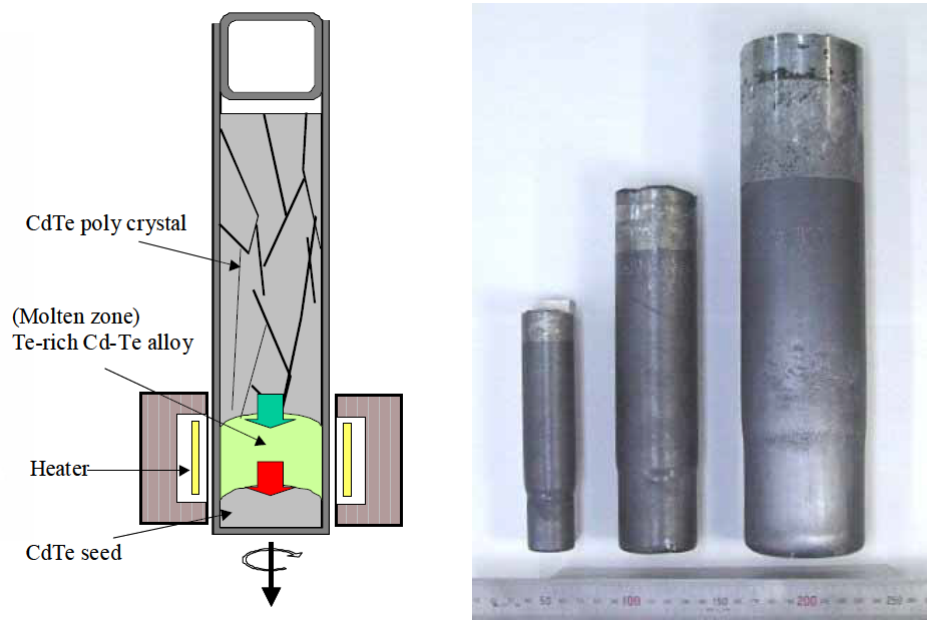

(a) Scheme of Travelling Heater Method (THM).

(b) Photo of some crystals: in the lower part the seed, in the middle the grown and in the upper the molten zone.

Figure 3.7: CdTe crystals [10]

The fig. 3.7 shows the process of growing of CdTe: a CdTe single crystal seed, Te-rich alloy and the CdTe poly-crystal rod are charged into the quartz ampoule, and after it is sealed with inert gas. For maximizing the resistivity and the carrier lifetime, the Te-rich alloy is doped with Cl adding $CdCl_2$. After heating up the oven, only the Te-rich alloy melts and the molten zone is formed. As the temperature of the lower end of the CdTe poly-crystal rod increases by moving down the ampoule slowly, the solubility of CdTe increases and the CdTe poly-crystal is dissolved into the molten zone. At the same time, the temperature of the upper surface of the CdTe seed decreases, CdTe is crystallized from the molten zone onto the seed. Finally, the whole CdTe poly-crystal rod is dissolved and re-crystallized on the CdTe seed by the travel of the ampoule in the whole length [10]. The phase diagram of CdTe (fig. 3.8) shows that it can be crystallized from the Te-rich Cd-Te solution at much lower temperature than the

melting temperature of stoichiometric CdTe, in this way the contamination from the quartz ampoule is ejected during the growth.

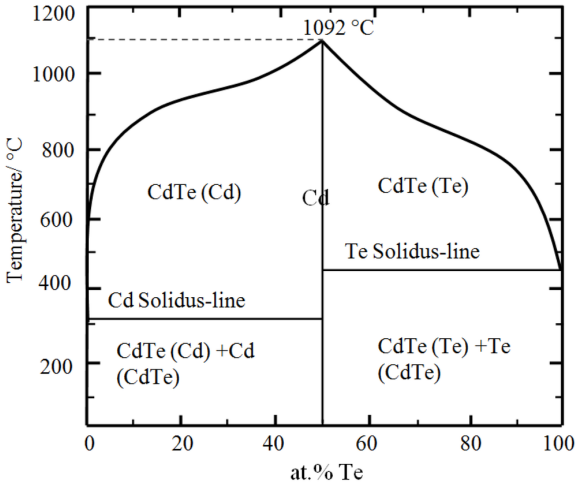

Figure 3.8: Phase diagram of CdTe.

3.3.2 Pixelisation process

There are two processes to pixelized a semiconductor sensor. In the first one passivation is used to protect the semiconductor surface from metal etchants used to pattern the deposited contact metal (fig. 3.9a). In the second one metal etchants are not needed at all (fig. 3.9b). AlN (aluminum nitride) passivation may be applied after lift off on the metal contacts deposited on a patterned layer of photoresist (avoiding the use of etchants), to ensure long term stability and to protect the surface during bump bonding. These processes assure an adequate inter-pixel resistances of the order of several hundreds of $G\Omega$ or more [12].

3.3.3 Bump bonding

The bump bonding technique is widely used by the electronic industry to couple the integrate circuits to PCB (printed circuit board). In particular the sensor in mounted on a CMOS ASIC (application-specific integrated circuit) chip for the signal readout using the technique of flip chip or bump bonded (fig. 3.10). The limiting size factor is the detector and CMOS processing technology. Usually CMOS technology allows a maximum circuit size of a few cm^2. The micro bumps are made of In or Pb/Sn (solder). Indium bumps are created on the pixel contacts of both the CMOS circuit and the Si or CdTe sensor by evaporation and lift off. Applying a well determined mechanical

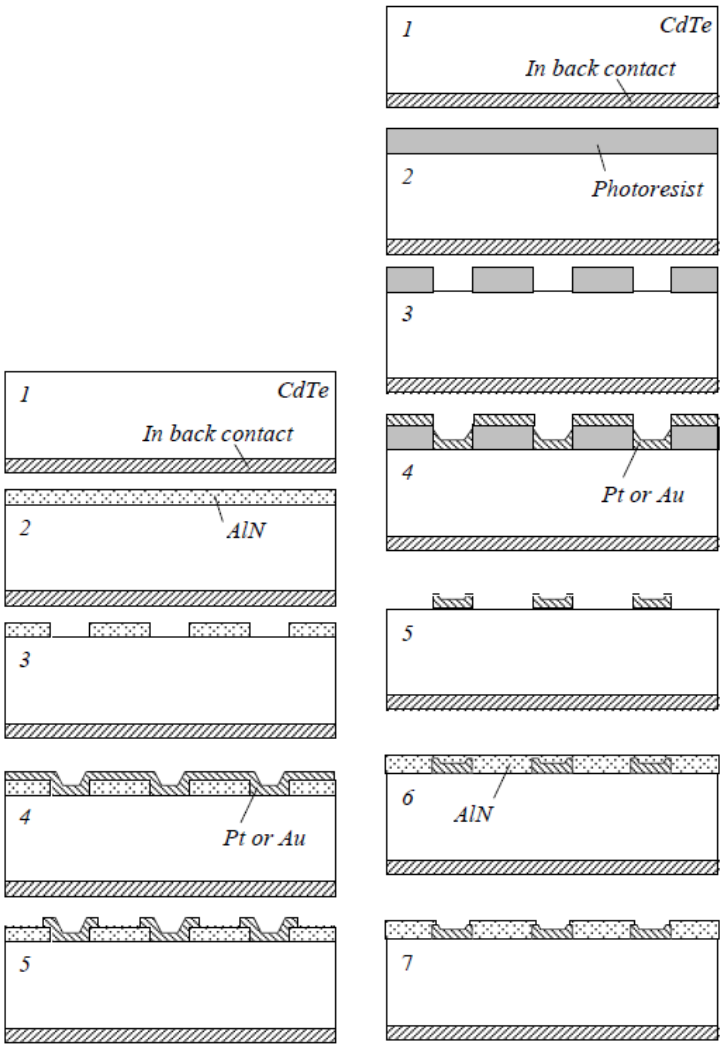

Figure 3.9: Steps of the two pixelisation processes [12]

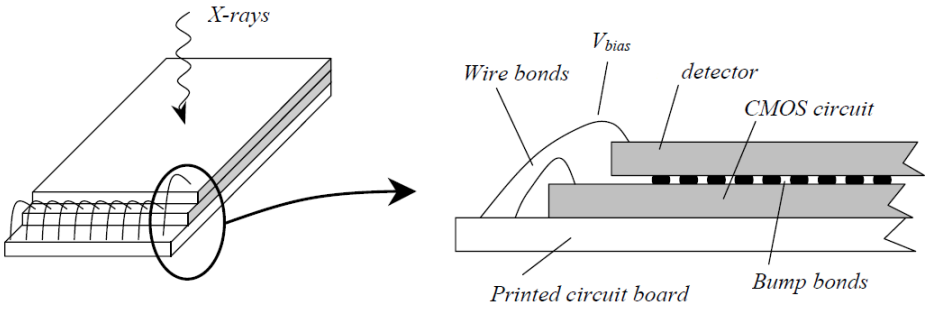

Figure 3.10: Sketch of a hybrid pixellated sensor [12].

pressure on the two aligned chips the flip chip connection with In bumps is performed. This process is very delicate because a dust particle or a lithography defect on a single pixel contact may cause the failure of the flip chip connection of the whole sensor [12].

3.3.4 Charge sharing effect

The CdTe sensors are electrically pixelated and not physically, so the e-h pairs generated by the radiation are free to move in the lattice volume according to the electric field imposed by the external bias voltage. During the drift of this charge towards the electrode a not negligible transverse spread cause a *charge sharing* between more neighbor pixel (the more probable event is the sharing between two pixels) (fig. 3.11) [13]. Many factors are on the base of this phenomenon.

The photoelectron range

A photoelectron is generated by the interaction of photon with the lattice and dissipated the energy along his path before to be absorbed. Electron-hole pairs are generated along the photoelectron path (for energies below 100 keV, the photoelectron range is no more than 40 μm) [13].

The fluorescence X-emission

When a x-ray is absorbed by a crystal, after the ionization of the atom a x-ray fluorescence emission follows the event, also this radiation is absorbed by the sensor material at some distance from the primary radiation. The principal energy lines for Cd are at 23 and 26 keV (K_α and K_β and at 27.5 and 31 keV for Te [13].

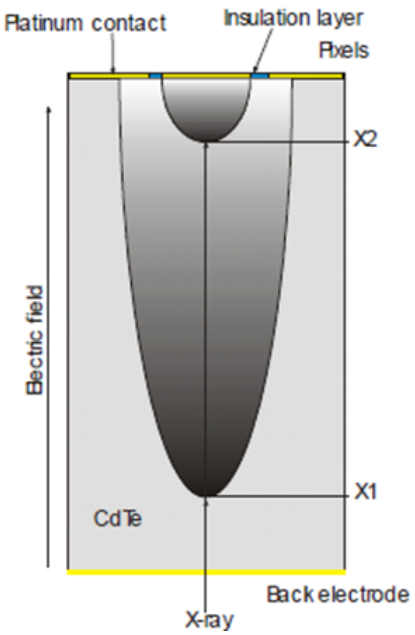

Figure 3.11: The charge sharing effect.

The carrier diffusion

The e-h pairs under the applied electric field are drifted toward the anode and the cathode inducing a current signal. The diffusion effect increase the size of the charge cloud. The solution of the diffusion equation give isotropic 2-D Gaussian with

$$\sigma = \sqrt{2D_n T_d} \tag{3.15}$$

where D_n is the diffusion coefficient for electrons and T_d is the drift time for the electron carriers to reach the anode, equal to

$$T_d(E) = \frac{d}{\mu_n V}(d - \frac{1}{\mu_{CdTe}(E)}) \tag{3.16}$$

where d is the crystal thickness, V is the bias voltage applied in the thickness z-direction, μ_n is the electron mobility and μ_{CdTe} is the attenuation coefficient of CdTe [13].

3.4 Front-end electronics

Electronics are a foundamental component of all modern detector systems. The scope of pulse processing and analysis systems is [8]:

- To acquire an electrical signal from the sensor (short current pulse).
- To drive the time response of the system to optimize
  1. the minimum detectable signal (detect hit/no hit),
  2. energy measurement,
  3. event rate,
  4. time of arrival (timing measurement),
  5. insensitivity to sensor pulse shape, or some combination of the above.
- Digitize the signal and store for subsequent analysis.

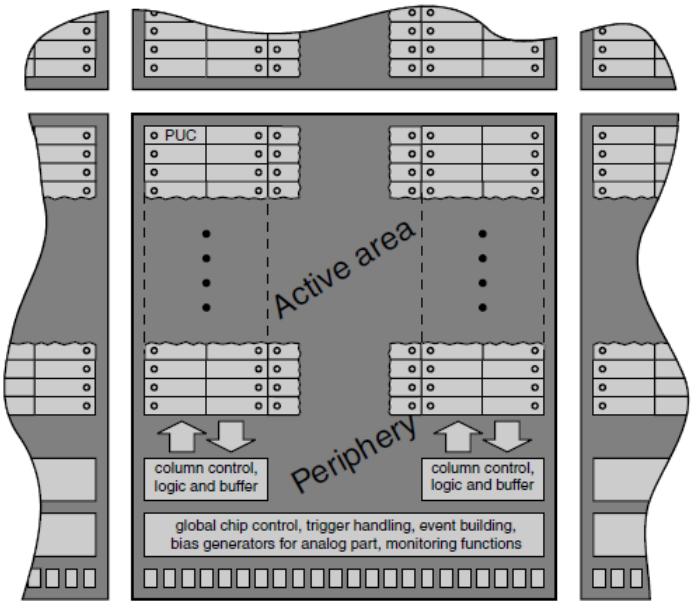

Figure 3.12: Generic geometry common to chips of hybrid detectors [7].

A large variety of pixel chips exists according to different geometries, readout philosophies, and analog circuits, but the building blocks architecture and properties are common. The chips are composed by an active area which contains a repetitive matrix of pixels and a chip periphery that controls the active part, where data is buffered and global functions common to all pixels are located. The wire bond pads for the connection are located only at the lower edge so that the chips can be coupled side by side to form a module. The gap between the chips is made as small as possible and so the size of the underlying sensor pixels must be increased only slightly. The constrains on the gap size are imposed by the tolerances in chip dicing and by the space required during the flipping procedure [7].

The sensor pixel determines the *active area* in which the *pixel unit cells* (PUCs) are located and grouped in columns according to the task (power, bias, and control signals), and the output data flow are routed vertically and only very few signals run horizontal. Two columns are often grouped together to *column pair* to share circuitry between pixels and to reduce cross talk between the digital and the analog sections.

The global control and bias section, and the wire bond pads are located in a repetitive blocks of the bottom part of the chip (*chip periphery*). The chip is endowed of an analog test pulse generator to inject known charges into the pixels. The bias signals for the analog sections in the PUCs is distributed by an interfaces to the columns, they provide buffered digital control signals, the buffer memory for the data. In the periphery are located also: the bias settings for DACs (digital-to-analog converters), the thresholds systems (global value and trim values) written in every PUC.

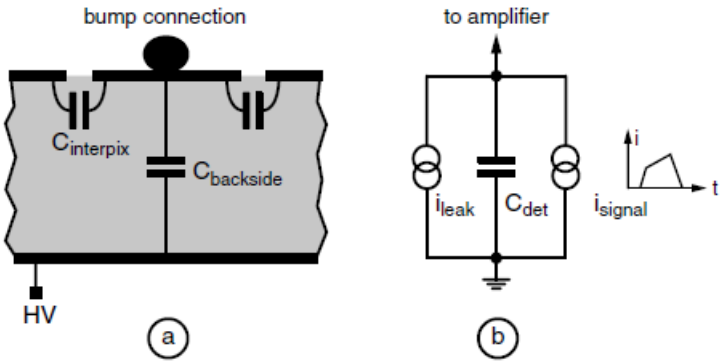

Figure 3.13: Simplified circuitry model of sensor [7].

As already illustrated in the previous sections, a sensor pixel can be modeled by the capacitances to the backside (C_{back}) and to the first (or more) neighbors (C_{inter}) (fig. 3.13a). Assuming as a first approximation that the neighbor pixels are held at constant potential by the connected amplifiers, the capacitances can be summed up leading to the effective detector capacitance C_{det} (fig. 3.13b). The leakage current is simulated in the model like a DC current source (I_{leak}). The charge (e-h pairs) produced by the interaction of radiation with the sensor is modeled by a time-dependent current source (I_{signal}). The exact temporal shape of this current signal depends on many factors like the position of the charge deposition, the sensor material properties (mobilities, trapping), the bias voltage, and the pixel geometry. The polarity of the signal is determined by the type of charge carriers collected on the pixel [7].

3.4.1 Pixel unit cell

A generic PUC model contains many circuit elements (fig. 3.14) some are very simple like the *bump pad* (for the connection to the sensor pixel), the *mask* (to disable the corrupted pixels), while others are more complex and of fundamental importance for the detector operation.

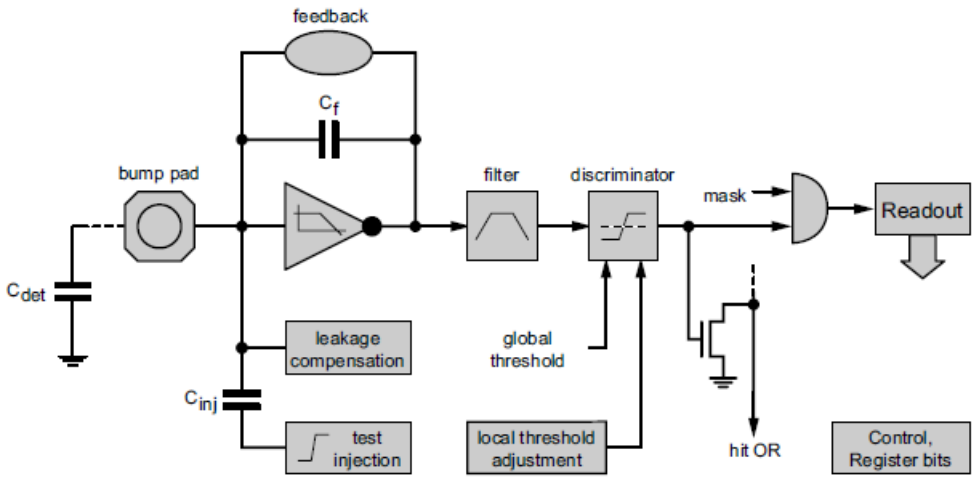

Figure 3.14: Simplified circuitry model of sensor [7].

The *charge-sensitive preamplifier* is an inverting amplifier with a feedback capacitor C_f converts an input charge Q_{in} to a voltage. The preamplifier is one of the most crucial parts in the PUC. It must provide an inverting gain of well above 100 with a sufficient bandwidth [7].

A *feedback circuit* is required to define the DC-operation point of the charge-sensitive preamplifier and to remove signal charges from the input node (or from C_f after the dynamic response of the amplifier) so that the preamplifier output voltage returns to its initial value [7]. To simplify this circuit it is possible to use a constant current discharge which has a saw-tooth-shaped output signals with a width proportional to the input charge. Measuring the width of the discriminator output pulse(*time over threshold* - ToT) it is possible to determine the deposited charge. The principal drawback is in high-rate applications due to the increasing dead time for large signal amplitudes [7].

The sensor pixels are usually DC-coupled to the preamplifier inputs so a *compensation circuit* for the leakage current must be implemented. A simple solution is the subtraction of a fixed current by measuring the leakage in some representative pixels. A very interesting designs use a current source in every pixel which is regulated such that the preamplifier output reaches a certain average DC-level. Because the signal

and leakage current can only be distinguished by their time profile, a very long time constant is involved in this solution [14][7].

A *discriminator* compares the shaper output (coming from the signal) to a threshold value which is distributed globally to all pixels. The threshold range is set in order to optimize the detection efficiency and the noise. Variations of the threshold of the individual pixels can lead to an increased noise hit rate or to a reduced sensitivity. So it is needed a *local threshold* fine-tuning in every pixel to compensate for these variations. In chips for X-ray detection there are two discriminators with different thresholds to distinguish between high- and low-energetic X-rays. The local threshold adjustment is most often implemented by simple DACs and several digital registers are needed in every pixel to store the trim values [7].

A very important circuit is the *test charge injection* of known charges into the preamplifier inputs. It is constituted by a known voltage step to a well-defined calibration capacitor C_{inj}. The voltage step can be supplied externally to the chip or generated in a chopper circuit in the chip periphery [7].

The hit information of the individual front-end chips must be sent to the *data acquisition* (DAQ) to process and storage. Serial links carrying digital or analog signals are normally used in order to reduce the number of cables.

In all the application in which the number of particles absorbed in every pixel during a given time interval must be determined (X-ray medical imaging, synchrotron radiation application) the hit signal is counted in every pixel and read out after the measurement interval. There are some technique to enlarge the dynamic range like the *wrap around* counter in which an overflow bit is set by the 16-bit wide counters when this happens. The total pixel count is calculated from the number of overflows and the remaining counter value. Some counting chips use two independent discriminators per pixel with different thresholds so that incoming hits can be stored in a low and/or high energies register. This device has many advantage like:

- to double the image information with a single shot of radiations;
- to halve the dose to a patient (medical application).

3.4.2 Threshold discriminator system

The photon counting detectors are equipped with circuitry that senses whether a pulse exceeds a threshold, this is a simple amplitude measurement known as *threshold discriminator system*. The fig. 3.15 illustrates a simplest scheme of threshold discriminator system at the output of the shaper. It provides a digital output whenever the shaper output exceeds the threshold level V_{th}. This amplitude evaluation yields only a on/off result, so it is also called *binary readout*. If the threshold coincides with the relative baseline (threshold *zero*) all of the signal pulses and all of the noise pulses will

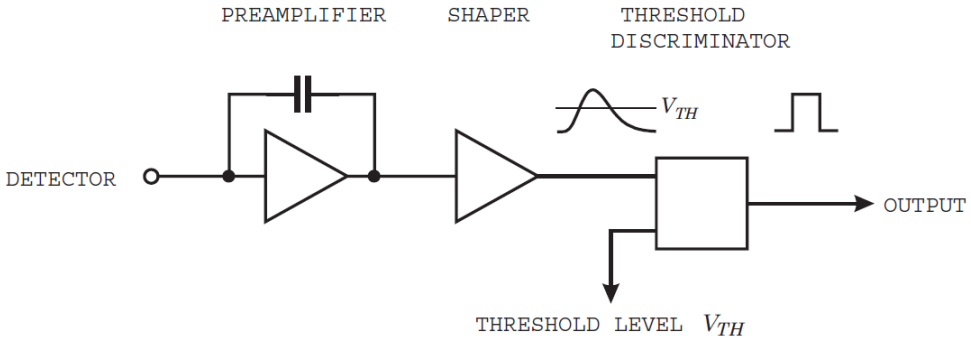

Figure 3.15: Thereshold discriminator system [8].

be recorded. The rate of noise hits can be reduced by increasing the threshold level. The fig. 3.16 shows some fraction of the noise pulses that exceeds the threshold [8]. In a binary system the threshold must be set optimizing the compromise between the

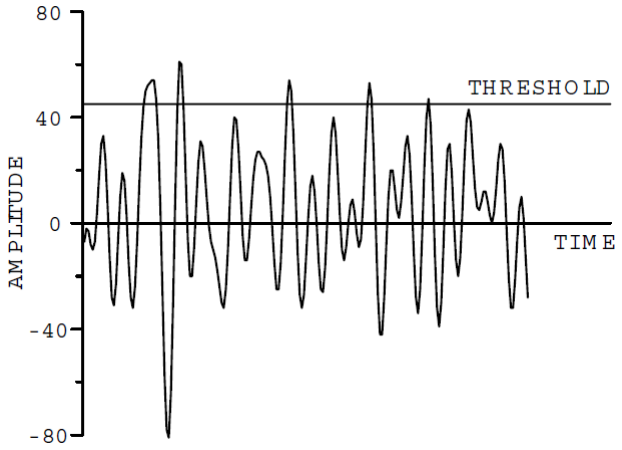

Figure 3.16: Amplitude vs time in a thereshold system [8].

exigence to include most of the signal and to cut the noise (fig. 3.17).

The noise level of a threshold discriminator system can be determined from threshold or signal scans. As already told in the previous section, test charge injection system, integrated in the PUC, applies a fixed signal amplitude. The threshold system scans all the range available (fig. 3.18):

1. initially all signal pulses will be counted,
2. the rate decreases, increasing the threshold values,
3. no signal is detected at highest threshold level.

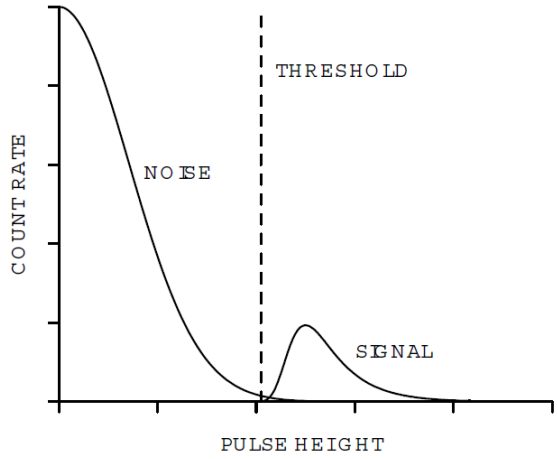

Figure 3.17: Signal and noise rapprensentation in a rate vs pulse height plot [8].

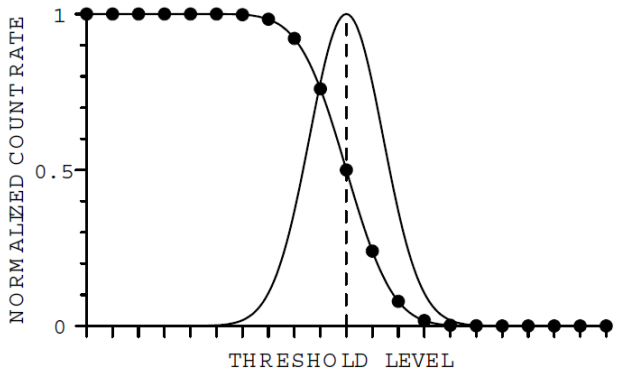

Figure 3.18: Thereshold scan for electronic noise meusurement using the charge iniection system [8].

The noise follows a Poisson distribution so

$$\sigma = \sqrt{Q_{inj}} = ENC \tag{3.17}$$

the variance of the injected charge Q_{inj} is known as *Equivalent Noise Charge*. This technique is applied also to Pixirad system as it will presented in the following chapters.

Chapter 4

Overview of the Pixirad system

This chapter is devoted to present an innovative X-ray imaging sensor with intrinsic digital characteristics based on Chromatic Photon Counting technology. The system counts individually the incident X-ray photons and selects them according to their energy to produce two color images per exposure. The energy selection occurs in real time and at radiographic imaging speed (GHz global counting rate). Photon counting, color mode and a very fine spatial resolution (more than 10 l.p./mm at MTF50) allow to obtain a high ratio between image quality and absorbed dose. The individual building block of the imaging system is a two-side buttable semiconductor radiation detector made of a thin pixellated CdTe crystal coupled to a Very Large Scale Integration (VLSI) CMOS pixel ASIC (Application Specific Integrated Circuits). Modules with 1, 2, 4, and 8 block units have been built, the largest one has a 25 x 2.5 cm^2 sensitive area. Results and images obtained from testing different modules are presented in this chapter [15].

4.1 Introduction

Over the last ten years the Fermi group of INFN Pisa has developed a new technology for imaging detectors, it is based on the coupling of a photon to charge converter (sensor) to a pixelized charge collection plane.The innovation of this device lies on the use of a chip ASIC that overcomes the inherent limit in the conventional spacing of the pixel arrays based on the PCB read-out approach. In this way it is possible to realize, at the same time, the charge collecting anode structure and the read-out electronics [16]. The typical miniaturization of the micro-electronics opens new frontiers in purely scientific (X polarimetry for celestial sources) and medical applications (chromatic single photon imaging in mammography) utilizing a crystalline cadmium telluride (CdTe) sensor.

Pixirad [17], a INFN spin-off, aims to develop and commercialize this last tech-

nology based on the **Chromatic Photon Counting**. This imagine methods permit to count individually the X-photons interacting with the detector distinguishing them according to their energy. This feature, associated with the high spatial resolution (50 μm step) allows to maximize the relationship between image quality and absorbed dose. The energy selection of the radiographic beam occurs in real time and with a single exposure, thus allowing to obtain a radiological chromatic imaging and significantly increase the information content of the images (table 4.1). The individual Pixirad block is a two-side buttable semiconductor radiation detector made of a thin pixellated crystalline cadmium telluride (CdTe) coupled to a large area VLSI CMOS pixel ASIC (512×476 pixels).

Table 4.1: Information content of the images

Energy range	$2-100$ keV
Count rate	>30 GHz

4.2 The sensor

The base block of the Pixirad system is realized by coupling, with the flip-chip bonding (bump-bonding) technique, an X-ray sensor made of a thin layer of crystalline cadmium telluride (CdTe) to a matrix of 512×476 pixels microcircuits (ASIC CMOS), figure 4.1. The detector is able to count the X-ray photons transmitted through the object and converted in two energy bins in each pixel of the CdTe sensor. The system therefore has a hybrid architecture in which the sensor and readout electronics are manufactured and processed separately. The sensor is segmented with the same ASIC geometry. Starting from the base block, a complete imaging system is obtained by coupling a number of blocks along one direction and then operating in slot-scanning or in full-field imaging mode. The width of the dead-space area (currently set at two pixels) is determined by the width of the high voltage guard-ring built on the radiation sensor.

In the digital radiography market Pixirad is an innovative, high quality system being:

- intrinsically digital
- noise free, due to the photon counting technique
- with optimal values of contrast and spatial resolution
- with high frame rate ($\sim$ 100 frame/sec)

- with capability to separate the image in various color components depending on the incident radiation energy
- with capability to operate in dead-time free mode (reading of one counter while taking data in the other one)

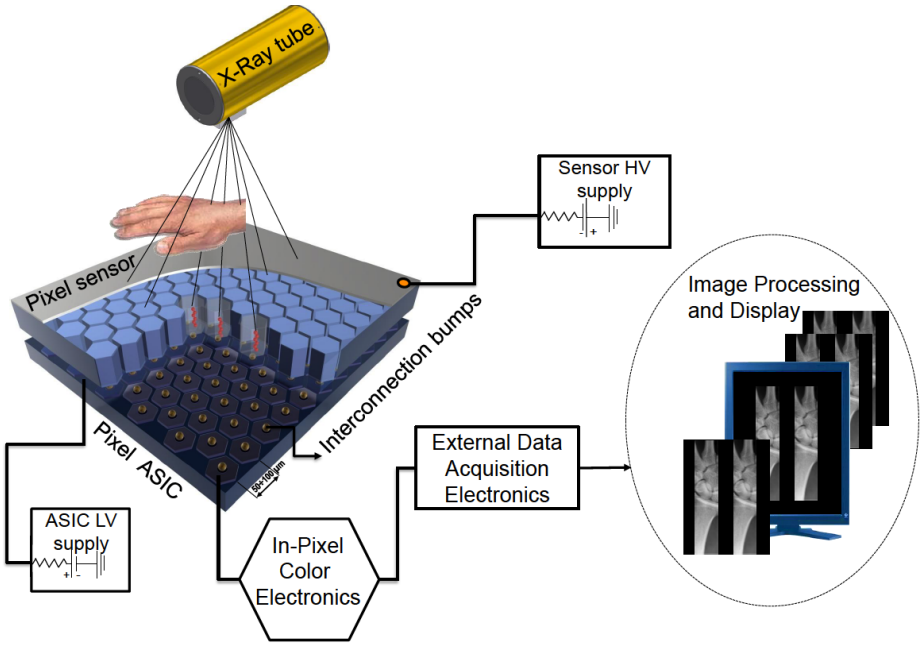

Figure 4.1: Principle of operation.

The CdTe detector (ACRORAD Co., Ltd., Japan) is a pixellated 650 μm thick Schottky type diode, with electrons collection on the pixels (fig. 4.2). The pixels are arranged on a hexagonal matrix with 60 μm horizontal pitch and 51.96 μm vertical pitch (fig. 4.3). The radiation receiving side of the CdTe crystal is metalized with a continuous Pt layer while the contacts on the pixel side are made through the deposition of successive Al, Ti, Au, Ni, Au thin metal films. A negative bias voltage is applied to the sensor using a tiny wire glued in a corner of the top Pt layer. The sensor is characterized by a very low leakage current ($5 nA \cdot cm^{-2}$) at 300-400 V when operated at reasonably low temperature (typically $-20°C$ in our case).

4.3 The ASIC

The CMOS VLSI chip has an active area of $30.7 \times 24.8 mm^2$, organized on a matrix of 512×476 pixels: it is the biggest ASIC ever produced (fig. 4.4) and the chip

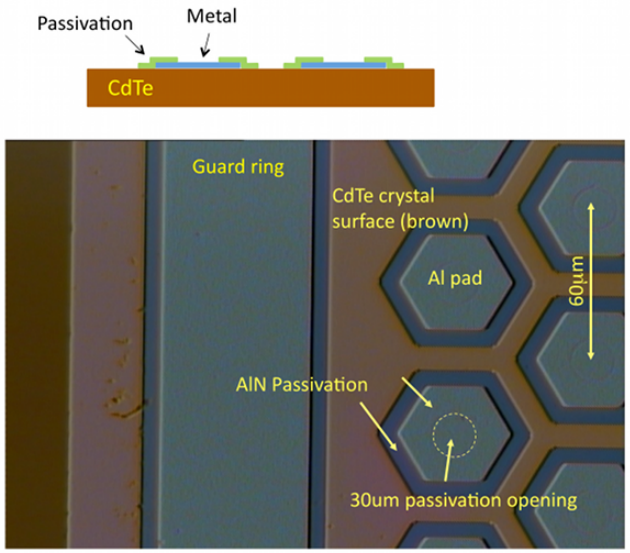

Figure 4.2: CdTe sensor.

integrates more than 350 million transistors. Each pixel incorporates a hexagonal electrode (top metal layer) connected to a charge amplifier which feeds two discriminators and two 15-bit counters. During data acquisition, the shift registers are clocked by the trigger generated by their respective discriminators. The pixels in the matrix are organized as 256 column pairs, each column pair having its own controller. In readout mode, the registers of several columns of pixels are serialized under the control of an external clock signal. The serialization of the column pairs is user-programmable: groups of 16, 32, 64 or 128 columns can be built, corresponding respectively to 32, 16, 8 or 4 active data output pads [15].

To reduce unavoidable variations of the DC level between the pixels, a self calibration circuit has been implemented in each pixel. In this way a global threshold per discriminator can be applied to the entire matrix. The intrinsic pixel amplifier noise is 50 electrons (rms). This level of electronic noise is achieved by taking advantage of the extremely low pixel capacitance (few fF) and the relatively long amplifier shaping time (pulse width 1 μs at the base). The acquisition can be done in a 2 color reading (2 thresholds, 2 counters) or, alternatively, by counting in one counter while reading the other one (dead-time free mode). The reading mode could be expanded to more colors by adding more counters: a particularly suitable solution for industrial applications such as non-destructive testing. Anyway, the actual counting configuration is maximized for an ultra high performance in digital mammography characterized by very fine position resolution, high sensitivity and DQE - Detective Quantum Efficiency.

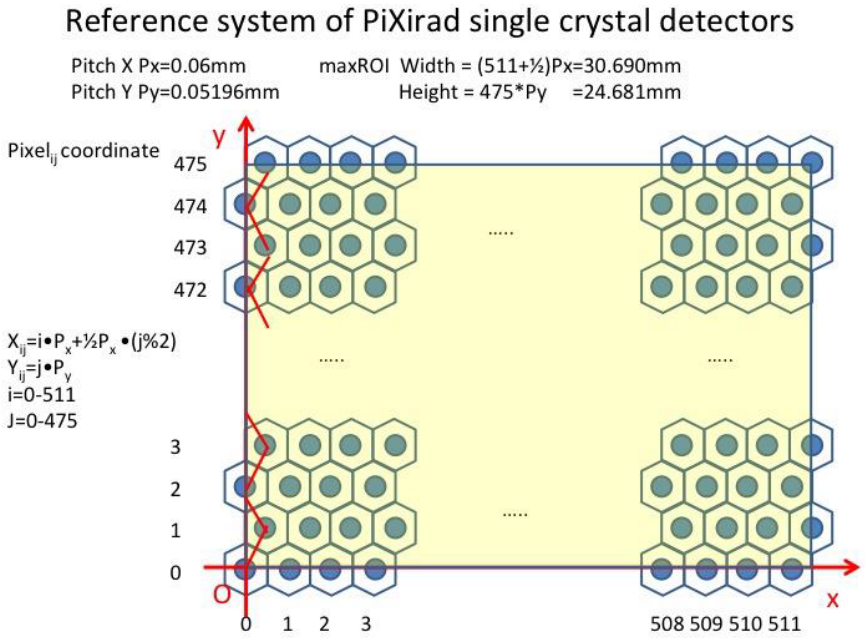

Figure 4.3: Scheme of the hexagonal pixels of the detector arranged in honeycomb matrix.

4.4 Images and performances

Testing of several configurations of the Pixirad imaging system has been performed. Modules with one (fig. 4.5), two (fig. 4.6), four and eight Pixirad blocks have been assembled. The two pixels dead-space between the blocks is usually removed from the images by off-line interpolation. The modules are able to deliver clear, highly detailed, noise free X-ray images to be used in medical, biological, industrial or scientific applications over the energy range 1-100 keV. The low energy limit is set by the minimum applicable global threshold, which is 200 electrons. Images are usually obtained at very high count rate (> 30 GHz for a 4 tiles module) by illuminating the samples with radiation from high power medical or diffraction X-ray tubes [15].

4.4.1 Chromatic photon counting

fig. 4.7 shows an example of chromatic photon counting with a single block module, Pixirad-1. Two images of a small dry animal are obtained by simultaneously counting the X-ray photons with a low energy threshold, fig. 4.7a, and a higher threshold, fig. 4.7c shows the image obtained by subtracting the two previous pictures one from the other and it contains mainly the low energy photons of the incident X-ray beam. Because the images of fig. 4.7a and fig. 4.7b are not statistically independent

Table 4.2: The CMOS ASIC characteristics

Shaped pulse duration (at the base)	1 μs (adjustable)
Linear range	> 3000 electrons
Saturation level	> 6000 electrons
Equivalent noise charge (ENC)	50 electrons (rms)
Residual offset after self-calibration	$\pm$ 30 electrons
Dynamic range	32768 counts (15 bit)
Input signal polarity	positive or negative
ASIC power consumption	3 W
Possibility to disable or by-pass pixels	user-selectable
Serialization of number of columns for best readout time	16, 32, 64, 128
Max readout clock frequency	200 MHz
Typical readout clock frequency	50 MHz
Readout time for 32 data outputs = 16 columns serialized (16 columns x 476 pixels x 15 bits x 20 ns) 50MHz	2.4 ms (per counter)
Readout time for 16 data outputs = 32 columns serialized	4.8 ms (per counter)
Readout time for 8 data outputs = 64 columns serialized	9.2 ms (per counter)
Readout time for 4 data outputs = 128 columns serialized	18.4 ms (per counter)

but fully correlated (they are obtained using the same photons), no further statistical noise is introduced by the subtraction process [15].

4.4.2 Low energy sensitivity

The sensitivity of the Pixirad sensors to image low energy X-ray photons is shown in fig. 4.8. Here, images of a very low contrast object (a jasmine flower) are taken at a global threshold of 200 electrons (corresponding to 1 keV energy, fig. 4.8a) for counter 1, and 1200 electrons (corresponding to 6 keV energy, fig. 4.8b) for counter 2. For a better visualization of the differences in contrast between the images at 1 and 6 keV thresholds, two different Look-Up Tables (Grays and ICA) are used [15].

4.4.3 High energy sensitivity

The image of a resolution phantom taken with a tungsten anode X-ray tube set at 90 kVp with 2 mm Aluminum filter, is shown in fig. 4.9. The lines are metal strips embedded in a 5 mm thick FR4 substrate (vetronite). The resolving power of the imaging system is good also at this high photon energies. This is shown by the capability to distinguish the two closest lines (50 μm wide with 50 μm separation). Fig. 4.9 shows a profile plot taken across the last two couples of lines on the left side. No significant

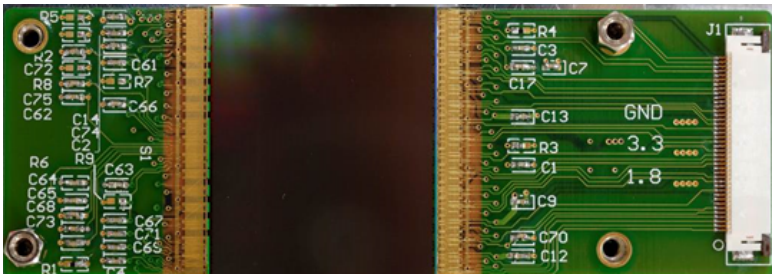

Figure 4.4: CMOS ASIC PIXIE II.

Figure 4.5: Pixirad-1 detector module unit

geometrical magnification has been used in the experimental set-up (source – detector distance = 50 cm, object-detector distance = 5 mm) [15].

4.4.4 Radiographic system: Pixirad-8

The main components of the simplest radiographic system consist of an X-ray tube and a detector. Modern X-ray systems often include objects for patient positioning, radiographic grids and other filters, as well as an array of detector choices. A mammography unit is a rectangular box that houses the tube in which X-rays are produced. The unit is used exclusively for X-ray imaging of the breast, with special accessories that allow only the breast to be exposed to the X-rays. Attached to the unit is a device that holds and compresses the breast and positions it so images can be obtained at different angles.

In our laboratory we have a mechanical system to reproduce the main features of a mammography system (fig. 4.10). It is a slot type scanning, in which the complete image is formed through a series of acquisitions obtained with shifting the sensor step

Figure 4.6: Pixirad-2 detector module unit

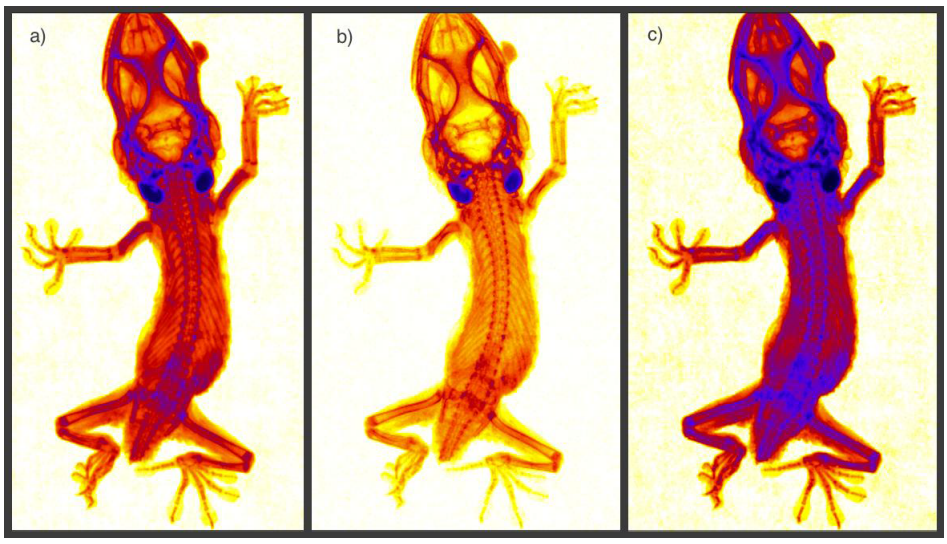

Figure 4.7: Images of a small dry animal obtained by simultaneously counting the X-ray photons (20 kV) with: a) a low energy threshold for counter 1 (all photons); b) a high energy threshold for counter 2 (high energy photons); c) subtracting the counts in the pixels of image b) from the corresponding counts in the pixels of image a). The result is a higher contrast, low energy, image.

by step along a circular arc. It is designed by STM Electronics (Verona, Italy) in collaboration with Pixirad in the framework of an R&D project supported by Regione Friuli-Venezia Giulia (Italy) [18] and it is composed by:

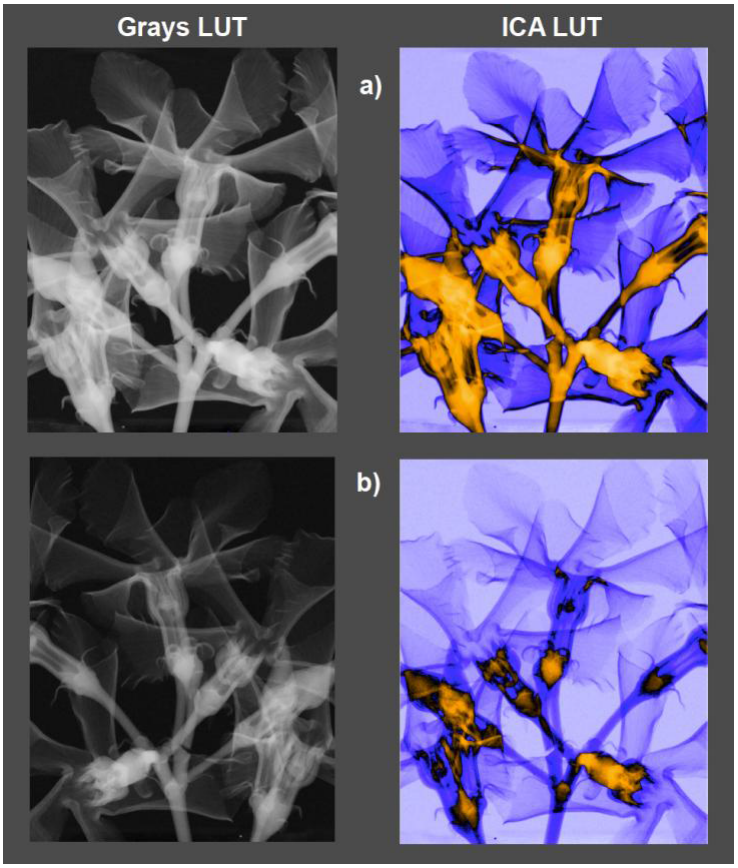

Figure 4.8: Images of a very low contrast object (a jasmine flower) taken: a) at a global threshold of 200 electrons (1 keV energy, LOW counter), and b) at 1200 electrons (6 keV energy, HIGH counter). False-colours are used to improve contrast.

- X-ray tube;
- Pb collimator;
- a carbon fibre plane for supporting the sample to be analysed;
- detector (Pixirad-8);
- electric motor for moving the detector.

Digital mammography is one of the most demanding X-ray imaging applications characterized by very fine position resolution, high sensitivity and DQE.

For this last purpose has been developed a prototype of detector which couples 8 units reaching the considerable dimensions of $25 \times 2.5 cm^2$ of active area and 2 Mega pixels called Pixirad-8 (fig. 4.11).

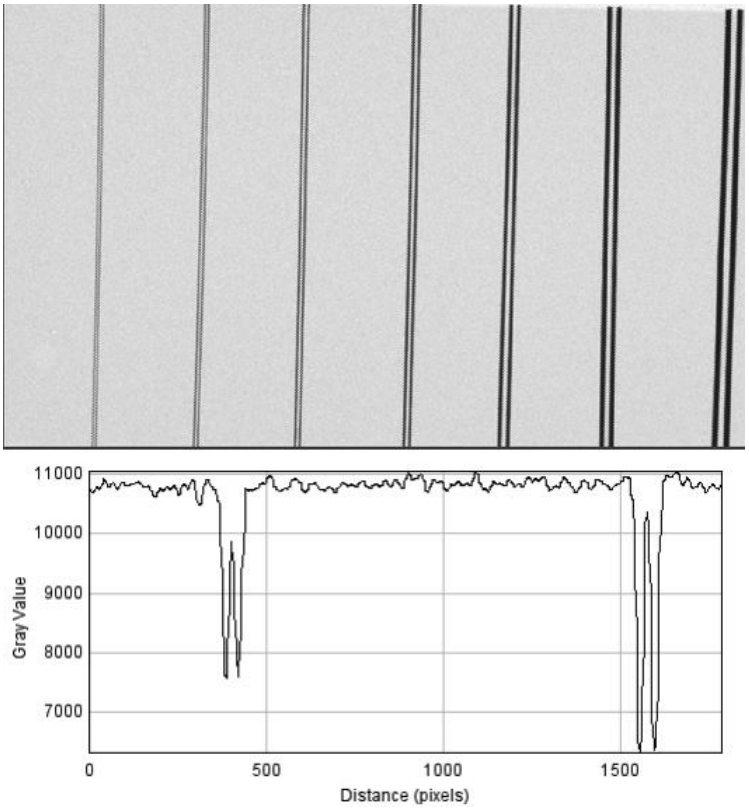

Figure 4.9: Image of a resolution phantom taken with a W anode X-ray tube set at 90 kVp. The plot is a profile across the last two couples of lines on the left. The closest lines are 50 μm wide 50 μm separation.

A single shot X-ray image of a man watch with its leather bracelet taken with Pixirad-8 is shown in fig. 4.12. The watch is made of plastic and metal parts. The top image (taken at low threshold) better visualizes weakly absorbing materials (plastic, leather) while the bottom image (high threshold) better visualize the metal parts.

In conclusion the Pixirad X-ray sensor is an innovative, high quality, noise free, chromatic imaging system. Its main characteristics are:

- large area of the elementary building block;
- high values of contrast and spatial resolution;
- wide energy range (CdTe radiation sensor);
- high frame rate ;
- capability to separate the image in various color components depending on the incident radiation energy;

- capability to operate in dead-time free mode (reading one counter while taking data in the other one).

The presented X-ray imaging system is the technological platform of Pixirad Imaging Counters s.r.l., a recently constituted INFN spin-off company [15].

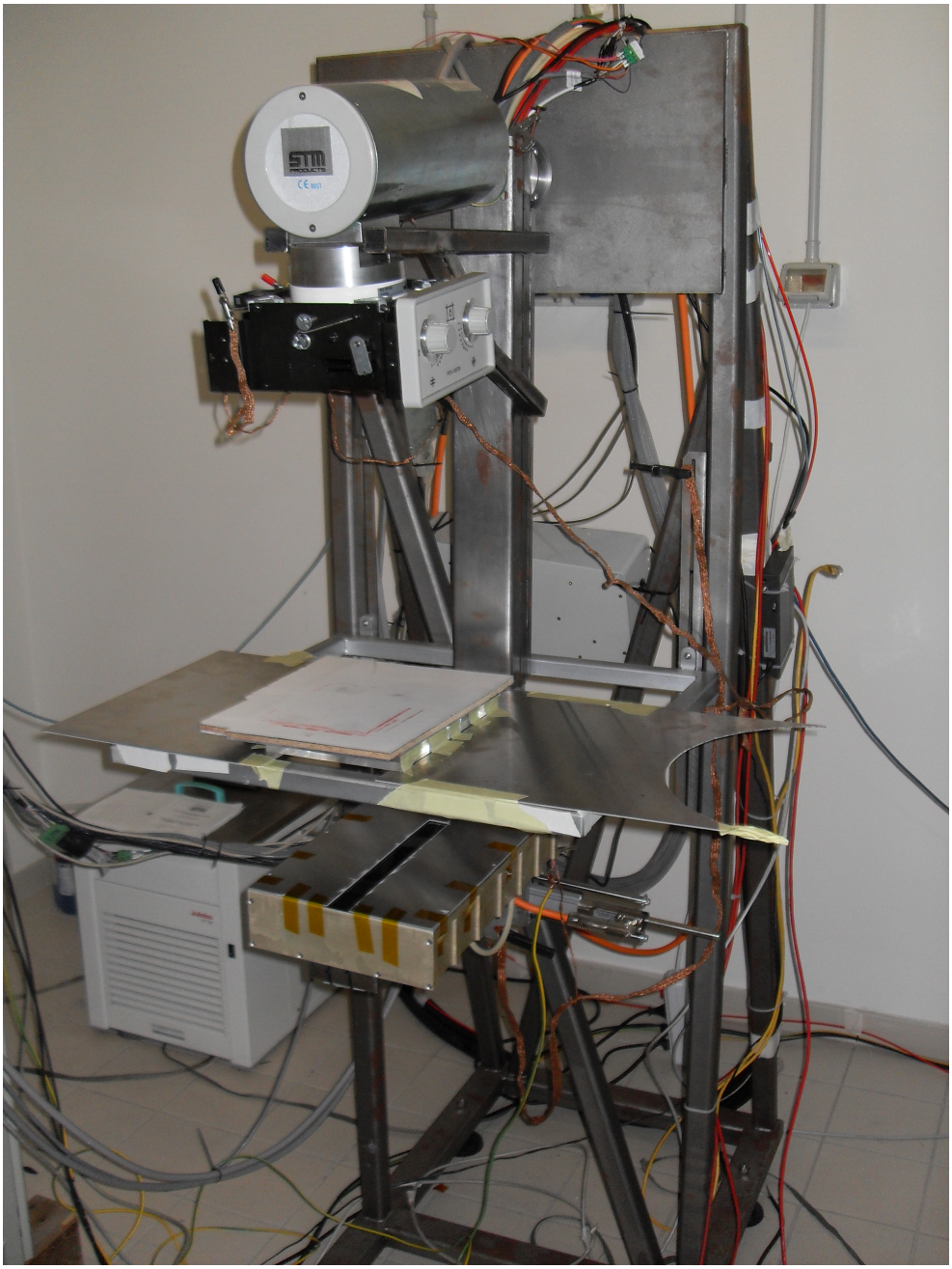

Figure 4.10: Mechanical apparatus reproducing mammography system

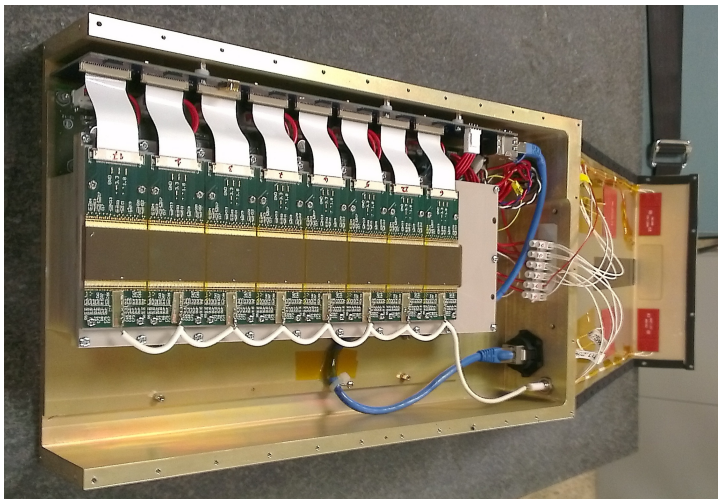

(a)

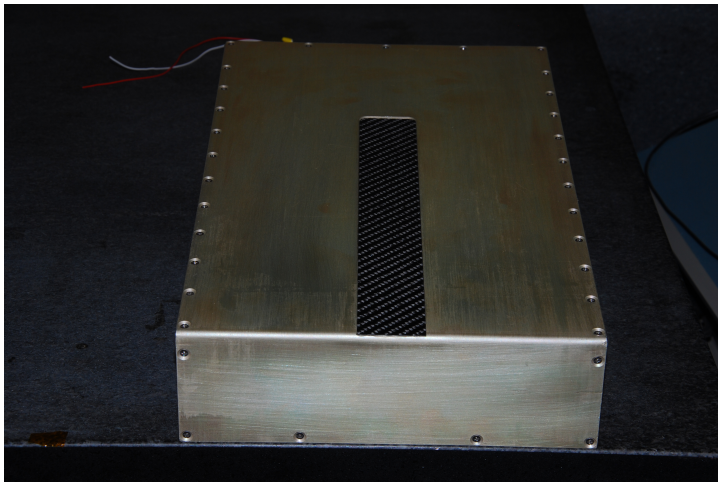

(b)

Figure 4.11: Pixirad-8.

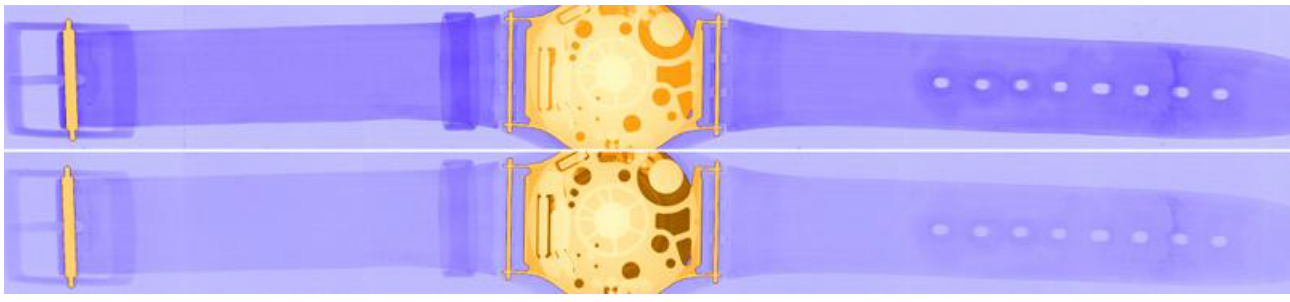

Figure 4.12: A single shot X-ray image of a man watch with its leather bracelet taken with Pixirad-8

Chapter 5

Energy characterization of Pixirad-1

This chapter is focused on the characterization of the Pixirad-1 detector system from the spectroscopic point of view [19]. An energy calibration has been carried out using different X-ray sources such as fluorescence lines, synchrotron radiation and radioactive elements. The energy resolution has been measured as function of the energy and the results have been compared with theoretical estimations. Finally, the charge sharing fraction has been evaluated by exploiting the monochromatic Elettra synchrotron beam.

5.1 Introduction

In general, the main advantages of photon counting over integrating detectors are:

- the capability to select the energy detection threshold for photons is counted, suppressing the noise;
- the capability of the energy-based discrimination of photons, allowing multi-spectral imaging.

This second advantage is enhanced in the Pixirad-1 system by its dual color feature. To be *spectrally* useful, and to evaluate the energy resolution, a photon counting system has to be energy calibrated. The aim of the calibration is here to find the relationship between the discriminator threshold voltage V_{th} (voltage driving the threshold of the discriminator in one color mode) and the corresponding photon energy. Since the V_{th} value has the same effect on *th-low* and *th-high* in two colors mode, the calibration in one color mode has been performed.

In this work a system with a 650 µm thick CdTe crystal, Schottky type, with electron collection on the pixels has been characterized. Due to the detector thickness and the small size of the pixels, charge-sharing effects between adjacent pixels are

anavoidable. Many complex and interconnected phenomena are involved in the spatial spread of charge carriers in CdTe detector material. Over all, the major factors influencing the charge sharing are the photo-electron ranges and the charge diffusion. In details, an X-ray photon absorbed in CdTe generates a photo-electron that loses energy along its track producing electron-hole pairs. The cloud of charge generated around the photo-electron track represents the initial source of charge spread, which drifts under the applied electric field. This charge cloud diffuses laterally when drifting towards electrodes [13]. The range of the photo-electron and the path of the secondary charges depend on the energy of the absorbed photon, so an energy dependence of the charge sharing effects is expected. However an accurate model of charge sharing in the detector is not available and this study is based on experimental data only. Practical effect of charge sharing is that the signal due to a photon is spread over multiple pixels. Inherent energy resolution of the detector is degraded by this effect, leading to a reduced ability to discriminate between two close energies.

The calibration of thresholds represents the first part of this work. At a later stage, the energy resolution of the system has been evaluated. Than the effect of the charge sharing has been studied from a spectroscopic point of view, quantifying it as a function of the X-ray energy of the beam.

5.2 X-ray sources

This work has been carried out in the energy range from 3 keV to 60 keV. Photons in the range from 3 keV to 19 keV have been obtained by X-ray fluorescence emissions of various materials (fig.5.1). In this experimental setup a polychromatic beam produced by an X-ray tube (Hamamtsu L9421-02 micro-focus tube) is strongly collimated on a target which is a thin foil of a solid element (vanadium, iron, copper, molybdenum) or a rubber balloon containing the gaseous element (argon). The target is placed close to the detector as in fig. 5.2.

Fluorescence is excited in the target and characteristic X-ray photons emitted by the material reach the detector. To minimize the amount of scattered photons and maximize the intensity of characteristic X-ray lines, the anode voltage of the tube has been kept just above to the K-edge energy of the target material. The goodness of the spectra of the radiation reaching the detector has been verified using a spectrometric device (Amptek X-123CdTe system).

In the range from 8 keV to 44 keV a synchrotron monochromatic radiation has been used, in particular the SYRMEP beam line at the Elettra-syncrotron laboratory in Trieste (Italy). Energies in this range have been explored in steps of 2 keV. At high fluence, photon-counting detectors have nonlinear response due to dead time effect. In the experiment, the fluence has been kept as low as possible using, as attenuators, various aluminum foils of different thickness. The 59.54 keV photons came from an

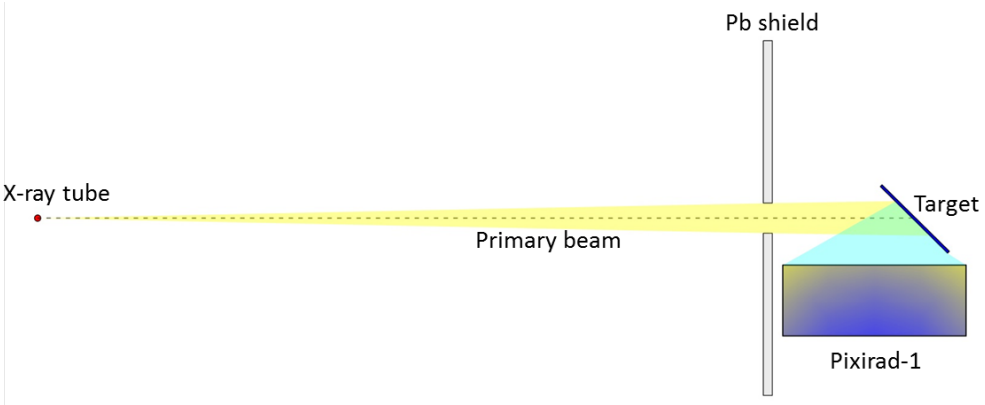

Figure 5.1: Sketch of the set-up of fluorescence measurements

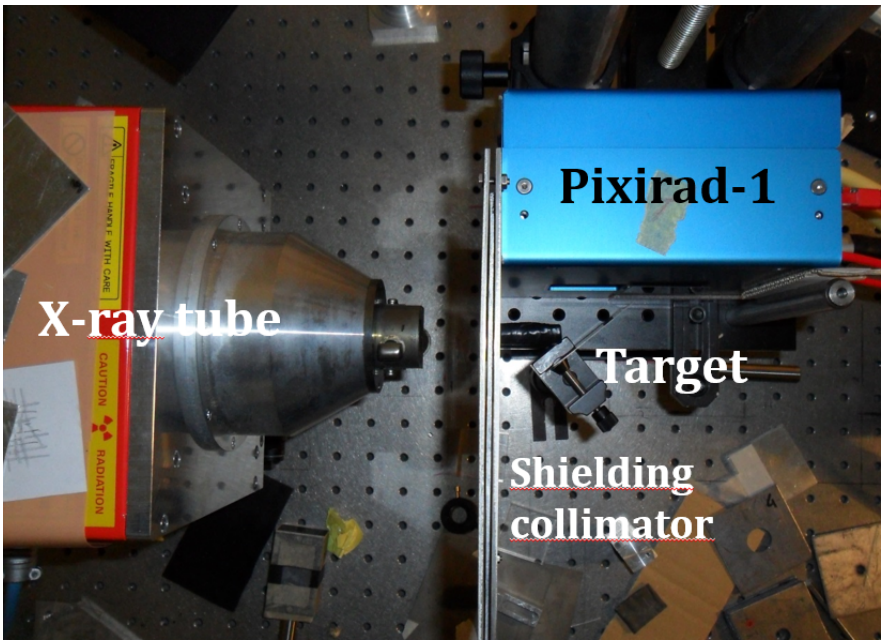

Figure 5.2: The experimental set-up of fluorescence measurements

Am-241 sealed source. The radioactive source was placed as close as possible to the entrance window of the detector.

5.3 Acquisition

Acquired data are arrays of counts generated in each pixel by interactions of photons with the detector during the acquisition time and can be viewed as images. The

detector was operated in one color mode. For each energy, images at different V_{th} values have been taken, performing the so-called thresholds scans. In a scan, the exposure time of a single image is fixed and its choice depends on the fluence of the X-ray beam reaching the detector. The result of a scan is a stack of images containing counts of signals above the corresponding values of V_{th}.

5.4 Raw spectra

Selecting regions in the images of a stack, measuring their mean counts and plotting the obtained values as a function of V_{th} it is possible to draw integral raw spectra (see fig. 5.3a). Differential raw spectra are obtained from previous curves by numerical differentiation. An example of differential raw spectrum of monochromatic X-ray beams of energy lower than 26.7 keV (K-edge of Cadmium) is shown in fig. 5.3b.

Referring to figures 5.3a and 5.3b, the following regions can be identified:

1. *full energy peak that appears (fig. 5.3b) with a distorted (on the left part) Gaussian shape*: the left broadening of the peak is due to the charge sharing phenomenon;

2. *signals corresponding to thresholds lower than the half of the photon energy*: the charge shared in multiple pixels produces multiple counts;

3. *signals corresponding to thresholds higher than the half of the photon energy*: since charge sharing induces the spread of the signal over multiple pixels, in this region an increase in the value of V_{th} corresponds in a loss of counts.

In principle setting up a threshold value corresponding to exactly the half of photon energy (charge sharing between two pixels) one expects to avoid multiple counts and has no losses in counts.

5.5 Calibration

Type 1 regions in differential raw spectra has been selected and fitted with Gaussian functions. Only the points belonging to the right side of the full energy peak are fitted to minimize the broadening effect due to the charge sharing. The values of V_{th} corresponding to the center of the Gaussian functions are represented as function of photon energies (see fig. 5.4). The curve has been fitted with a polynomial function and a relation has been found between V_{th} and the photon energy.

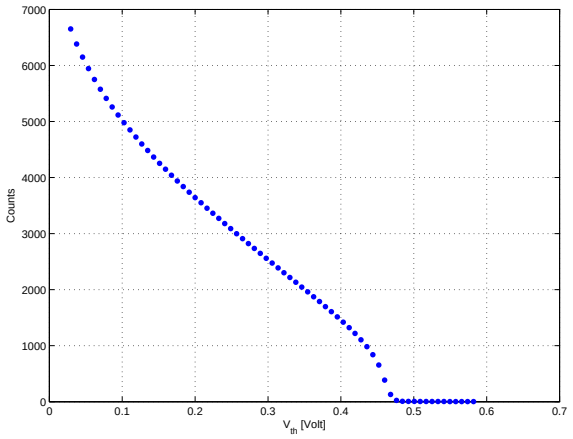

(a) Counts vs V_{th}

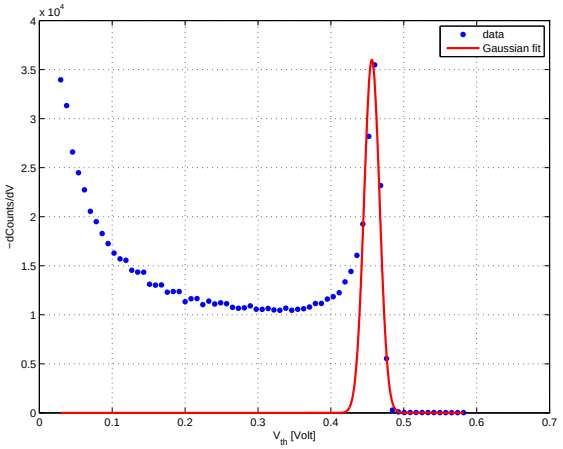

(b) Differential raw spectra

Figure 5.3: Data from a threshold voltage scan

5.6 Energy resolution

After calibration, values of V_{th} in the differential raw spectra can be replaced with corresponding photon energy values. Linearizing the abscissas according the calibration curve, the final spectra have been obtained. On these spectra, using the same fitting described in the section 5.5 the energy resolution has been calculated. For a pixel detector an additional source of the full-peak broadening is related to slight differences in pixel amplifier gain and the residual pixel to pixel DC offsets spread after internal compensation, the energy resolution has been studied for different sizes of the region selected to extract the integral spectrum. In particular, measurements on single pixels

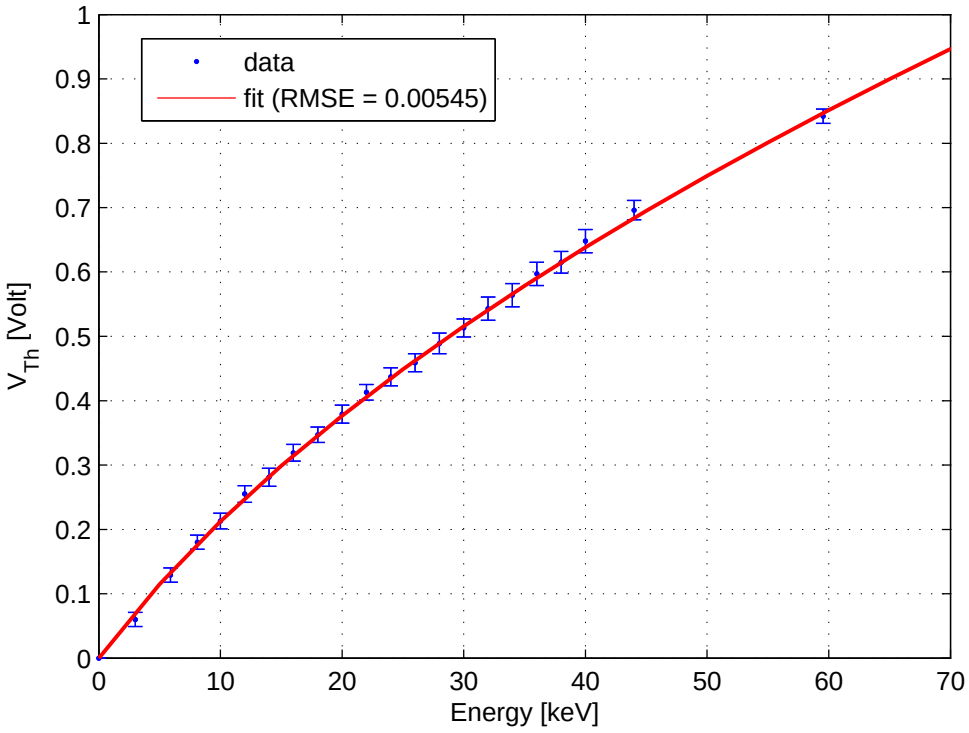

Figure 5.4: Energy calibration curve

has been carried on .

5.7 Charge sharing measurements

Starting from the spectrum shape, it is helpful to estimate the amount of charge sharing, calculating the complement to one of the ratio between the area under the Gaussian fit and the whole area under the curve peak, starting from the half of the energy of photon. This computation has been made after interpolating the data with cubic spline, according the following relation:

$$\text{charge sharing fraction} = 1 - \frac{\int gauss}{\int_{\frac{\overline{E}}{2}}^{E^*} fitdata} \tag{5.1}$$

The sketch in fig. 5.5 shows this simple method, in which $\overline{E}$ is the energy of monochromatic photon, E^* is the spectrum end-point. To avoid that multiple counts affect the

measurements, the integral lower bound of fit-data must be equal to $\frac{\overline{E}}{2}$.

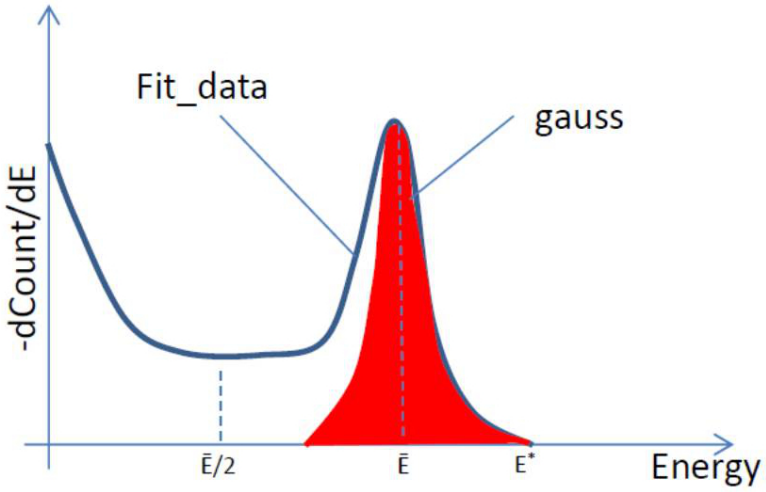

Figure 5.5: Sketch of a spectrum of monochromatic photon beam of energy $\overline{E}$: the blue line represents data interpolation with cubic splines, the red area is the Gaussian integral of signal.

5.8 Measurements results

The calibration curve of the detector is shown in fig. 5.4. It shows the absence of saturation effects in the range up to 60 keV, thus making the device effective for spectroscopic studies only in this range. The nonlinear behavior, mostly occurring at energy greater than 15 keV, is consistent with the original design of the ASIC [15].

In fig. 5.6 some differential spectra acquired with different photon sources are shown. These spectra have been obtained selecting regions composed of 1000 pixels. The good energy resolution of the system is noticeable even for very low energy photon, as that one coming from 2.96 keV argon line fluorescence (fig. 5.6a), but residual background of the primary beam is even present. The system is able to discriminate the K_α and K_β fluorescence lines of molybdenum at 17.5 keV and 19.6 keV (fig. 5.6b). The fig. 5.6c shows the spectrum of 20 keV synchrotron X-ray beam, third-order harmonic contamination of the source and perhaps residual pileup effect causing the tail above the full energy peak. The fig. 5.6d shows the spectrum of Am-241 radioactive source.

The corresponding energy resolution results are summarized in tab. 5.1. Better spectra are expected if data come from a single pixel. The limiting factor in a single pixel analysis is the poorer statistics bringing noisier data (the differentiation of the integral spectrum propagates that noise).

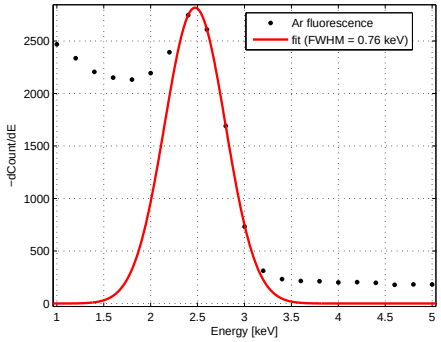

(a) Argon fluorescence line spectrum

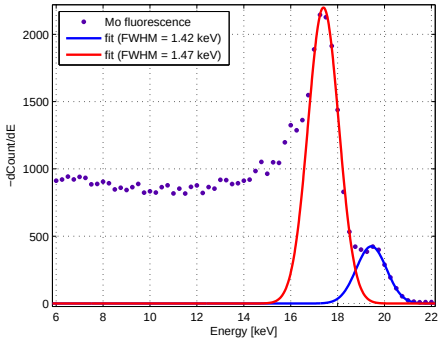

(b) K_α and K_β Molybdenum fluorescence lines

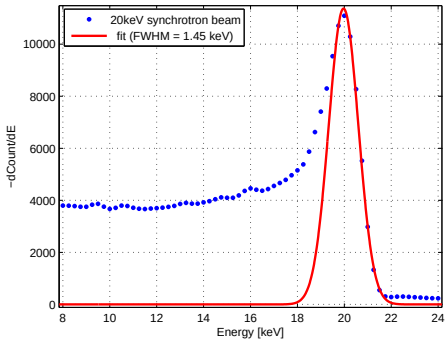

(c) 20 keV synchrotron light monochromatic spectrum

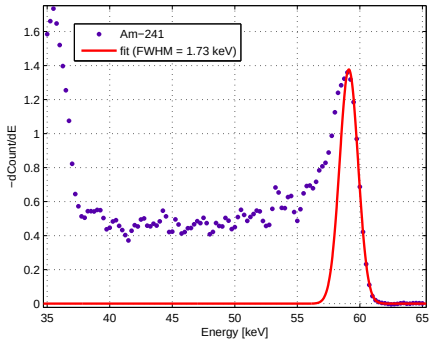

(d) Am-241 spectrum

Figure 5.6: Some spectra obtained with different photon sources

However, some single pixel spectra have been obtained (see fig. 5.7) proving the expected improvement of the energy resolution. In the simplest model, the energy resolution of the detector is influenced only by electronic and statistical noise [2]:

$$(FWHM)^2_{overall} = (FWHM)^2_{el} + (FWHM)^2_{stat} \tag{5.2}$$

The theoretical energy resolution based on eq. 5.2 for a 16 keV photon, considering that the Equivalent Noise Charge of the ASIC is 50 electrons rms and assuming a Fano factor for CdTe of 0.15 [7], is 574 eV. The spectrum in fig. 5.7 shows the measured FWHM (710 eV) at the same energy. This value can be considered close to the theoretical one keeping in mind that eq. 5.2 does not take into account the worsening influence of coupling capacitance between the CdTe sensor and the ASIC. The broadening effect on energy resolution of cluster of pixels (1310 eV at 16 keV) compared to the single pixel one (710 eV at 16 keV) is due to small differences of the amplifier

Table 5.1: Energy resolution on a cluster of 1000 pixels

Energy [keV]	FWHM [keV]	Resolution %
2.96	0.76	25.8
4.95	0.85	17.1
8.1	0.88	10.8
10	0.92	9.2
12	1.06	8.8
14	1.20	8.6
16	1.31	8.2
18	1.48	8.2
22	1.38	6.3
38	1.60	4.2
59.54	1.73	2.9

gain (of the order of 2% rms) and residual offset variation from pixel to pixel, which are not completely corrected by the self-calibration. In fig. 5.8 it is shown the fraction of charge shared events, calculated according the eq. 5.1, for monochromatic photon beams in the energy range from 3 keV to 26 keV, below the energy of the Cadmium K-edge. The plot suggests that up to 10 keV the fraction of charge sharing events increase almost linearly and after a knee it reaches a value of about 70%. Further studies are ongoing to better understand this behavior.

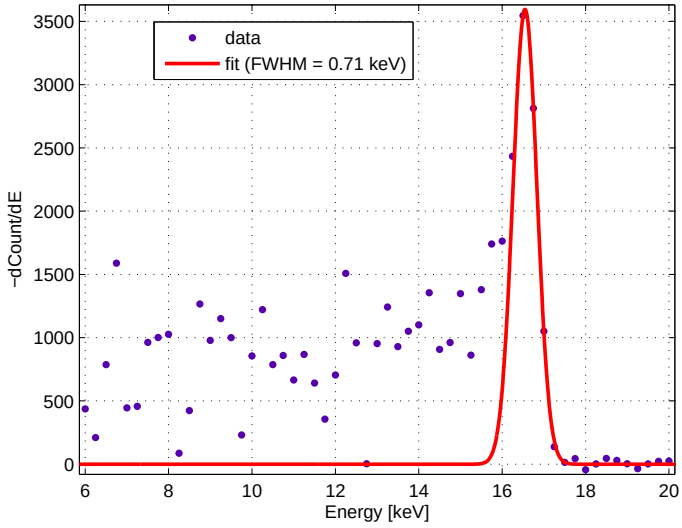

Figure 5.7: Single pixel energy resolution 16 keV

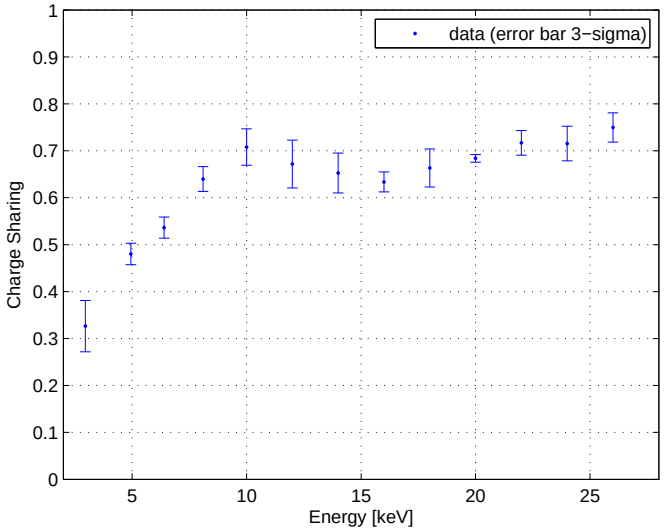

Figure 5.8: Fraction of charge shared events measured at different energy

Chapter 6

Imaging characterization of Pixirad-1

The aim of this chapter is the characterization of the imaging performance of the Pixirad-1 detector system with monochromatic synchrotron radiation at different energies. The linearity of the system has been investigated varying the impinging photon flux up to paralyzation. The ratio between detector counts and number of impinging photons, as a function of energy and discriminator thresholds, has been measured. The pixel noise has been evaluated and the result compared with the theoretical Poisson model. Eventually, the spatial resolution has been evaluated by measuring the line-spread function at different energies and discriminator thresholds [20].

6.1 X-ray source

The data have been acquired at the SYRMEP (SYnchrotron Radiation for Medical Physics) beamline (fig. 6.1) at Elettra. The machine ran at 2 GeV in top-up mode with multi-bunch filling pattern. The radiation source is one of the bending magnets of the storage ring; a double-crystal Si(111) monochromator provides a beam energy in the range from 8.5 to 44 keV, with energy resolution $\Delta E/E = 2 \cdot 10^{-3}$. Several tungsten slit systems are used to define the beam shape in order to be completely included in the detector surface. The beam cross-section at the detector is 29 mm (horizontal) x 5 mm (vertical, Gaussian-like shape). The flux can be adjusted by means of a stack of aluminum sheets of different thickness used as attenuators and it can be measured with an ionization chamber used as a beam monitor system. Since the ionization chamber is calibrated, the mean number (intensity) and mean number per unit time (flux) of photons per pixel can be calculated for each experimental condition. Monochromators based on silicon crystals can generate third harmonics in the output beams. When selecting the energy, it has been used the crystal detuning procedure to reduce the harmonic contamination. Moreover, for each working point, it has been verified that at a threshold slightly above the selected energy, the detector registered no counts.

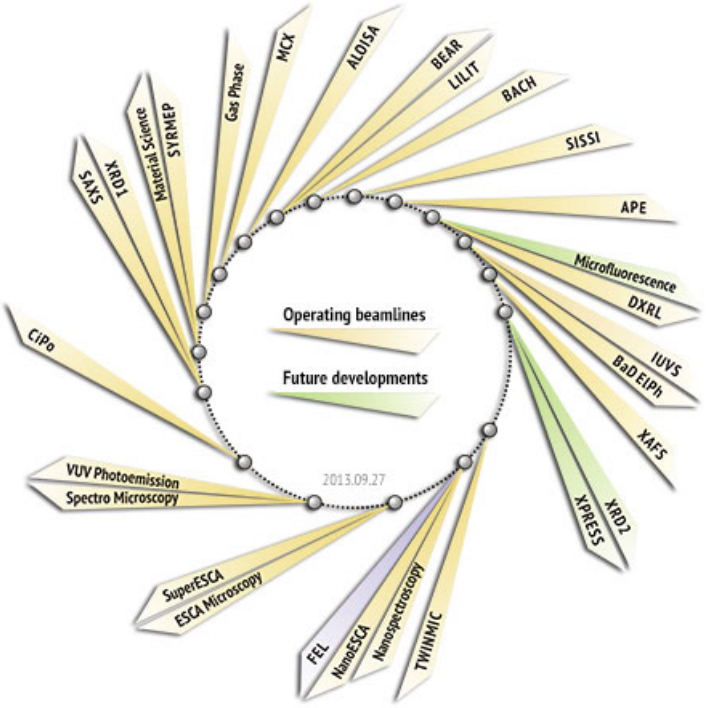

(a) Elettra.

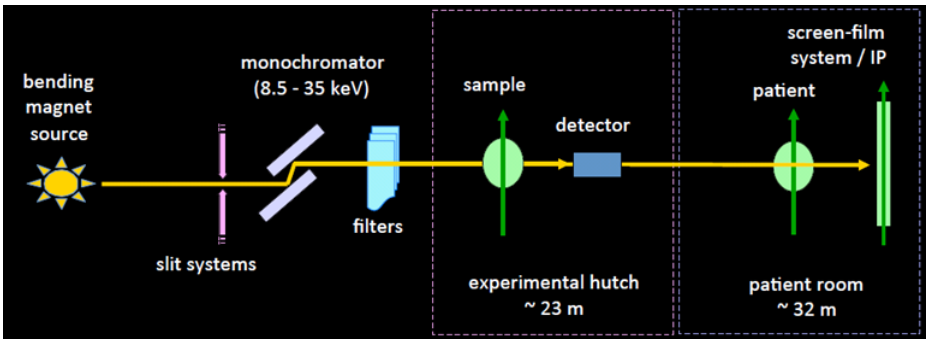

(b) SYRMEP.

Figure 6.1: SYRMEP beam line at Elettra synchrotron (Trieste)

6.2 Linearity

Linearity measurements have been performed at different energies and discriminator threshold values (working points). For two energies (20 keV and 30 keV) it was possible to reach a photon flux high enough to paralyze the detector. Since dead time is related mainly to the temporal overlap of the signals higher than the discriminator threshold, it is expected to observe some dependence on the photon energy and on

the threshold value. For each working point it was varied the mean photon flux by choosing the appropriate attenuators. Fixing an acquisition time of 10 ms, it has been recorded sets of 10 images of the beam (to improve the statistics) and the beam monitor readings. Since the beam has a vertical inhomogeneous shape, the local photon flux varies along the vertical direction (fig. 6.2). This allows extracting from a single image, the mean counts of the pixels in different rows, corresponding to different fluxes. For each working point, the shape of the beam has been obtained from the image at the lowest mean flux, assuming that the whole detector is working in linear regime. Fig. 6.2 shows two images of the beam at low and high mean flux and their vertical profiles. Low-flux image allows defining the actual beam profile that appears distorted in the high-flux one.

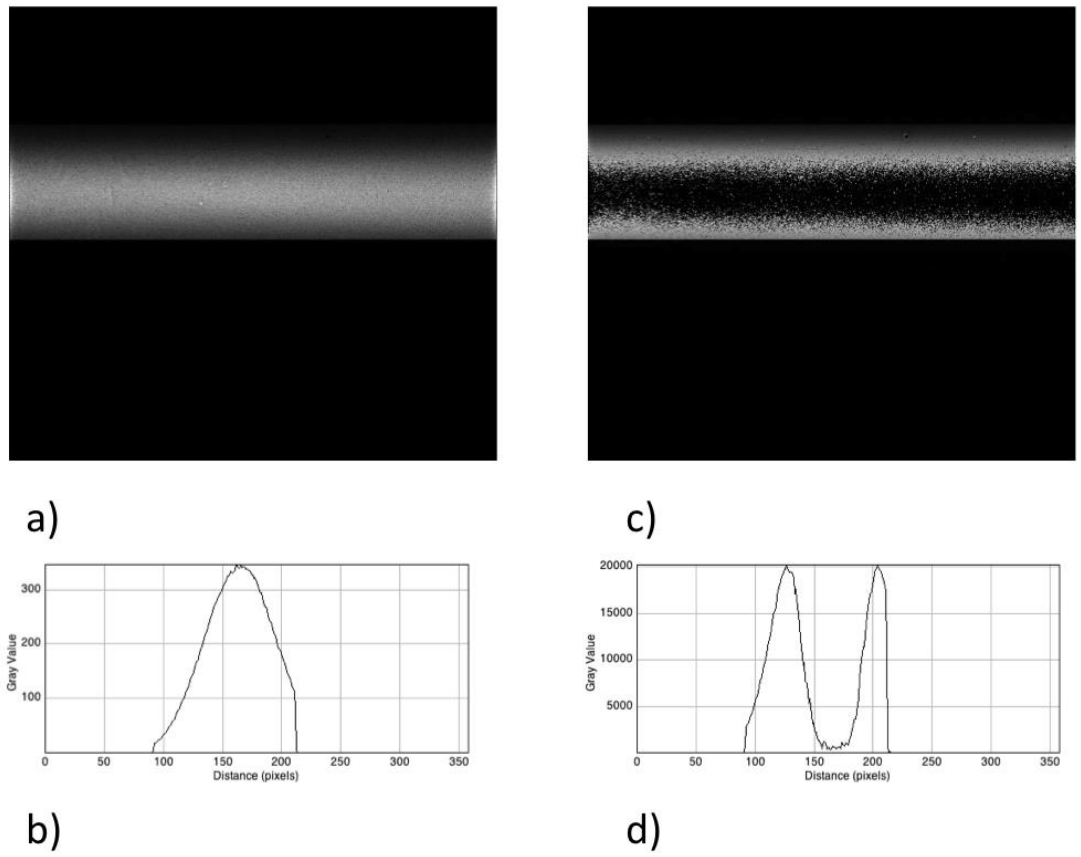

Figure 6.2: The image of the beam with attenuators (a) allows extracting the beam profile along the vertical direction (b). In the image of the beam without attenuators (c), pixels under higher flux get paralyzed and the profile (d) is strongly distorted.

In the analysis of data it is called *input events* the signals, coming out from the preamplifiers and selected by the discriminators, that should be counted if the system

were in linear regime and *counts* the signals actually recorded. The number of input events per photon interacting in the sensor depends actually on the discriminator threshold value. For example, setting up a threshold value above the energy of the photons, the rate of input events is always zero. Moreover, setting up a threshold value below half the energy of the photons, multiple input events per photon are allowed due to charge share. At sufficiently low fluxes no loss of counts occurs, every input event is counted and the counts rate is equal to the input events rate. At high fluxes counts are lost, the system becomes nonlinear and the counts rate is lower than the input events rate. Input events rates at high fluxes have been calculated by re-scaling the input events rates at low fluxes for the beam monitor readings at high fluxes. The results of the analysis of the linearity of the system have been summarized as plots of counts per pixel per second as function of input events per pixel per second.

Fig. 6.3 shows the counts per pixel per second as a function of the input events per pixel per second for two different energies and different thresholds values. As the energy of the photons and the threshold vary, the system remains linear up to $2 \cdot 10^5$ counts per pixel per second. The loss of linearity above this value depends on both the energy and threshold.

Let's define C_{max} the maximum achievable number of counts per pixel per second and I_{max} the corresponding input events per pixel per second. Those values define the range in which the system can, in principle, be linearized. Increasing the energy of the photons, C_{max} and I_{max} decrease. Referring to the fig. 6.3 a and c (20 keV and 30 keV at low thresholds), C_{max} varies from about $4 \cdot 10^5$ to $3.5 \cdot 10^5$ counts per pixel per second. For the same working points, I_{max} decreases from about $7 \cdot 10^5$ to $5.5 \cdot 10^5$ input events per pixel per second. This behavior can be explained in terms of the amplitude of the signals coming out from the charge preamplifiers: higher energy photons produce, on average, higher and temporally longer signals that lead to paralyzation at lower fluxes. Moreover, fixing the photons energy, an increase of the discriminator threshold selects higher and temporally longer signals coming from the preamplifier, with consequent decreasing of C_{max} and I_{max} that limits the range of the linearizability. Finally, the slope of the curve depends also on the energy of the photons and on the threshold value, making the linearization a high specific task.

6.3 Energy response

Energy response measurements have been performed to relate the counts with the number of impinging photons as a function of energy and discriminator threshold. The photon energy was varied in the range 16 - 38 keV and, for each energy value E, a set of images of the beam was taken. The flux was set in order to keep the count rate inside the linear region. The set is obtained by fixing the single image exposure time to 100 ms, scanning the threshold values ($2keV < th < E + 2keV$) with steps of 1 keV,

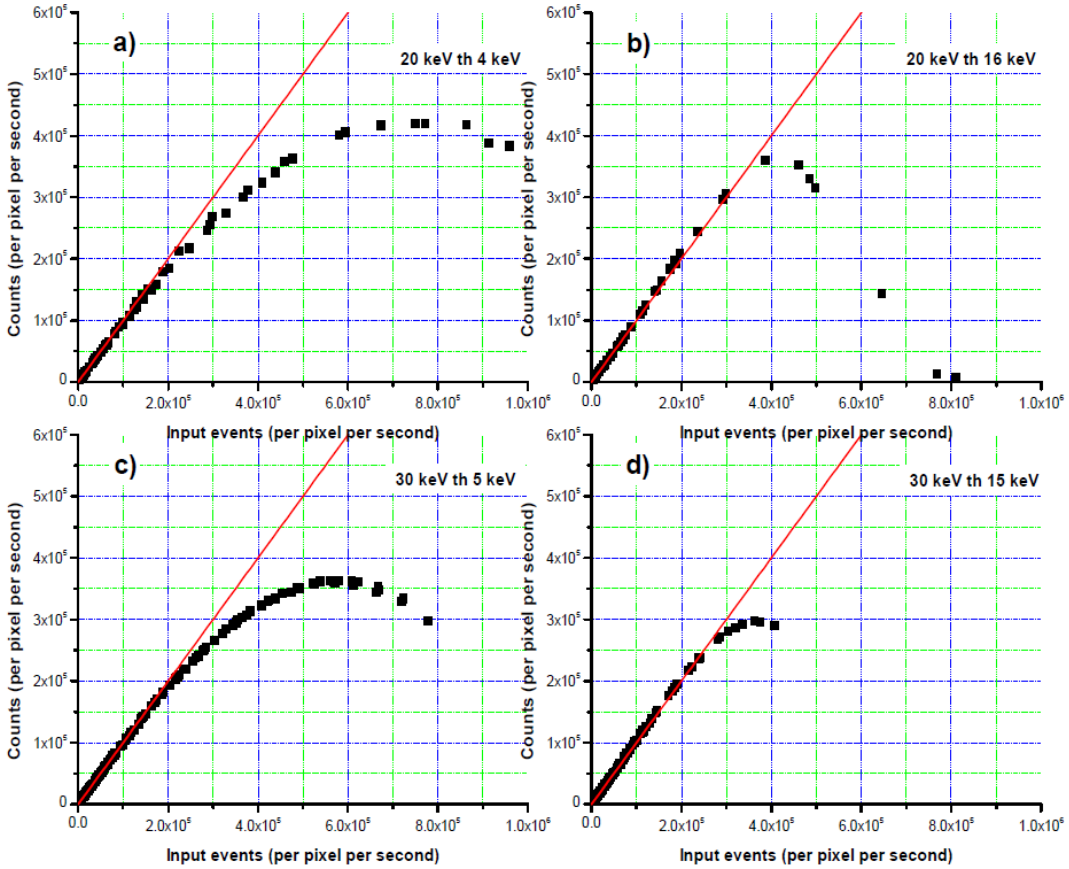

Figure 6.3: Linearity curves for different energies and thresholds values.

and recording 10 images per step to improve the statistics. For each image, it has been measured the mean counts per pixel in the region hit by the photons and compared it to the intensity measured by the beam monitor system. The number of counts of each pixel was then compared with the expected number of impinging photons on the pixel, calculated by taking into account beam energy and size, exposure on the monitor ionization chamber, detector acquisition time, distance between the ionization chamber and the detector and the corresponding air attenuation.

The *Energy Response* (ER) is the ratio between the experimental counts and the number of impinging photons. Since charge sharing is present, the ER depends on the threshold used in the acquisition: if $th < E/2$, multiple counts are allowed and ER can be greater than one; if $th > E/2$ there is a loss of counts and ER<1. In principle, setting up a threshold exactly equal to half the energy of the photons ($th = E/2$), ER corresponds to the efficiency. This dependency is investigated by repeating the ER measurement at different threshold values.

The ER as a function of energy is reported in fig. 6.4. The results are shown for

three values of the discriminator threshold. The threshold is reported here as a fraction of the beam energy (i.e. for 20 keV, th=0.5 means a threshold value of 10 keV). As expected, for a threshold value of 0.5, the ER is almost 1 below the K-edge energy of Cadmium (26.7 keV). Above this energy, a fluorescence photon can be produced that can either escape the material or be reabsorbed by the detector. However, in the latter case, the charge generated by this photon can be split in two (or more) pixels in a way that, for each pixel, the charge is below the threshold. So the photon is lost. This explains the drop in ER. A similar trend can be observed close to the Te K-edge (31.8 keV). For lower thresholds the ER at low energies is greater than one, because for some photons the charge, shared between two pixels, is counted twice.

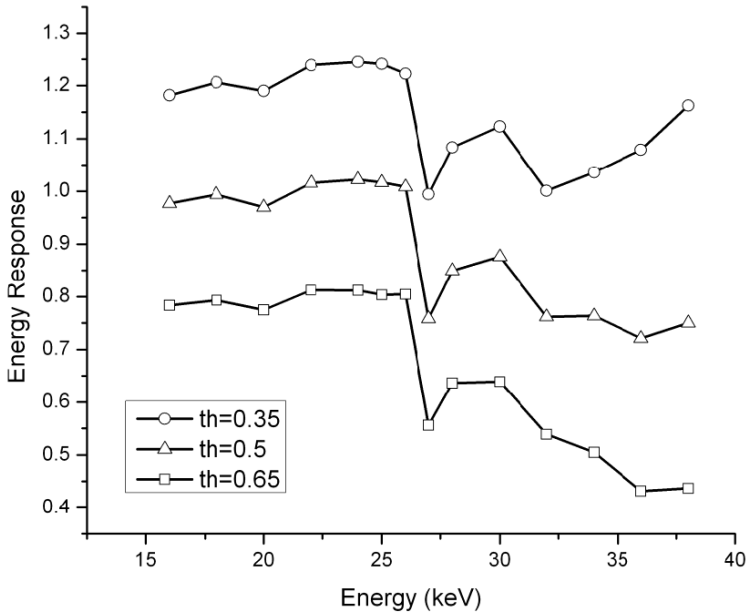

Figure 6.4: ER function: the experimental data are presented for three different thresholds: 35, 50 and 65% of the beam energy.

6.4 Energy and intensity dependence of image noise

Since the detector is a photon counter, the counts in each pixel follow a Poisson distribution: the dependence of image noise on X-ray energy and intensity is modeled by using this simple assumption. If σ is the standard deviation of counts and I the average counts in a given region, it has been suppose:

$$\sigma = \sqrt{I} \tag{6.1}$$

To test this model, it has been analyzed the data acquired according the method explained in the previous section. For each energy, in order to expand the range of intensities under investigation, it has been also used different filtrations. Since the beam presented spatial non-uniformities that could affect the evaluation of fluctuations, 9 images were averaged and used as a flat field, in order to equalize the 10th image. It has been divided furthermore each image in small area regions (5 x 10 pixels) calculating the mean intensity and the standard deviation in these regions. Finally, a scatter plot of these standard deviations vs. mean intensities has been produced. The experimental data are also compared with the theoretical curve.

In fig. 6.5 the standard deviation is plotted as a function of the mean counts, for four energies. The threshold value used is 0.5 E. The theoretical Poisson behavior (solid line) is also reported in fig. 6.5 and it is in very good agreement with the experimental data. The few points not following the Poisson distribution are due to noisy pixels. Results are similar for all the energies under investigation.

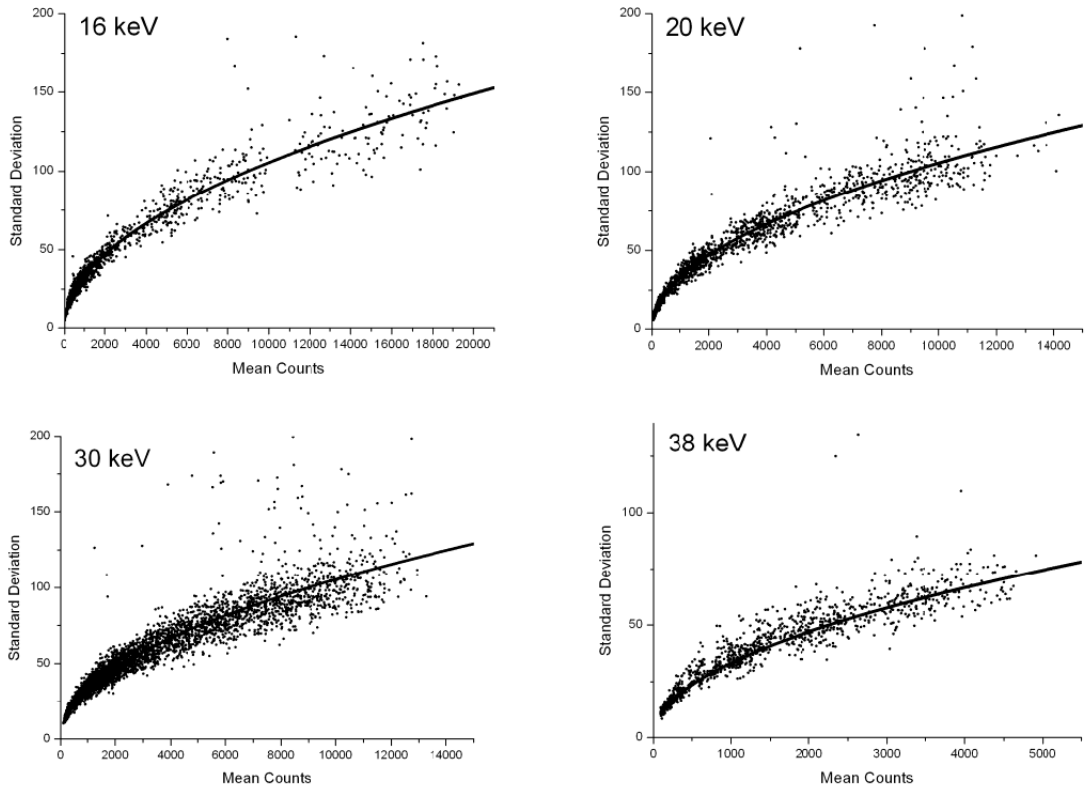

Figure 6.5: Standard deviation as a function of average count for four monochromatic energies. The threshold value is 0.5 E. The solid line is the theoretical Poisson behavior.

6.5 Spatial resolution

Spatial resolution has been evaluated, in the range 15 - 40 keV, in terms of *Line Spread Functions* (LSFs) using a method similar to the one proposed in the paragraph 2.3.1 (Fujita method). A tungsten sheet, 0.5 mm thick, with a sharp border has been used to acquire images of an edge. The sheet was placed slightly slanted with respect to the pixels rows or columns in order to obtain the over-sampled *Edge Spread Functions* (ESFs). Images were later processed and the LSFs calculated. Since Pixirad-1 detector with PIXIE II ASIC has hexagonal pixels arranged in a honeycomb matrix, some care must be put in both acquiring and analyzing data. First of all, the aper-

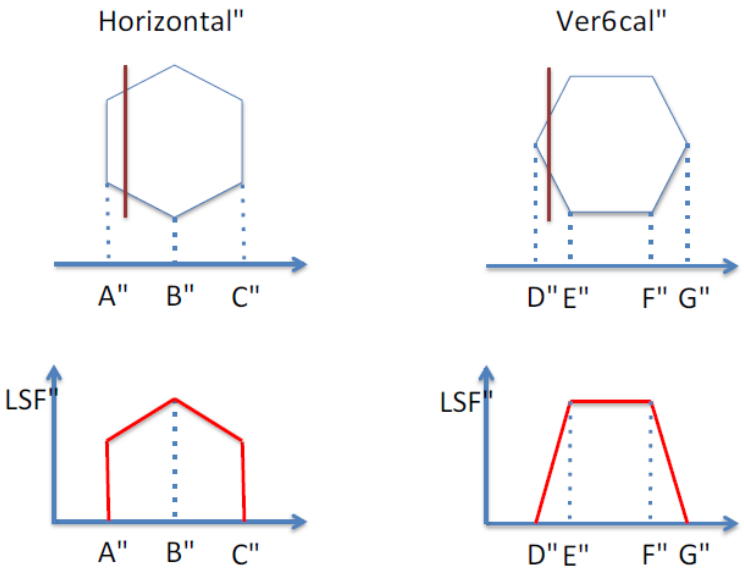

Figure 6.6: Ideal LSFs for a pixel with hexagonal aperture.

ture of a single pixel is asymmetrical: its maximum width along the vertical direction, is 69.3 microns, while the maximum width, along the horizontal direction, is 60 microns. Using a purely geometric model to describe the spread due to the pixel aperture, LSFs obtained scanning the line along horizontal and vertical directions differ in shape (fig. 6.6). Consequently it has been evaluated both horizontal and vertical LSFs. Moreover, sampling points (centers of the pixels) lie on straight lines along the horizontal direction while, along the vertical direction, odd and even rows are shifted by half a pitch. To correctly obtain oversampled ESFs, each image has been split in two sub images made up with only odd and even rows and analyze them independently. To obtain the vertical LSFs, it has been started from the image of the slanted edge, equalized for flat field, extracting profiles along columns (fig. 6.7 b and c). Profiles from different columns are combined to produce a high statistics oversampled ESFs. The ESF is then

differentiated obtaining the LSF (fig. 6.7 d). A similar procedure is used to obtain the horizontal LSFs. Images were acquired in linear regime. Since it is expected that the most important factor limiting the spatial resolution is the charge sharing, the study of LSF has been made as a function of the energy of photons and the discriminator threshold value.

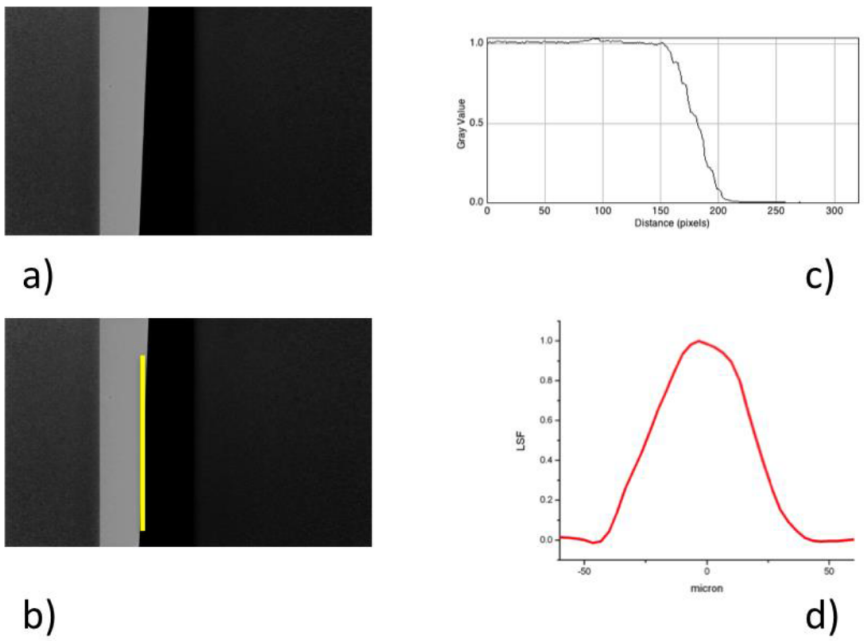

Figure 6.7: Vertical LSF. a) Image of the slanted edge, equalized for flat field. b) Selection along a column where the profile (c) is extracted. d) LSF obtained from a high statistic ESF.

The fig. 6.8 shows the horizontal and vertical LSF at 25 keV with a discriminator threshold of 16 keV. No multiple counts due to charge sharing are expected in this set up. Vertical LSF is slightly wider (45 ± 5 microns FWHM) than horizontal one (38 ± 5 microns FWHM). This is compatible with the expected differences due to the aperture functions.

Fig. 6.9 shows a set of vertical LSFs corresponding to different energies. For each energy, the threshold is set close to $E/2$, in order to avoid multiple counts. LSFs have similar width, ranging from 41 ± 5 microns FWHM at 20 keV to 49 ± 5 microns FWHM at 35 keV. At higher energy ($\geq$30 keV) it has observed a rise in the tails, due to fluorescence photons that interact with the detector far away from the creation point.

Fig. 6.10 shows a set of vertical LSFs obtained at 15 keV with different discriminators threshold values. At thresholds $\leq$7keV multiple counts are possible, allowing a

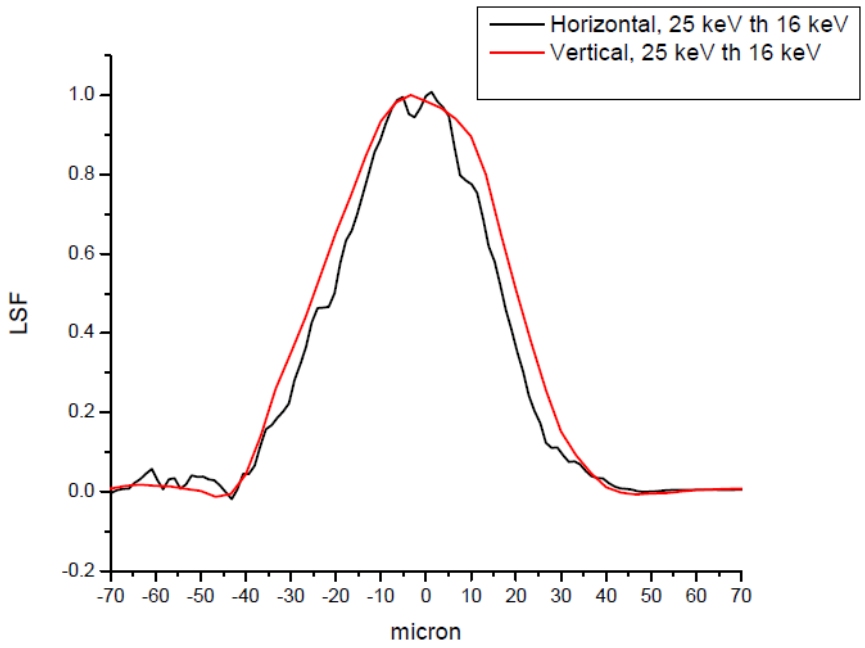

Figure 6.8: Horizontal and vertical LSF.

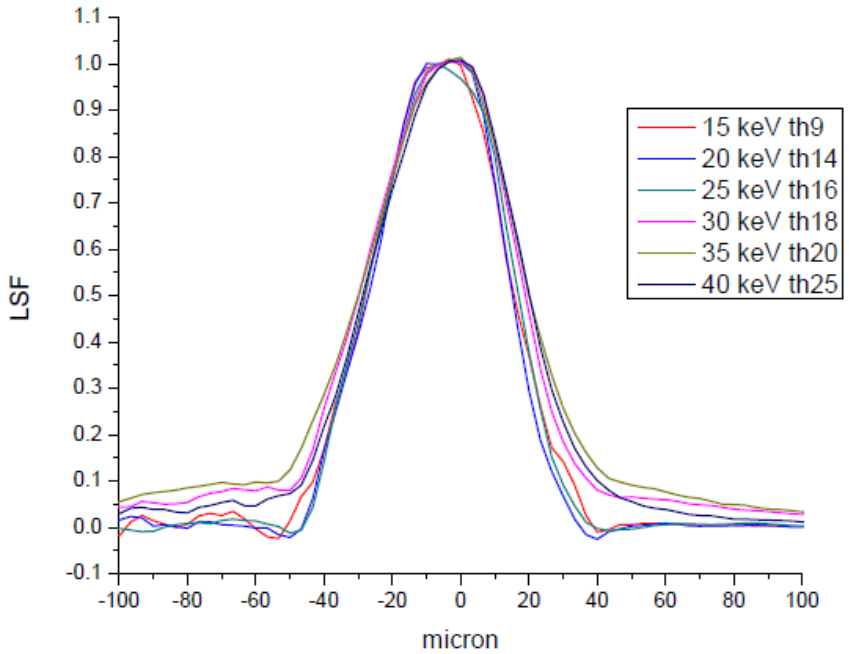

Figure 6.9: Vertical LSFs at different energies.

spread in the LSF width. This effect increases when lowering the thresholds. On the other hand, higher thresholds select the events with less charge sharing; these events, that are due to photons interacting in the center of the pixel, cause a shrinkage of the LSF. The width ranges here from 61 ± 5 microns FWHM at 3 keV threshold to 34 ± 5 microns at 13 keV threshold.

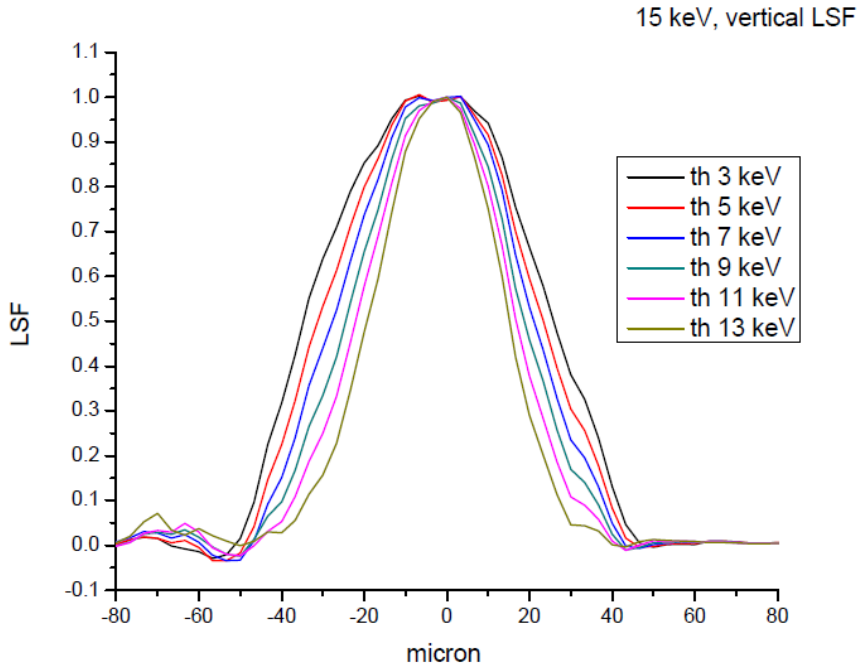

Figure 6.10: Vertical LSFs at same energy and different threshold values.

This behavior can be observed at different energies. Fig. 6.11 shows the dependence of the LSF width from the discriminator threshold expressed as a fraction of the photon energy. The relationship appears almost linear.

The system is always reasonably linear up to $2 \cdot 10^5$ $counts\,mm^{-2}\,s^{-1}$ or rather about $6.5 \cdot 10^7$ $counts\,mm^{-2}\,s^{-1}$ (since the pixel density is 323 $pixels\,mm^{-2}$). In principle, up to the paralyzation, the system can be linearized. However, since the maximum rate of counts before the paralyzation as well as the dependence of the counts from the input photon rate depends on both the energy and discriminator threshold, this task is highly specific, especially with polychromatic sources. The energy response (for the energies under investigation) is almost one for thresholds close to one half of the energy of the beam, up to the Cadmium K-edge. Above the K-edge, there is a significant drop of the response, due to fluorescence photons. This effect is particularly severe for the highest thresholds. The noise on the pixel matches perfectly the expected Poisson behavior for all the energies under investigation, even above Cd K-edge. Since the line spread function depends mainly on the threshold value, expressed as a fraction of the

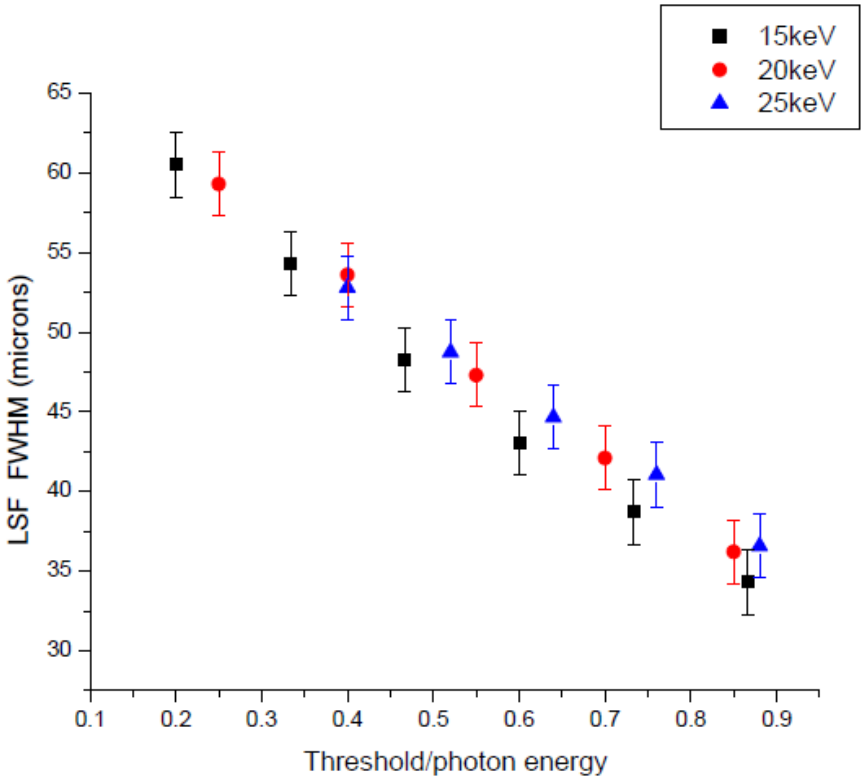

Figure 6.11: LSFs width as a function of threshold for various energies.

energy of the photons, it is possible to predict it at different energies and thresholds. The knowledge of the quantities, studied in this chapter for monochromatic energies, allows to easily simulate the behavior of the detector also in the case of polychromatic sources.

Chapter 7

PIXIE III: the third ASIC generation

In this chapter are showed some last measurements with PIXIE III: the third generation of very large area (32 x 25 mm^2) pixel ASICs developed by Pixirad Imaging Counters s.r.l. to be used in combination with suitable X-ray sensor materials (Silicon, CdTe, GaAs) in hybrid assemblies using flip-chip bonding. A Pixirad unit module based on PIXIE III shows several advances compared to what has been available up to now. It has a very broad energy range (from 2 to 100 keV before full pulse saturation), high speed (100 ns peaking time), high frame rate (larger than 500 frame/s), dead-time-free operation, good energy resolution (around 2 keV at 20 keV), high photo-peak fraction and sharp spectral separation between the color images [21].

7.1 Introduction

Spectroscopic imaging is the new frontier in X-ray and γ-ray imaging applications. Indeed, spectral information adds a new, powerful dimension to the image. High speed photon-counting with pixel detectors is the natural technology choice to try to implement this new modality. However, adding sharp color sensitivity to a very finely segmented pixel sensor is highly demanding in terms of complexity and transistor density of its read-out electronics which has to cope with the *charge sharing* effect. The sharing is due to the finite size of the charge cloud and the unavoidable diffusion process occurring during its transport from the conversion point to the collecting pixel anode [22]. To solve the problem of charge sharing a new generation of very large area (32 x 25 mm^2) pixel ASICs, PIXIE III, has been developed by Pixirad Imaging Counters srl. Pixirad detectors are based on the hybrid assembly of a CMOS VLSI ASIC to suitable X-ray sensor materials (Silicon, CdTe, GaAs) via the flip-chip bonding technique. PIXIE III can be configured in several counting modalities. In *Pixel Summing Mode* (PSM) it is possible to recover the charge (energy) shared between one pixel and its neighbors (mostly one) and get a sharp X-ray spectral imaging.

A PIXIE III based on Pixirad unit shows several advances compared to what has been available up to now. It has a very broad energy range (from 2 to 100 keV before full pulse saturation), high speed (100 ns peaking time), high frame rate (larger than 500 fps), dead-time-free operation, good energy resolution (around 2 keV at 20 keV), high photo-peak fraction and sharp spectral separation between the color images.

7.2 The large area photon-counting ASIC, PIXIE III

The chip is fabricated in 0.16 μm CMOS technology and it is organized as a matrix of 512 x 402 square pixels at 62 μm pitch. Each pixel incorporates an octagonal electrode (top layer of metal) connected to a charge ensitive shaping amplifier feeding two discriminators and two 15-bit counter/registers allowing to collect two color images in a single exposure. The events are counted into a first counter (counter#0) if their energy falls inside the window defined by a lower (V_{th0}) and an upper threshold (V_{th1}), and counted into a second counter (counter#1) when their energy is higher than V_{th1}.

Table 7.1: PIXIE III electrical characteristics

Equivalent noise charge	50 electrons rms
Linear range	> 12000 electrons
Saturation level	> 18000 electrons
Residual offset after auto-calibration	$\pm$30 electrons
Shaped pulse duration (at the base)	450 ns (adjustable)

To reduce unavoidable DC offset variations from pixel to pixel at the discriminators input, a self-calibration circuit is implemented in each pixel. In this way global threshold levels can be applied to the whole matrix with the noise fluctuations as the main limiting factor to the device sensitivity. During the data acquisition, the shift registers, in conjunction with a proper XOR feedback, are used in pseudo-random generator mode, clocked by the trigger coming from their respective discriminators. After initialization, the number of events or clock periods recorded is uniquely linked to the register contents, with a maximum of 2^{15} counts per counter. In read-out mode, the registers of each column of pixels are serialized and their content pushed out of the circuit under the control of an external clock signal. In Table 7.1 are listed the main features of PIXIE III.

The chip can be configured in different operation modes, the most important being:

1. **Pixel Mode** (PM): in this modality each pixel counts independently from the others. The pixel works in windowed counting mode and each counter can be read-out in less than 1 ms, allowing for very high frame rates. PM is the modality

showing the highest count rate capability (higher than 1 MHz input rate per pixel) but it could suffer for some multiple counts effect when working at very low thresholds with polychromatic beams. The sharpness of the color separation is limited by the tail of the pixel charge collection efficiency due to charge leak to neighbor pixels because of diffusion.

2. **Neighbor Pixel Inhibit mode** (NPI): in this modality only one counter per event is allowed to count. This is accomplished by exploiting the duration (Time-Over-Threshold) of the discriminator output pulse. In case an event spreads over several pixels, the hit is allocated to the pixel receiving the highest fraction of the total charge. This modality has the highest position resolution and the lowest possible noise, but the problem of the sharpness of the color separation is not yet completely solved.

3. **Pixel Summing Mode** (PSM): in PSM mode the signals of 4 neighbor pixels are summed together to correctly evaluate the total energy of any event involving up to 4 pixels. Because the sum is performed in each pixel, i.e. at the same pitch of 62 μm in both X&Y directions, when used in combination with NPI the PSM ensures that both the spatial accuracy and energy resolution are finally preserved. The unavoidable trade-off is an increase of a factor 2 in the pixel noise and a factor 4 in the pulse pile-up probability. For this reason special attention has been paid to reduce the input amplifier shaping time to less 450 ns (total duration of the pulse at the base) and the noise of the FE amplifiers.

To obtain two sharp *color* images in a single exposure, a third discriminator and a sum amplifier have been added in each pixel. The summing amplifier collects the 4 signal currents which are dispatched by the front-end amplifier (FE) of the pixel itself and by the FEs of 3 neighbor pixels (at East, South and South-East) and converts the sum back into a voltage. The latter is then discriminated against the windowed energy thresholds to assign the hit to a unique color pixel counter. The additional discriminator is used to resolve the ambiguity, which occurs when only one pixel collects the full charge.

A Monte Carlo detailed model has been developed to simulate the different modes of operation of PIXIE III; in particular to check how efficiently the Pixel Summing Mode can recover the charge (energy) shared between pixels, respect to the standard Pixel Mode. The MC results for 26 keV X-ray photons and a CdTe sensor of 750 μm thickness are shown in fig. 7.1 where the blue line refers to photons with energy between 5 and 13 keV and the red one to photon with energy greater than 13 keV. The energy and spatial distributions obtained with the PSM show clearly how this mode allows preserving both energy resolution and spatial accuracy.

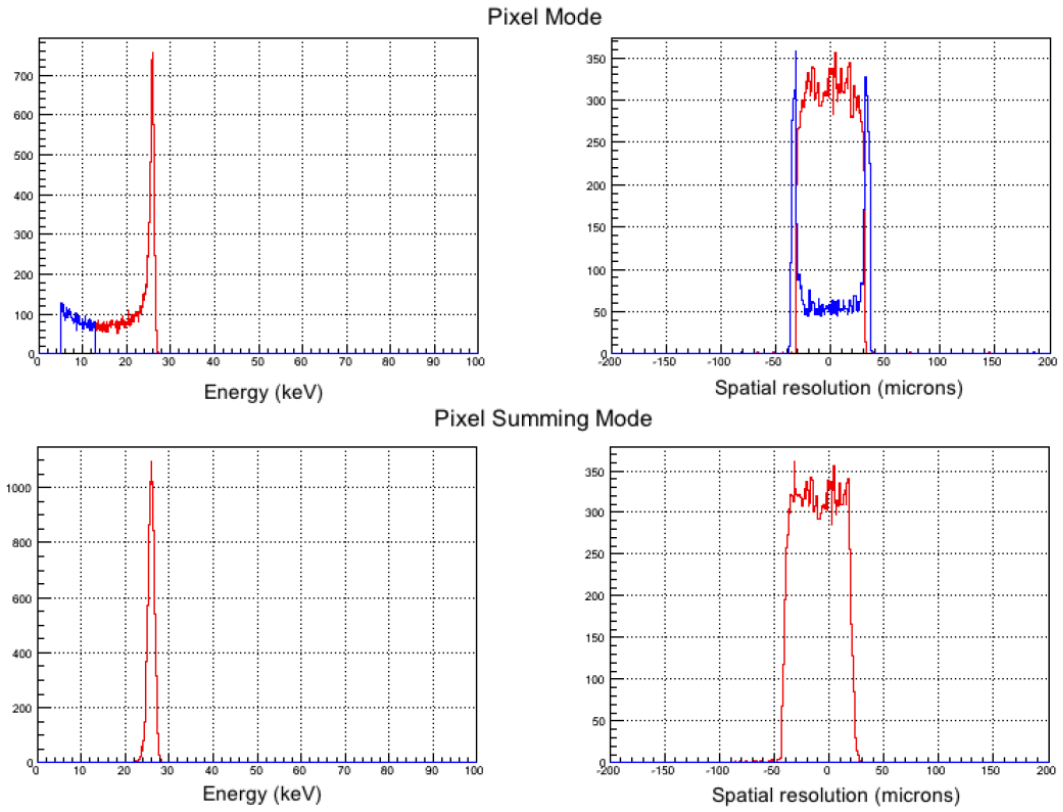

Figure 7.1: Monte Carlo simulation of PIXIE III Pixel Mode functionality (top) and Pixel Summing Mode (bottom). The simulation has been performed with 26 keV photons and 750 μm CdTe. In the figure, the label *Spatial resolution* refers to the difference between true and reconstructed MC points.

7.3 Results in test bench set-up

Threshold scans with charge injection have been performed to study the basic characteristics of PIXIE III. Fig. 7.2 shows the normalized pixel counts as a function of the threshold for the single pixel (left panel) and for all pixels (right panel) in a CdTe-PIXIE III detector. The difference between 16% and 84% in the cumulative distribution function (the sigmoids in fig. 7.2) gives an estimation of the noise. The measured single pixel noise, corresponding to the amplifier noise, is 0.85 keV FWHM, while the overall noise (averaged over all the pixels) is 1.61 keV FWHM (CdTe equivalent). The latter is the sum squared of different contributions:

$$(FWHM)^2_{tot} = (FWHM)^2_{amp\ noise} + (FWHM)^2_{offset\ disp} + (FWHM)^2_{gain\ disp} \quad (7.1)$$

The equivalent noise for Silicon can be derived from the single pixel noise for CdTe, by scaling with the ratio of the average energy per hole-electron pair (4.43 eV for CdTe, 3.62 eV for Si). The Si equivalent single pixel noise is (FWHM) = 0.69 keV, the total noise (FWHM) = 1.31 keV.

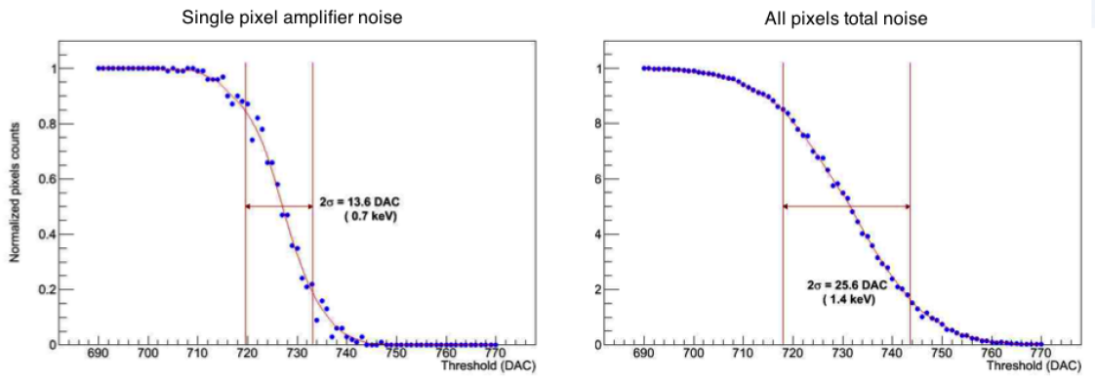

Figure 7.2: Noise measurements: single pixel (left) and all pixels (right).

7.4 X-ray energy resolution and spectral imaging

The total noise still has a not negligible contribution due to offset dispersion and gain variation as fig. 7.3 shows. Improvements in the energy resolution are foreseen in the second part of the first engineering run with the implementation of a minor modification to the pixel offset compensation algorithm. Nevertheless a good *energy resolution* of 6.6% (FWHM) at 60 keV has been measured (fig. 7.4) while keeping the high spatial resolving power provided by the 62 microns pixels. The energy distributions of fig. 7.4 refer to a region of 1000 pixels and two different acquisition modalities of PIXIE III: Pixel Mode (left panel) and Pixel Summing Mode (right panel). The two spectra have been obtained by differentiating the integral raw counts acquired through a fine threshold scan. The PIXIE III unit has a good *spectral capability* as it is demonstrated in fig. 7.4 where also the fluorescence and the escape peaks of the cadmium and tellurium components are shown together with the Am-241 main line at 59.6 keV.

The *imaging capability* of the Pixirad CdTe-PIXIE III assembly has been tested in the PSM configuration under high flux of X-ray radiation. As it can be seen in fig. 7.5, the detector can resolve up to 8 line pairs/mm with high modulation factor.

To demonstrate the *spectral imaging* power of the new detector a series of energy resolved X-ray diffraction experiments have been conducted. *Diffraction methods* are a powerful tool to investigate the crystal structure of compounds as for example the caffeine. By using a sharp selection of energy windows in a polychromatic X-ray

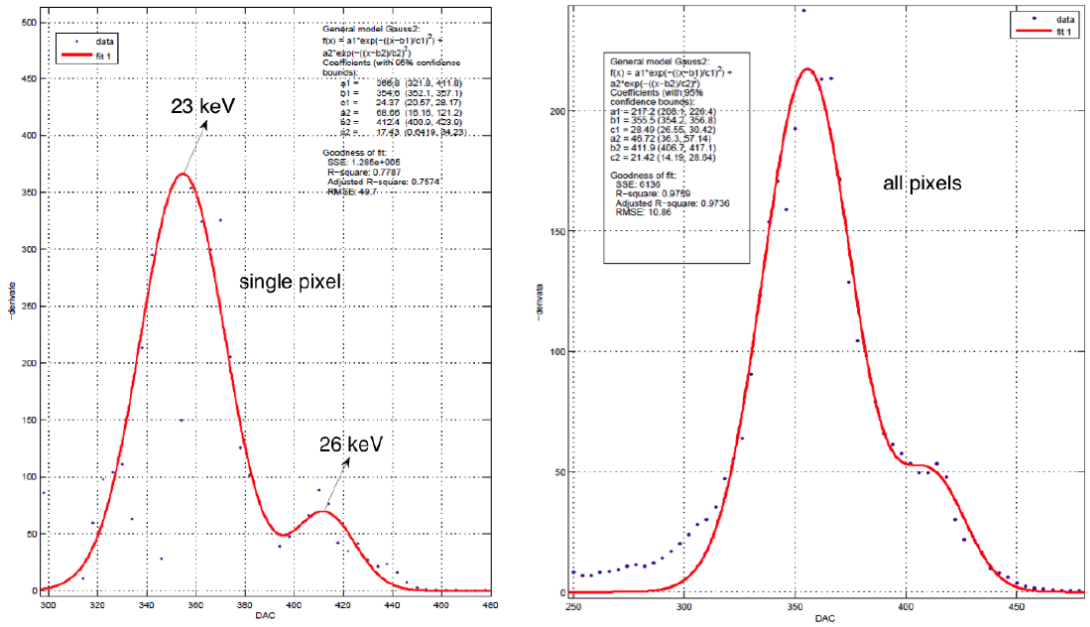

Figure 7.3: Experimental energy distribution for single pixel (left) and all pixels (right), obtained exploiting the cadmium fluorescent lines at 23 and 26 keV.

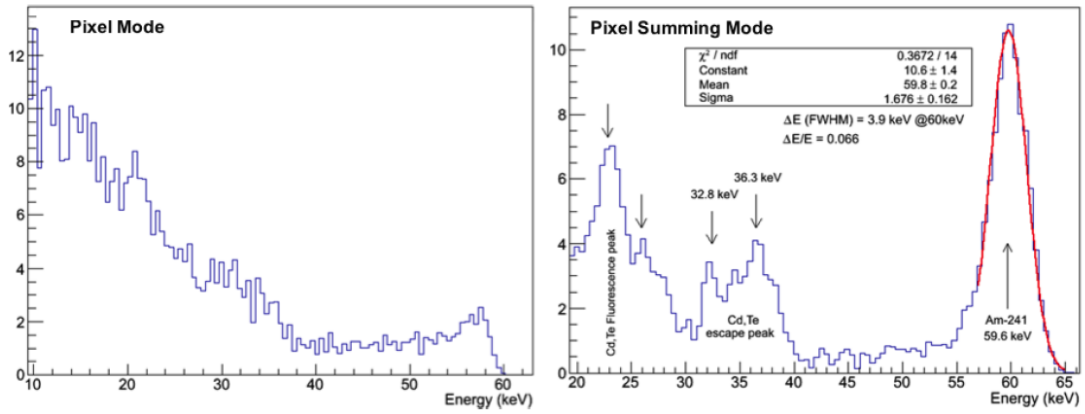

Figure 7.4: Energy distribution of 60 keV X-ray photons from Am-241. Data have been acquired in Pixel Mode (left) and Pixel Summing Mode (right). The distributions refer to a ROI of nearly 1000 pixels.

spectrum, possible with a PIXIE III-based Pixirad detector, the structure of an anhydrous caffeine powder has been detected. Fig. 7.6 (bottom panel) shows the unfiltered spectrum generated at 40 kVp by the X-ray tube with a tungsten anode (W) used in the experiment. Different energy windows have been selected in the spectrum by using

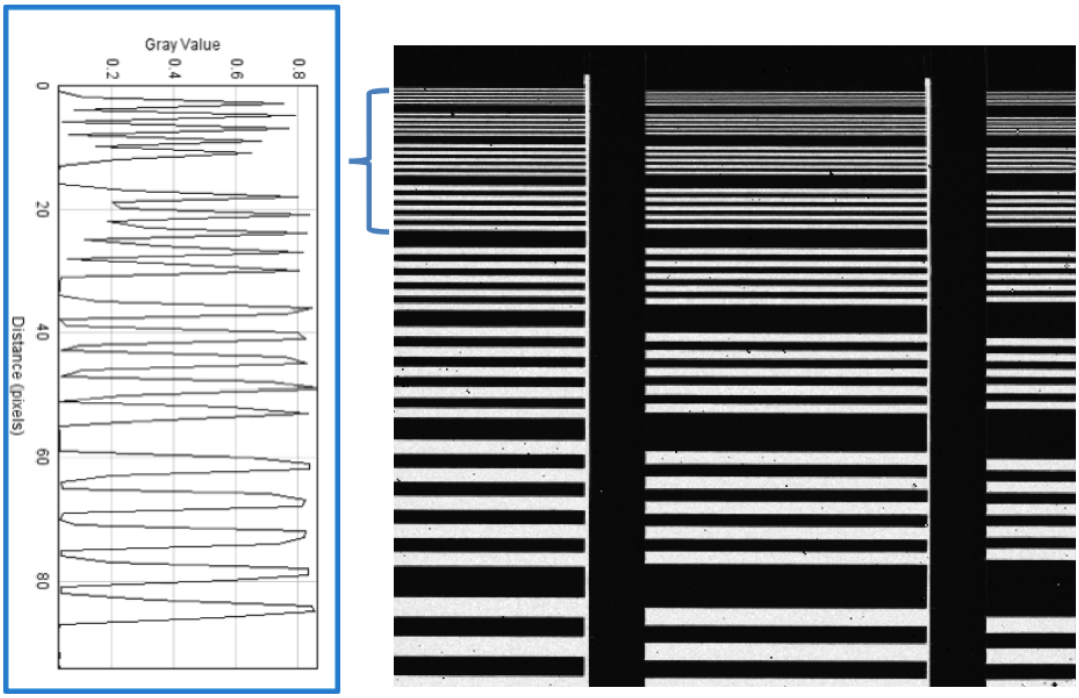

Figure 7.5: Imaging capability in Pixel Summing Mode. The highest density in the graph on the left, corresponds to the 8 lp/mm of the Huttner line-pairs test object.

PIXIE III as an electronic monochromator. In the top panel of fig. 7.6 the caffeine diffraction patterns (two rings with energy dependent radii) are shown. In the 8–12 keV energy range, data show the two rings, each one split in three sub-rings corresponding to the three W energy lines of around 8, 9 and 12 keV, while in the 9–10 keV energy window the two rings correspond to the main W line only. The two caffeine rings have been also visualized in a different setting, with photons taken from the continuum only, but using a sharp energy selection between 20 and 21 keV (fig. 7.6, top panel, rightmost image).

The sharp *color separation* achievable with PIXIE III is shown also in the two images reported in fig. 7.7. With the detector operating in Pixel Summing Mode there is no high energy photon leaking in the low energy window due to charge sharing. In the low energy photons image (left panel) bony structures are better visualized due to a higher bone-tissue contrast while at higher energies the contrast is highly reduced (right panel).

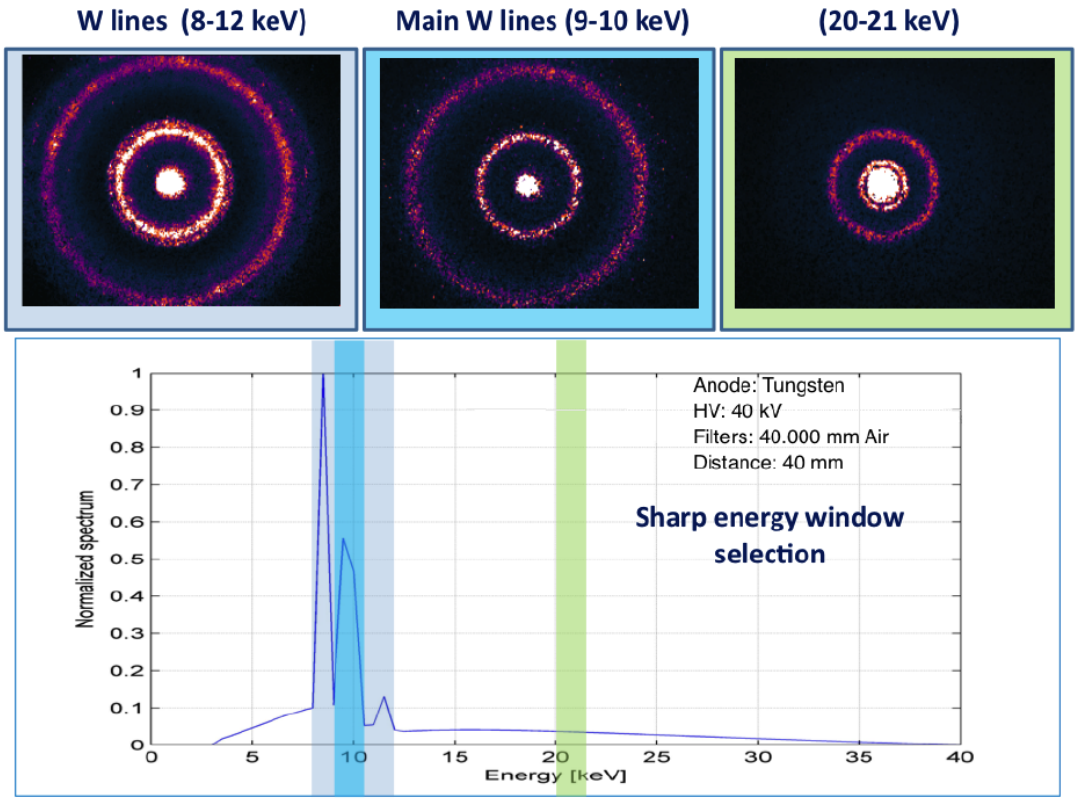

Figure 7.6: Caffeine diffraction patterns: two rings with energy dependent radii.

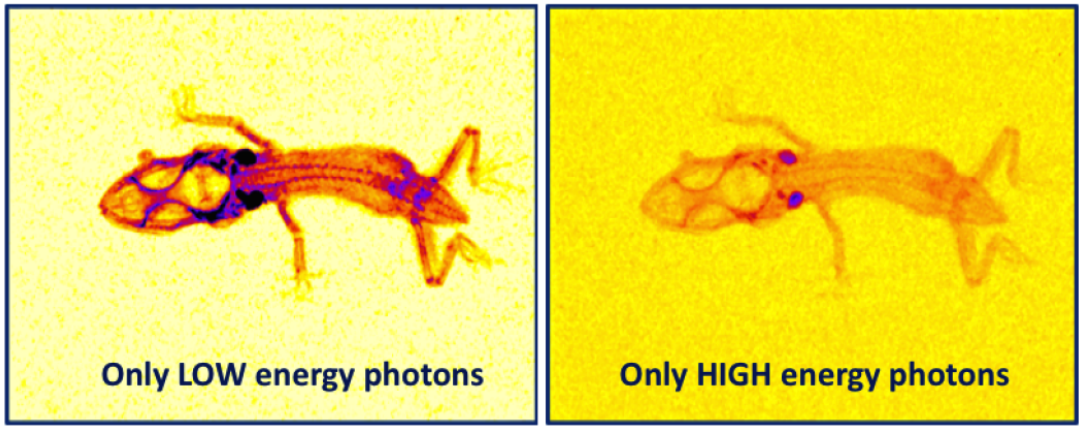

Figure 7.7: X-ray spectral imaging of a small animal obtained with the PIXIE III-Pixirad detector operating in Pixel Summing Mode.

Chapter 8

Conclusions and future developments

The purpose of this work is to characterize an innovative X-ray imaging sensor with intrinsic digital characteristics. It is based on Chromatic Photon Counting technology and developed by Pixirad Imaging Counters srl (INFN spin-off). The Pixirad-1 detector system counts individually the incident X-ray photons and selects them according to their energy to produce two color images per single exposure. The energy selection occurs in real time and at radiographic imaging speed (GHz global counting rate). Photon counting, color mode and a very fine spatial resolution ($8\ lp \cdot mm^{-1}$) allow to obtain a high ratio between image quality and absorbed dose. The individual building block of the imaging system is a two-side buttable semiconductor radiation detector made of a thin pixellated CdTe crystal coupled to a Very Large Scale Integration (VLSI) CMOS pixel ASIC (Application Specific Integrated Circuits).

A calibration curve with PIXIE II (the second generation of Pixirad ASIC) has been obtained in a wide energy range (from 3 to 60 keV). The detector has shown good energy resolution (from 25,8% to 2,9% in the same energy range). The statistical fluctuations affect the energy resolution according to the theoretical estimation. The agreement is better in case of single pixel than in case of cluster of pixels. The source of the FWHM broadening effect for cluster of pixels is related to slightly differences in pixel amplifier gain and the residual DC offsets after compensation. As expected the sharpness of color separation is limited by charge sharing effects, when working with polychromatic beams, and using the simple method described this contribution proves to be non-negligible.

Finally, the new generation of large area ASICs PIXIE III is presented and characterized. This innovative architecture is very flexible and various operation modalities can be selected to better suit the specific application needs (lowest energy threshold, highest rate capability, highest frame rate). Its main goal is to provide a sharp X-ray color imaging while working with very small pixels (62 microns). The energy resolution of 1.72 keV (FWHM) at 23 keV is demonstrated, with no charge sharing tails. When working in *sum mode* it allows to fully recover the charge sharing ef-

fect, providing two *color* images in a single exposure characterized by high chromatic purity (spectroscopic imaging). The residual spread of the pixel DC offsets after auto-calibration needs to be further optimized. We will try to achieve this with the second wafer batch of our first pilot engineering run.

A future very interesting application field of this technology is the *neutron imaging*, a promising new non-destructive imaging method in areas such as scientific research,industrial and medical applications, and security systems. As demonstrated in this work, CdTe sensors have high spatial and energy resolutions and they can be operated at room temperature, making them suitable for neutron imaging. Moreover, CdTe contains Cd-113, which has large thermal neutron capture cross-section and acts as a neutron converter, emitting gamma rays and conversion electrons on neutron capture [23]. The future challange for Pixirad system detector is to investigate its spatial resolutions as neutron imager and neutron/gamma ray discrimination capability.

Appendix A

Image gallery

(a)

(b)

Figure A.1: Images of an object with a very low absorption power (a tiny flower), (a) 1 keV threshold, (b) 6 keV threshold. These two images were taken in a single shot of radiation.

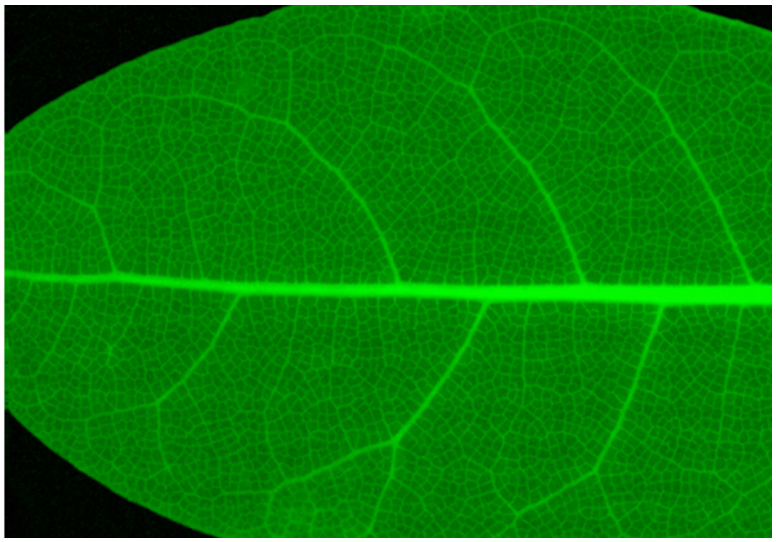

(a)

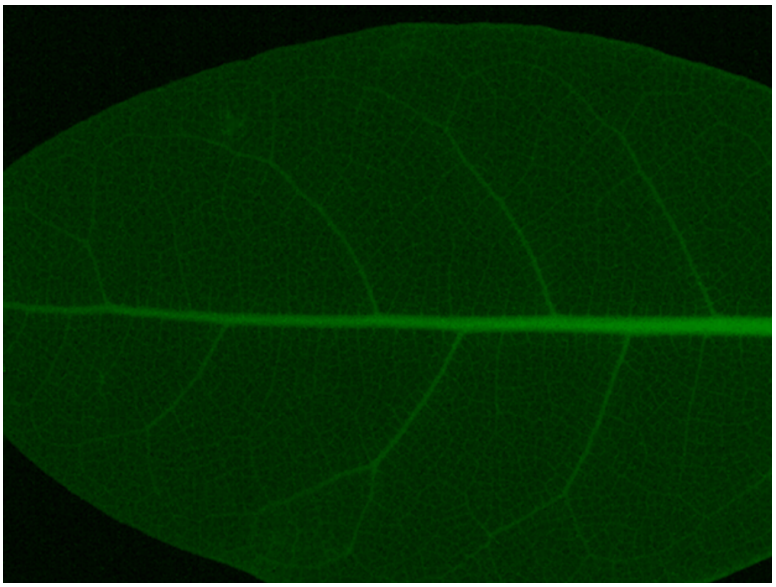

(b)

Figure A.2: Images of an object with a very low absorption power (a leaf), (a) 1 keV threshold, (b) 6 keV threshold. These two images were taken in a single shot of radiation.

Figure A.3: Detail of human hand bones.

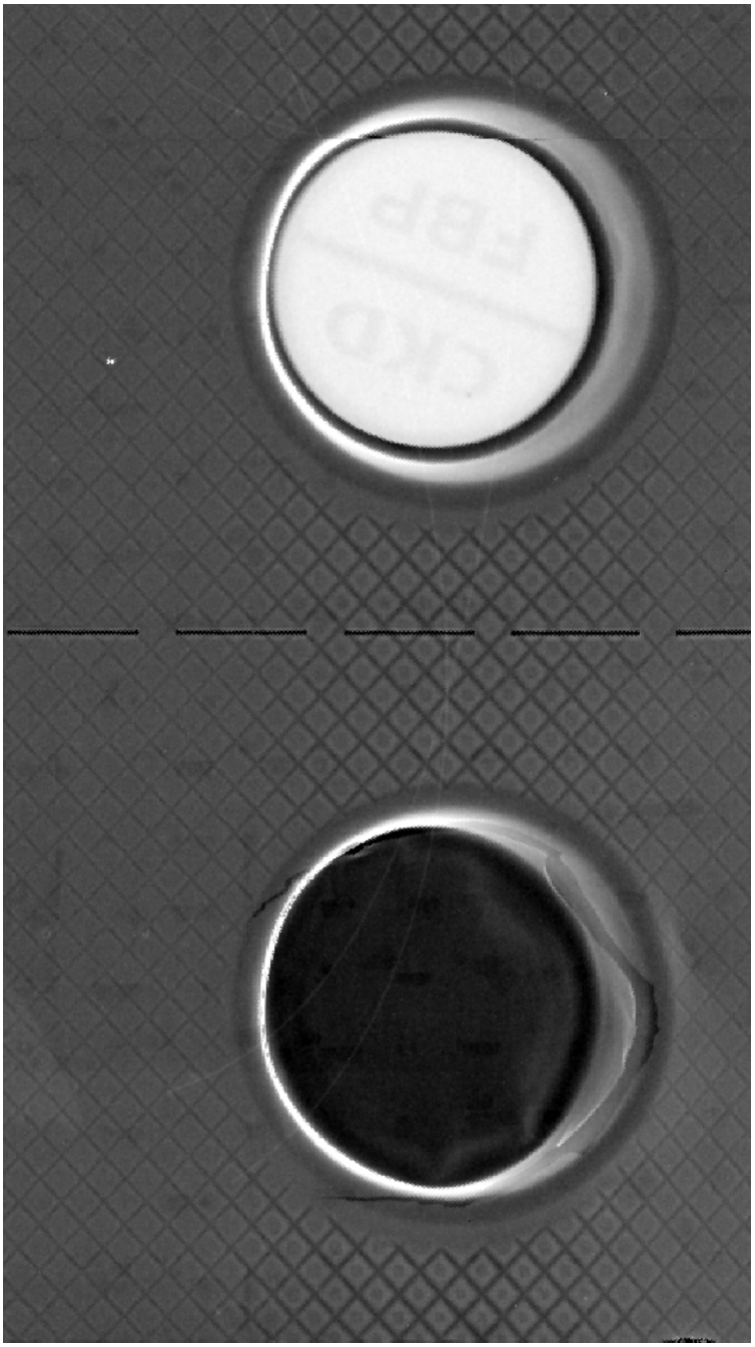

Figure A.4: Detection of foreign objects (human hair) inside a pill alluminum package.

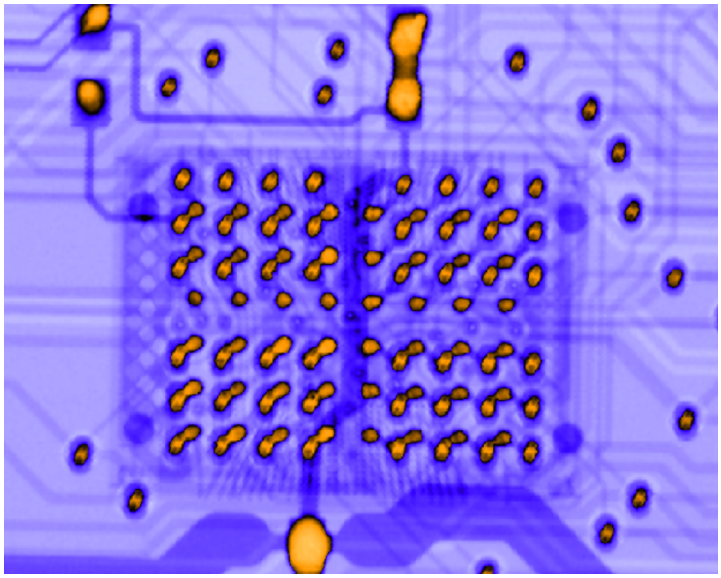

(a)

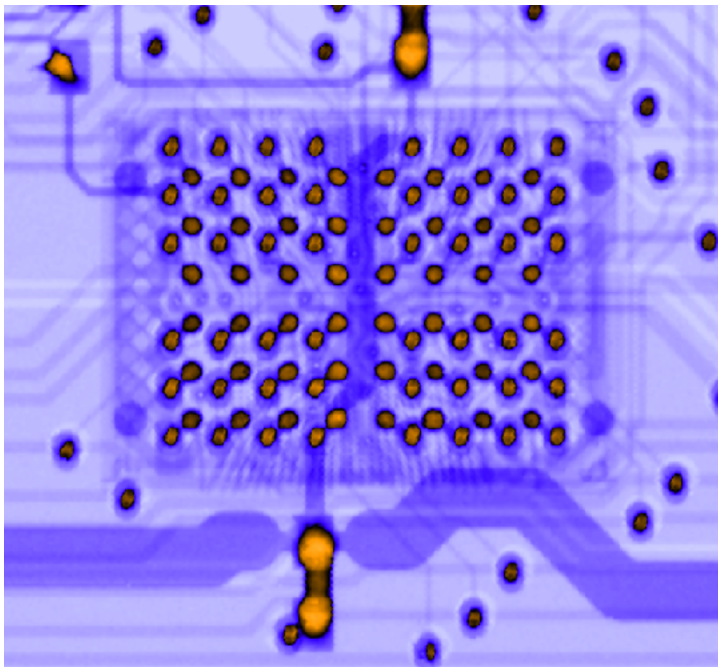

(b)

Figure A.5: Radiograph of a high density memory connected with a BGA technology: solder bumps of bad (a) and good (b) quality are visible.

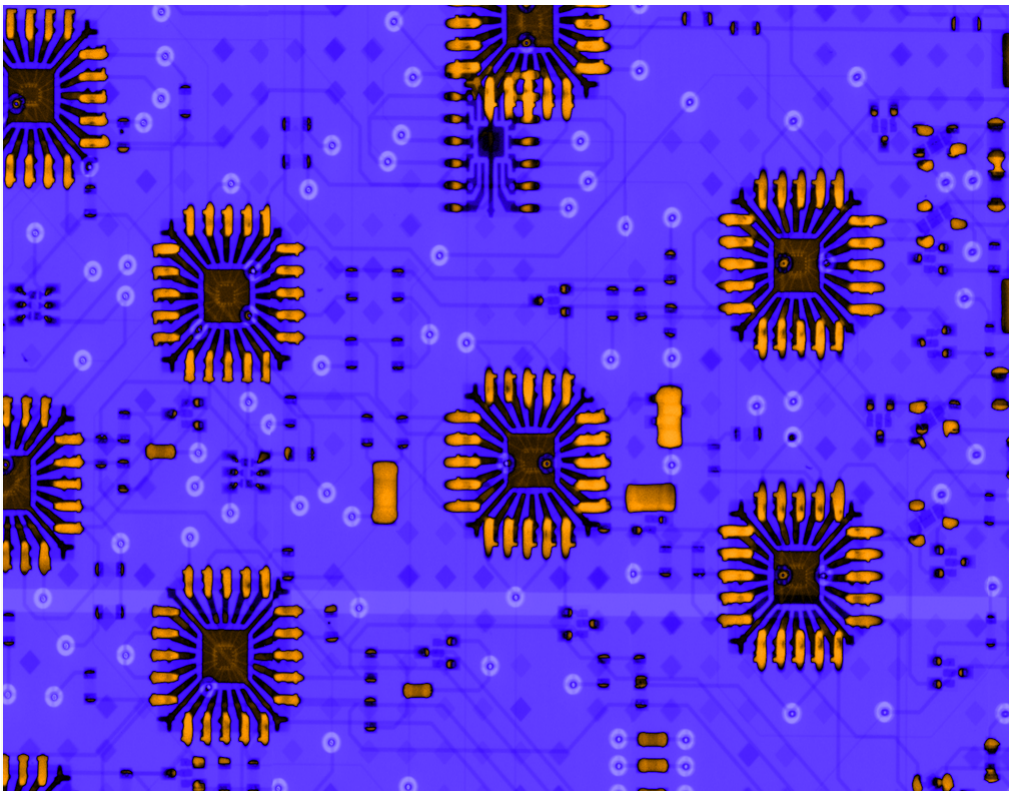

Figure A.6: A detail of the image of a large PCB taken in slot-scanning mode. Wire bondings inside an electronic package are neatly visible.

Bibliography

[1] Smith F. A. *A primer in applied radiation physics*. World Scientific Publishing Co. Re. Ltd, 2000.

[2] Knoll G. F. *Radiation Detection and Measurements*. John Wiley & Sons, 2000.

[3] Leidholdt E. Boone J. Bushberg J. Seibert J. *The essential physics of medical imaging*. Ed. by Lippincott Williams & Wilkins. 2002.

[4] Itoh T. Doi K. Morishita J. Ueda K. Ohtsuka A. Fujita H. Tsai D.Y. "A simple method for determining the modulation transfer function in digital radiography". In: *Medical Imaging, IEEE Transactions* 11.1 (1992), pp. 34–39.

[5] Wirth S. Pfeifer K. Reiser M. F. Treitl M. Korner M. Weber C. H. *Advances in Digital Radiography: Physical Principles and System Overview*. 2005 RSNA Annual Meeting.

[6] Pacella D. "Energy-resolved X-ray detectors: the future of diagnostic imaging". In: *Reports in Medical Imaging* (2015).

[7] Rohe Wermes Rossi Fischer. *Pixel detectors: from fundamentals to applications*. Springer, 2005.

[8] Spieler H. *Semiconductor Detector Systems*. Oxford University Press, 2005.

[9] Caroli E. Mancini A. M. Zappettini A. Ubertini P Del Sordo S. Abbene L. "Progress in the Development of CdTe and CdZnTe Semiconductor Radiation Detectors for Astrophysical and Medical Applications". In: *Sensors Molecular Diversity Preservation International (MDPI)* 9 (2009), pp. 3491–3526.

[10] Ryuji Jinnai Akira Tachibana Minoru Funaki Yukio Ando and Ryoichi Ohno. *Development of CdTe detectors in Acrorad*. Tech. rep. Monograph of Acrorad.

[11] Aokia T. Tomitab Y. Hatanaka Y. M. Niraulaa M. Nakamuraa A. "Stability issues of high-energy resolution diode type CdTe nuclear radiation detectors in a long-term operation". In: *Nuclear Instruments and Methods in Physics Research A* 491 (2002), p. 168.175.

[12] Schulman T. “Si, CdTe and CdZnTe radiation detectors for imaging applications”. PhD thesis. Faculty of Science of the University of Helsinki, Finland, 2006.

[13] Mikkelsen S. Maehlum G.E. Wagenaar D.J. Tsui B.M. Patt B.E. Frey E.C. Wang X. Meier D. “MicroCT with energy-resolved photon-counting detectors”. In: *Physics in Medicine and Biology* 56.9 (2011).

[14] Krummenacher F. “Pixel detectors with local intelligence: an IC designer point of view”. In: *Nuclear Instruments and Methods in Physics Research Section A* 305 (1991), 527–532.

[15] Brez A. Minuti M. Pinchera M. Mozzo P. Bellazzini R. Spandre G. “Chromatic X-Ray imaging with a fine pitch CdTe sensor coupled to a large area photon counting pixel ASIC”. In: *Journal of Instrumentation* 8 (2013).

[16] Spandre G. Bellazzini R. “Gas Pixel Detectors”. In: *ICFA Instrumentation Bulletin* Vol. 27 (2005).

[17] PIXIRAD Imaging Counters s.r.l. URL: http://pixirad.pi.infn.it/.

[18] *Specifica tecnica generale IMAGER - PIXIRAD*. Rev. 2. STM Products S.r.l. 2012.

[19] Delogu P. Bellazzini R. Brez A. Minuti M. Pinchera M. Spandre G. Vincenzi A. de Ruvo P. L. “Energy characterization of Pixirad-1 photon counting detector system”. In: *Journal of Instrumentation* 10, C04010 (Apr. 2015), p. C04010. DOI: 10.1088/1748-0221/10/04/C04010.

[20] Bellazzini R. Brez A. de Ruvo P.L. Minuti M. Pinchera M. Spandre G. Vincenzi A. Delogu P. Oliva P. “Characterization of Pixirad-1 photon counting detector for X-ray imaging”. In: *Journal of Instrumentation* 11.01 (2016), P01015. URL: http://stacks.iop.org/1748-0221/11/i=01/a=P01015.

[21] Spandre G. Minuti M. Pinchera M. Delogu P. de Ruvo P.L. Vincenzi A. Bellazzini R. Brez A. “PIXIE III: a very large area photon-counting CMOS pixel ASIC for sharp X-ray spectral imaging”. In: *Journal of Instrumentation* 10 (2015).

[22] Campbell M. Horswell I. Llopart X. Marchal J. Sawhney K.J.S. Tartoni N. Turecek D. Gimenez E.N. Ballabriga R. “Study of charge-sharing in MEDIPIX3 using a micro-focused synchrotron beam”. In: *Journal of Instrumentation* 6.01 (2011), p. C01031. URL: http://stacks.iop.org/1748-0221/6/i=01/a=C01031.

[23] Singh Morii Mimura Aoki Miyake Nishioka. “Development of a CdTe thermal neutron detector for neutron imaging”. In: *Nuclear Instruments and Methods in Physics Research A* 677 (2012).